Multifunctional Three-Dimensional Nanoelectronic Networks for Smart Materials and Cyborg Tissues

Citation

Dai, Xiaochuan. 2015. Multifunctional Three-Dimensional Nanoelectronic Networks for Smart Materials and Cyborg Tissues. Doctoral dissertation, Harvard University, Graduate School of Arts & Sciences.

Multifunctional Three-Dimensional Nanoelectronic Networks for Smart Materials and Cyborg Tissues

A DISSERTATION PRESENTED
BY
XIAOCHUAN DAI
TO
THE DEPARTMENT OF CHEMISTRY AND CHEMICAL BIOLOGY

IN PARTIAL FULFILLMENT OF THE REQUIREMENTS
FOR THE DEGREE OF
DOCTOR OF PHILOSOPHY
IN THE SUBJECT OF
CHEMISTRY

HARVARD UNIVERSITY
CAMBRIDGE, MASSACHUSETTS
MAY 2015

Dissertation advisor: Professor Charles M. Lieber Xiaochuan Dai

Multifunctional Three-Dimensional Nanoelectronic Networks for Smart Materials and Cyborg Tissues

ABSTRACT

Nanomaterials provide unique opportunities at the interface between nanoelectronics and biology. "Bottom-up" synthesized nanowire(NW) with defined functionality can be assembled and enabled into three-dimensional(3D) flexible nanoelectronic networks. The micro- to nanoscale electronic units blur the distinction between electronics and cells/tissue in terms of length scale and mechanical stiffness. These unconventional 3D nanoelectronic networks can thus provide a path towards truly seamless integration of non-living electronics and living systems. In this thesis, I will introduce a general method for fabricating 3D macroporous NW nanoelectronic networks and their integration with hydrogel, elastomer and living tissues, with an emphasis on the realization of two-way communication between active nanoelectronics and the passive or living systems in which they are embedded.

First, fabrication of 3D macroporous NW nanoelectronic networks will be described. Examples showing hundreds of individually addressable, multifunctional nanodevices fully distributed and interconnected throughout 3D networks will be illustrated. Proof-of-concept studies of macroporous nanoelectronic networks embedded through hydrogels and polymers demonstrate the ability for dynamically mapping pH gradients and strain fields.

Second, a universal method to improve the long-term stability of semiconductor NWs in physiological environments using atomic layer deposition(ALD) of dielectric metal oxides

shells on NW cores will be introduced. Long-term stability improvement by ALD of Al_2O_3 shells with different shell thickness and annealing conditions will be described and discussed. In addition, studies of semiconductor NW nanodevices with multilayer Al_2O_3/HfO_2 shells indicates stability for up to two years in physiological solutions at 37°C.

Third, 3D macroporous nanoelectronic networks were integrated with synthetic cardiac tissues to build "cyborg" cardiac tissues. Spatiotemporal mapping of action potential(AP) propagating throughout 3D cardiac tissue was carried out with sub-millisecond time resolution, allowing investigation of cardiac tissue development and responses to pharmacological agents. These results have promised the applications of cyborg tissues in the fields ranging from fundamental electrophysiology and regenerative medicine to pharmacological studies.

Finally, multifunctionallities of nanoelectronic devices for applications at the bio/nano interface will be discussed. Incorporation of NW field-effect-transistor(FET) and electrical stimulators in macroporous nanoelectronic networks demonstrates simultaneous recording and regulation of AP propagation in cyborg cardiac tissues. In addition, a convexed-NW FET bioprobe has been developed for simultaneous detection of AP and contraction force from individual cardiomyocyte. These explorations on the nanoelectronics functionalities highlight the capability to enable new communication modes between electronics and living tissues.

Contents

Listing of figures

DEDICATED TO MY PARENTS AND NIANQIAO PHYLLIS JU.

Acknowledgments

Five years of PhD is a long journey that consists of moments of hard work, satisfaction, disappointment and surprise. Those people who accompanied me, advised me, assisted me and encouraged me along the journey become the most valueable presents in my life. I cannot be more grateful to them who made everything in these years possible.

My advisor, Dr. Charles M. Lieber, brought me to the field of nanoscience and nanotechnology and lightened my research career. Charlie is an incrediably smart scientist, responsible advisor, constructive mentor and supportive friend. His tremendous erudition, constant enthusiasm on research, supreme pursuit of perfection deeply inspired me as a young scientist and as a young man. I want to thank him, for being my beacon, for tailoring my shortcomings and immaturation, for training me to think from subtlety to magnificence, for encouraging me to survive in difficuities, and for supporting me to strive for my career. Graduation can be granted at many places but only having him as my advisor can I gain the confidence in becoming an outstanding scholar.

My sincere gratitude also goes to the members of my Graduate Advising Committee, Dr. X. Sunney Xie, Dr. Daniel G. Nocera and Dr. Xiaowei Zhuang. Through the research discussion with them for a few times, I received substantial advices and suggestions that helped pave the path for my research projects and inspire now thoughts. I also want to thank them for their continuous and extensive support for my academic career.

None of the research projects accomplished during my PhD studies can be done without teamwork. I cannot help acknowledging those great researchers who worked together with me to achieve all of these beautiful works. Dr. Jia Liu and Dr. Chong Xie worked with me to develop the macroporous nanoelectronic networks and enable all the following works based on this platform. Fruitful teamwork with Dr. Wei Zhou earns us the powerful method for enhancing the stability of nanoelectronics in plysiological environment. We also worked together and demonstrated "cyborg" cardiac tissue investigation for electrophysiology, tissue development, pharmacological studies, arrhythmia modeling and cardiac activity regulation. Dr. Jun Yao collaborated with me to build the novel convexed-NW dual-functional bioprobes for simultaneous electrical and mechanical studies of cardiomyocyte. Dr. Teng Gao joined our team in my graduating year. His efforts and contributions boost the last project towards completion much more efficiently.

I also want thank many labmates for their help in experiments and discussion. Dr. Robort Day and Max Mankin are experts in CVD synthesis of NWs and they helped me a lot in the trouble shooting of CVD experiments. I thank Dr. Xiaojie Duan, Dr. Hao Yan, Dr. Xiaocheng Jiang and Dr. Ping Xie for sharing their extensive experience on nanoelectronics fabrication and electrical property chracterization. Dr. Bozhi Tian, Dr. Quan Qing and Dr. Tzahi Cohen-Karni taught me cell culture and electrophysiology measurement and should earn my great gratitude. My sincere thanks are also due to Dr. James Cahoon, Dr. Yongjie Hu, Dr. SungWoo Nam, Dr. Hwan Sung Choe, Dr. Lin Xu, Dr. Ruixuan Gao, Dr. Zengguang Cheng, Dr. Ning Gao, Dr. Peter Kruskal, Dr. Jae-Hyun Lee, Dr. Guosong Hong, Zhe Jiang, Tian-Ming Fu, Tao Zhou and Sean You for their helpful advices, insightful discussing, and making our lab such a pleasant place to work.

I also want to express my great gratitude to many collaborators from other prestigious research groups and bring their specialties to me. Jia Liu from Bertoldi group at *School of Engineering and Applied Sciences, Harvard University* strongly supported our research via his impressive expertise on mechanics simulation. Yang He from Hoffman group at *Department of Physics, Harvard University* translated his data analysis skills to help with motion tracking of cardiomyocyte contraction. I would like to thank Dr. Donghui Zhang and Dr. Zhiqiang Lin from Pu group at *Boston Children's Hospital, Harvard Medical School*, Dr. Yi-Dong Lin and Dr. Yanfei Yang from Liao group at *Brigham and Women's Hospital, Harvard Medical School* for inspiring discussion on heart regeneration and electrophysiology.

Smooth and efficient research cannot run without all the supporting people. I want to pass on my sincere thank to the staffs at *Center for Nanoscale Systems(CNS), Harvard University*, Jiangdong Deng, Adam Graham, Hao-Yu Lin, Yuan Lu, Dr. Andrew Magyar and Jason Tresback, for their patient guidance on instruments and great maintainance to keep *CNS* such a wonderful research platform. I also want to thank the technical staff in our lab, Dr. Jinlin Huang, for his ubiquitous help and support throughout these years. It is my great pleasure to work with Jinlin and learn from him. I appreciate our administrative staff, Purvant Patel, Dr. Kathleen Ledyard and Renée Donlon for their efforts, help and kindness beyond their job.

My last and deepest thank should go to my families. Their endless love, support and understanding along all these years is my strongest force. It helps me go through the most difficult times and keep pursuing the unknowns. It is my greatest fortune to have them with me. Graduating is never the end of my journey but a celebration on the way, allowing me to share my happiness with all the accompanying people.

1

Introduction

The unprecedented advances in nanoscience and nanotechnology provide us with opportunities to gain new insight into new scientific fields in the last half-century. The silicon (Si) industry keeps its pace in the miniaturization of electronic components, which leads to the realization of increasingly fast computing processors, highly integrated circuitry chips, exponentially expanding memory media. In parallel, rapid development of mechanically flexible electronics provide new capabilities that cannot be accessed by conventional technologies. This new type of electronics, such as flexible display screen[1], elastic battery[2, 3], paper-like computer[4, 5] make people believe the possibility of seamless integration of flexible electronics with our clothes, skins[6, 7], contact lens and other wearable objects.

Especially for the applications of bioelectronics, such as brain stimulators[8], implantable biosensors[9], etc.[10, 11], the flexibility of electronics is critically required for them to mechanically match the cells or tissues and further guarantee the good electronics-biology interface.

Nanomaterials and nanoelectronics play an important role in building flexible bioelectronics because (1) nanoscale electronics geometrically match the dimension of common biological targets, which makes it possible to build integrated nanoelectronics with active subcellular size components; (2) bending stiffness of nanoelectronic structures is proportional to one over the fourth order of the their dimension, which can make the nano-scale electronics as soft as cell or tissues. Traditional nanoelectronics fabrication mainly relies on the "top-down" paradigm[12], in which nanostructures of electronic units are defined using lithography techniques and subsequently tailored from large-scale single-crystalline bulk materials (i.e., Si wafers). This fabrication paradigm intrinsically precludes the fabrication of nanoelectronics on flexible substrates. Although several transfer techniques have been developed[13] to address this problem, they are still at an early stage, which can only reach operational resolution at the micrometer to millimeter scale, and also is not compatible with the scale-up productions. Organic and polymeric electronics demonstrate another solution for fabricating flexible electronics. However, poor electrical performance remains an obstacle for extensively adopting these materials[2, 3, 14–18].

The "bottom-up" paradigm, on the other hand, is a more promising alternative[19–23]. In the "bottom-up" paradigm, nanomaterials are synthesized from the most primitive units, atoms, molecules and nanoclusters, and assembled into complex structures[24, 25]. The synthesized nanomaterials can be manipulated and patterned on virtually various substrates and target for fabricating high-performance nanoelectronics. The dimension of these "bottom-up" synthesized nanomaterials is comparable with, or even smaller than, that of the state-of-the-art nanoelectronic units[26]. In addition, nanomaterials synthesized by "bottom-up" methods, analogous to the way that biology so successfully works, have unique advantage in achieving sophisticated geometry and controllable doping modulation, which makes them more promising to fulfill the increasing requirements for integration and multifunctionalities.

1.1 Synthesis of Nanowires

The semiconductor NWs with great flexibility have become promising building blocks of "bottom-up" nanomaterials for fabricating nanoelectronics, as they have been extensively investigated during past decades. Nearly all the conventional industrial electronics systems have been demonstrated by using well-designed NWs, including memory, computing circuit, etc., proving their potential applications in multifunctional flexible nanoelectronics.

A general process for synthesizing NWs is nanocluster catalyzed vapor-liquid-solid (VLS) growth (Figure 1.1)[27]. In this process, the metal nanoclusters are heated above the eutectic temperature of metal-semiconductor alloy. The melted metal-semiconductor nanoclusters were subsequently feed with a vapor-phase precursor, which serves as the semiconductor source. The oversaturated semiconductor atoms gradually precipitate at the solid-liquid interface; preferentially incorporates into the solid semiconductor lattice; and result in directional one-dimensional single crystal growth. Different methods have been explored to grow semiconductor NWs. The chemical vapor deposition (CVD) process is the most popular technique for VLS growth. In the case of Si NW growth, Au nanopar-

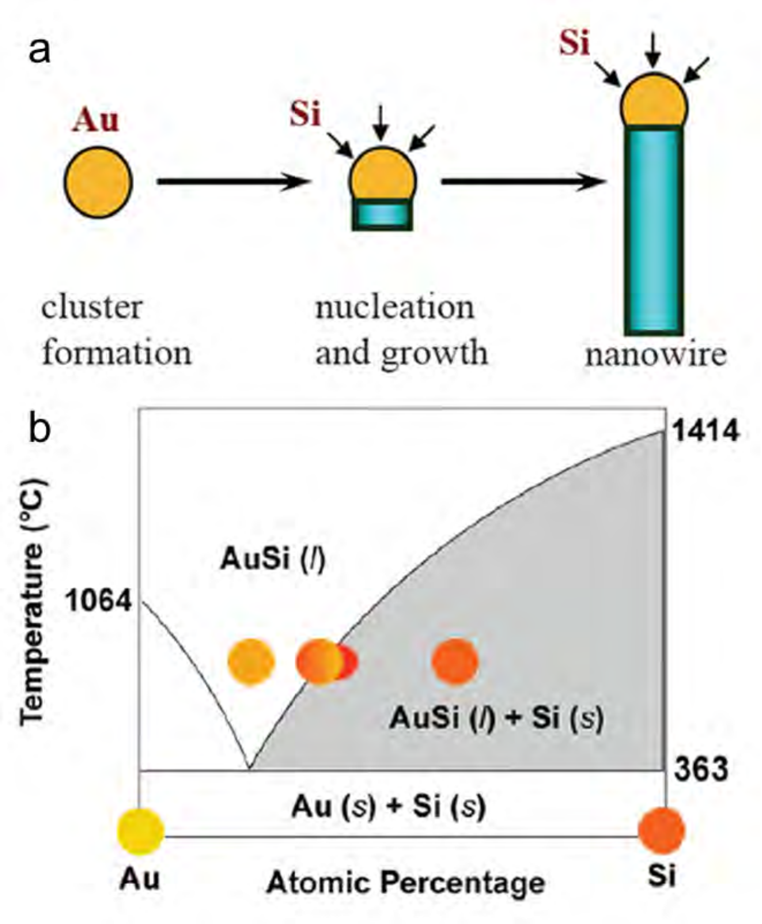

Figure 1.1: Schematic of VLS growth of Si NWs. (a) A liquid alloy droplet of Au-Si is first formed above the eutectic temperature (363 °C) of Au and Si. The continued feeding of Si in the vapor phase into the liquid alloy causes oversaturation, resulting in nucleation and directional NW growth. (b) Binary phase diagram for Au and Si illustrating the thermodynamics of VLS growth. (Courtesy of ref. [27])

ticles could serve as catalytic sites where the gaseous precursor silane decomposes to provide Si reactant. Similar processes can be extended to synthesize different single crystal NWs, including semiconductor groups IV, III-V and II-VI, by selecting desirable nanocluster and precursors. One major advantage of CVD method is that with precise design growth parameters and procedures, sophisticated geometries such as axial heterojunctions, radial heterojunctions, branched NWs, kinked NWs as well as corresponding composition/doping modulation can be achieved[27–30]. These "bottom-up" synthesized NWs have been utilized to build different types of nanoelectronic devices including FETs[31], light-emitting-diodes[32], biochemical sensors[33, 34], etc.

1.2 Assembly of Nanowires

The superior device performance of NW building blocks has been well-studies and discussed, however, developing efficient and scalable strategies to assemble large amount of NWs into increasingly complex architectures is critical to build NW based integrated devices and circuits. Up to date, fluidic flow-directed alignment[35, 36], Langmuir-Blodgett approaches[37, 38], shear force alignment[39, 40] and lubricant-assisted contact printing[41] methods have been reported to assemble large-scale oriented NW arrays at room temperature on different kinds of substrates, including Si wafer, glass, plastics, paper, etc. After assembly of NW on the target substrates, conventional lithography can be carried out on those well-aligned NWs to build nanoelectronic circuits.

Among all the above assembly methods, lubricant-assisted contact printing method shows great potentials in wafer-scale assembly of highly ordered, dense, and regular arrays of NWs with high uniformity and reproducibility. A high density NW arrays with a

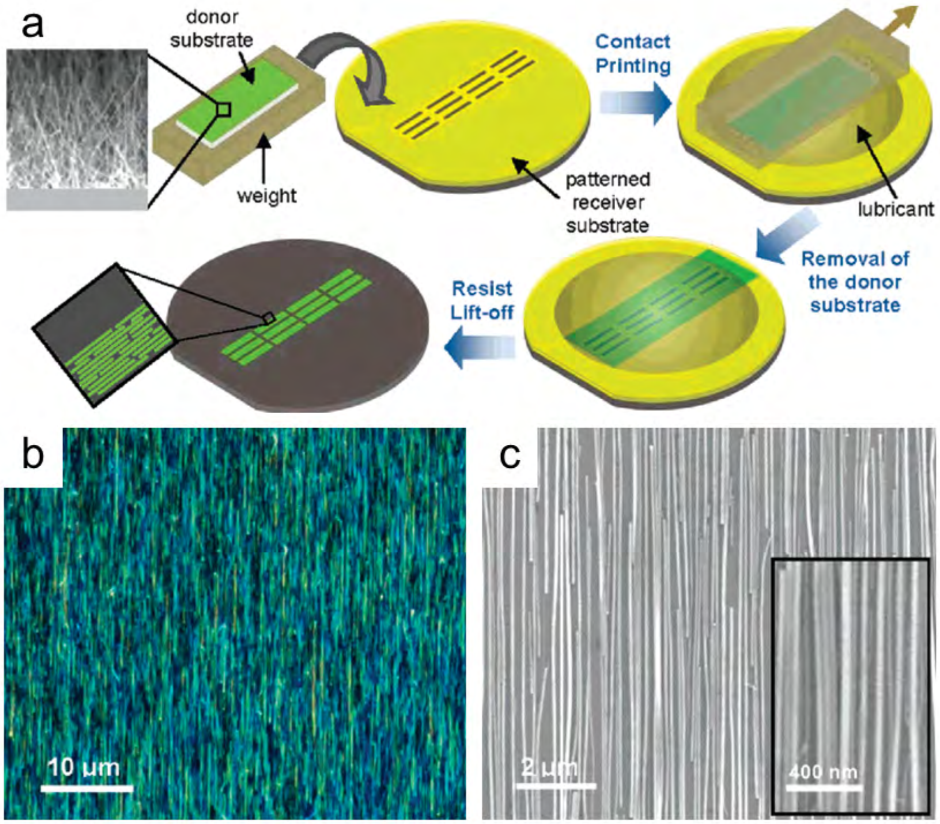

Figure 1.2: Contact printing of NWs. (a) Schematics of the process flow for contact printing of NW arrays. (b) Dark-field optical image of Ge NWs (Diameter: 30 nm) printed on a SiO_2/Si substrate showing highly dense and aligned monolayer of NWs. (c) SEM image of aligned NWs. (Courtesy of ref. [40])

high alignment ratio (ca. 90–95% with a misalignment angle of ±5°) has been demonstrated (Figure 1.2)[40]. This process uses the NW growth substrate as a donor substrate to directionally slide over a receiver substrate, which can be different materials with surface pre-treatment to affiliate with the NW surface. Lubricants such as octane and mineral oils are used between the two substrates for the purpose of minimizing the NW-NW friction. During the contact printing process, NWs are detached from the donor substrate as they are anchored by the van der Waals interactions with the surface of the receiver substrate, resulting in the direct transfer of aligned NWs to the receiver chip. Through the contact printing technique and following conventional lithography processes, flexible nanoelectronic devices based on well aligned NWs can be fabricated for different purposes. McAlpine *et al.*[42] demonstrated the fabrication of chemical sensors on a flexible substrate. Timko *et al.*[43] reported the fabrication of Si NW FET arrays for electrical potential detection and recorded extracellular APs from chicken cardiomyocytes. Takei *et al.*[44] utilized contact printing technique to assembly Ge/Si core-shell NW on a polyimide substrate to build NW active matrix circuitry and demonstrated this circuitry as electronic "skin" for pressure sensing.

However, contact printing method still has its own limitations with respect to avoiding crossing defects while aiming for large-scale and dense assembly of NWs. To further improve the contact printing technique, Yao *et al.*[45] have recently reported a nanocombing assembly technique (Figure 1.3). The main innovation of new transfer technique is the separation of the anchoring region of NWs from the aligning region. Regarding to the anchoring regions, surface of receiver substrate has been treated physically or chemically affiliative to NWs. In the aligning regions, substrate has weaker Van der Waals interac-

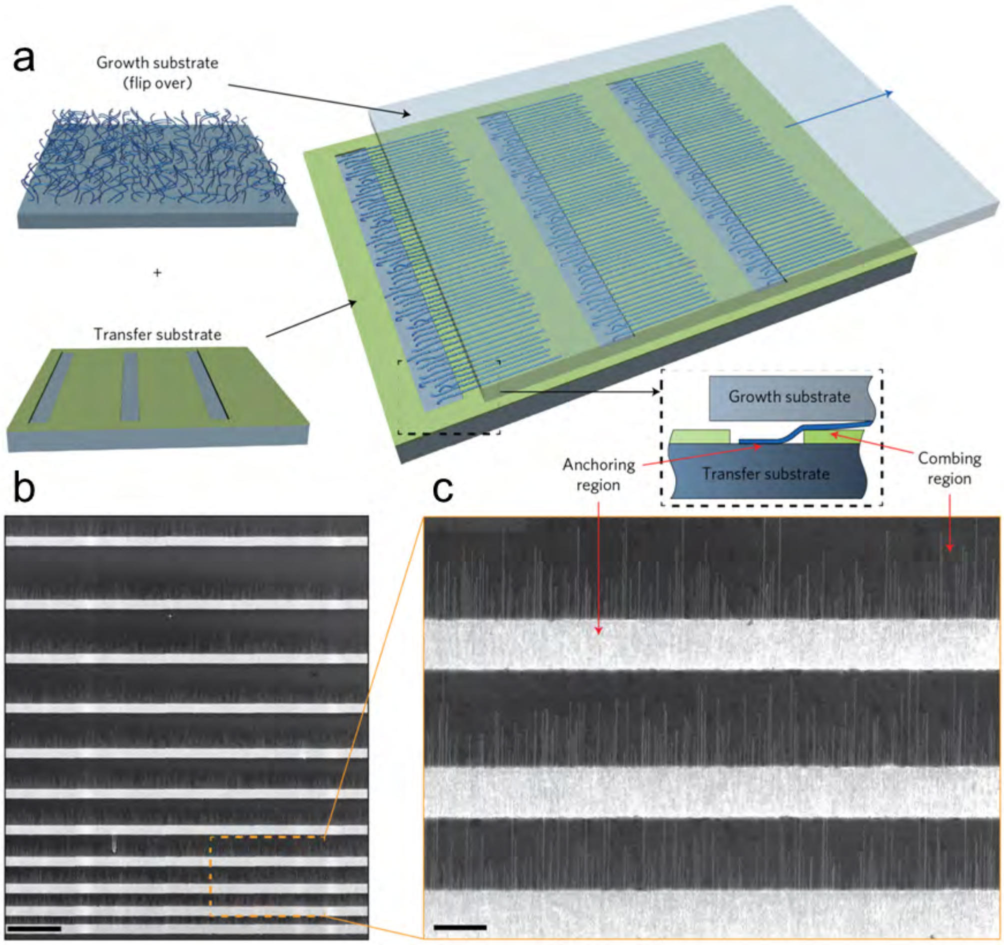

Figure 1.3: Nanocombing of NWs. (a) Schematics of the nanocombing process. The blue arrow indicates the travelling direction of the growth substrate with respect to the target substrate, which yields a combing/aligning force that is parallel and opposite to the anchoring force. The dashed window at the right bottom shows a side view of the nanocombing process. (b–c) SEM images of Si NWs on the combing (resist) surface at different magnifications. The thickness of the resist (S1805) layer was 70 nm. Scale bars: 50 μm (b), 10 μm (c). (Courtesy of ref. [45])

tions to ease NW stretching and straightening by shear force. This method yields NW arrays with >98.5% of NW aligned within ±1° of the combing direction. Besides, by lithographic patterning of anchoring regions and aligning regions, a deterministic assembly has been demonstrated to produce high yield of NW arrays with each NW located at desirable sites.

1.3 Flexible Nanoelectronics and Applications in Biological Systems

Nanoelectronic detection of biomolecules and recording of cellular electrical activity have been highly successful. The capacity of nanoelectronics for high throughput, scalability and low cost has led to novel analytical devices for disease-marker detection, DNA sequencing and other applications. Electrical recording of electroactive cells (i.e., neurons, cardiomyocytes, etc.) are important on research areas ranging from fundamental biophysical studies to biomedical applications[46–48]. In past decades, glass patch pipette[49], sharp electrode probes, multi-electrode arrays[50] and planar FETs[51] have been demonstrated to interface electrogenic cells. These reported approaches are limited by the size and the flexibility due to either fabrication strategies or intrinsic recording mechanism. Reducing their invasiveness and detection size remains critical for cellular or even subcellular measurement. Having intrinsic good flexibility and small dimension features, NW based nanoelectronics provide a promising solution to achieve bio-sensing or bio-recoding in high spatial resolution.

Recently, there have been several approaches using NW-based nanoelectronics to interface with cells and tissues. Metallic vertical NWs have been used as detectors to interface with the cells cultured directly on them. Electroporation was applied by 10 NWs to break

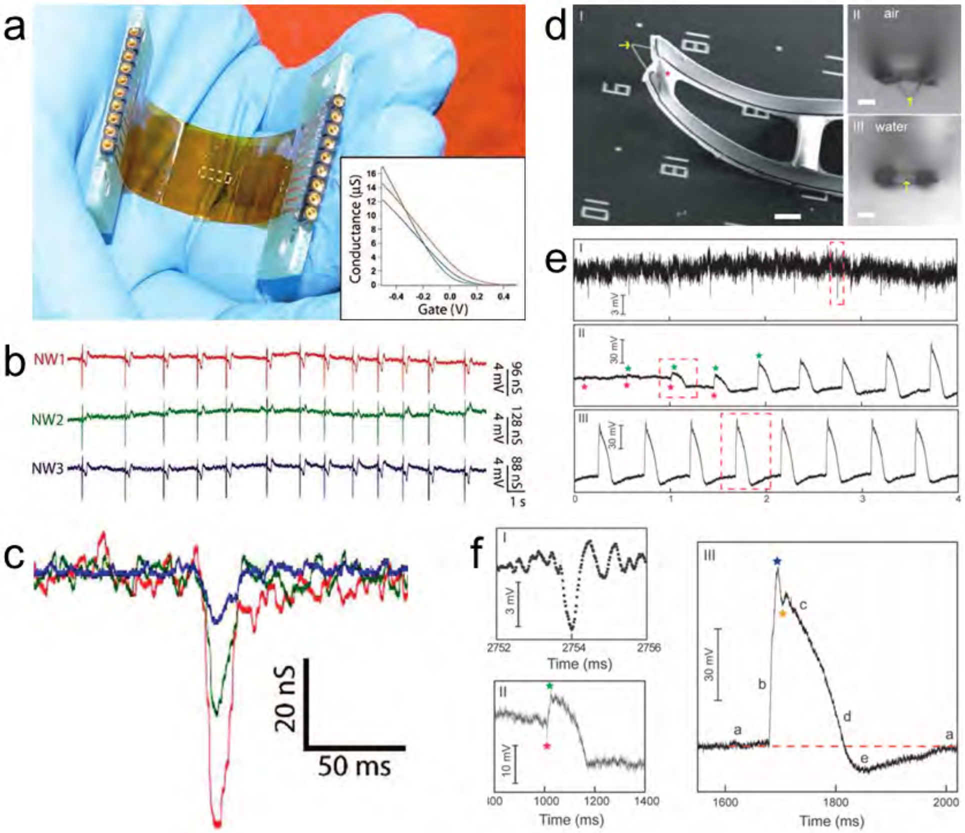

Figure 1.4: APs recording from flexible NW nanodevice. (a) Photograph of NW FET chip on a flexible Kapton substrate. The dashed white rectangle highlights the location of NW FET array. Inset: I–V_g measurements for three representative NW FET devices. (b) Multiplexed heart AP recorded at $V_\mathrm{g} = -0.2$ V. (c) Expansion of single AP measured at $V_\mathrm{g} = -0.4$ (red), 0 (green), and 0.4 V (blue). (Courtesy of ref. [29]) (d) SEM (I) and bright-field optical microscopy (II, III) images of a 3D free-standing kinked NW FET probe. The yellow arrow and pink star mark the nanoscale FET and SU-8, respectively. II and III are recorded in air and water, respectively. Scale bars: 5 mm. (e) Electrical recording from beating cardiomyocytes: (I) extracellular recording, (II) transition from extracellular to intracellular recordings, and (III) steady-state intracellular recording. Green and pink stars denote the peak positions of intracellular and extracellular signal components, respectively. (f) Zoom-in signals from the corresponding red-dashed square regions in (e). Blue and orange stars designate features that are possibly associated with inward sodium and outward potassium currents, respectively. The letters a to e denote five characteristic phases of a cardiac intracellular potential. The red-dashed line is the baseline corresponding to intracellular resting state. (Courtesy of ref. [10])

the cell membrane for a temporary interface between NW detectors and the intracellular environment. However, all these techniques are invasive procedures, which could introduce inevitable damage to cells or tissues.

On the contrary, the NW FET has proved to be a "non-invasive" and "active" detector with sensitivity intact while decreasing the detector size. Timko *et al.*[43] have demonstrated the fabrication of flexible and transparent NW FET arrays on thin polymer substrate for simultaneous optical imaging and electrical recording of beating embryonic chicken hearts (Figure 1.4a–c). A 50 µm thick flexible and transparent Kapton substrate containing NW FET arrays was bended to interface with whole heart with a convex configuration. Simultaneous multiplex measurements from three NW FETs on an isolated beating heart show correlated fast and slow phase peaks. The excellent signal-to-noise ratio further demonstrates the high performance of Si NW nanoelectronics. Tian *et al.*[10] synthesized kinked NW with ca. 80 nm diameter and modulated its axial doping to localize a lightly doped nanoscale FET region on the tip of the kink supported by two highly doped metallic arms. When stressed metal contacts were utilized, kinked NW sensors could be detached from supporting substrate and form a protruding 3D probe. Phospholipid bilayers were functionalized on the surface of the kinked NW to facilitate the penetration of the NW into the cell. Using this nanoscale FET probe, extracellular and intracellular cardiomyocyte APs was successfully recorded (Figure 1.4d–f).

Most reported nanoelectronics for interfacing cellular networks or tissues are limited at recording electrophysiological signals from the surface of tissues. However, tissues are 3D integrated constructions and the surface of tissue provides only limited information, therefore it will be more interesting and important to target the whole tissue in a 3D manner.

Optical methods used to visualize 3D tissues are mainly subject to small optical penetration depth due to light scattering as well as low temporal resolution compared to electronic approaches. Electronics inserted into tissues relied on rigid substrates will cause large damage to the tissue and also will lead to chronic damage due to the mechanical mismatch between rigid substrates and soft tissues, resulting in severe immunoreactivity and further degrading of interface. In order to build a seamless interface between 3D nanoelectronics and tissues for long-term and high-quality recording and intervention, conceptually new methods are desired.

1.4 Overview of the Dissertation

In this dissertation, I will first introduce a new approach for building 3D macroporous nanoelectronics in order to address the challenges described above. This 3D macroporous nanoelectronic network contains 3D continuous interconnection but depicts large porosity and flexibility. Individually addressable, nanoscale, multifunctional active elements were embedded to interface the surrounding environment around the networks. This macroporous nanoelectronic networks were firstly integrated with non-living materials for building "smart" materials which communication between interior and external environment can be achieved. Investigation and enhancement of long-term stability of NW elements embedded in the 3D nanoelectronic networks has been demonstrated in order to make it possible for integration of nanoelectronic networks with living tissues. This nanoelectronic networks mimics the flexible and macroporous structure of extracellular matrix of tissues and can function as tissue scaffolds. By culturing cells within this nanoelectronic network, nanoelectronics fully integrated tissues — "cyborg" tissues — can be built as a novel tissue model for spatiotemporal detection and intervention of tissue behavior. Pharmacological and pathological studies can be carried out based on cyborg tissue system for disease diagnostics and electronic therapeutics. Last, I will introduce further exploration of new type of nanodevice enabling new functionality.

In Chapter 2, I will introduce a new approach to fabricate 3D macroporous nanoelectronic networks. This 3D networks are initially fabricated in a two-dimensional (2D) form on top of a sacrificial layer. Using a contact printing assembly technique and lithography patterning, nanoelectronics base on NW arrays are patterned into polymeric networks. Removing the underlying sacrificial layer allows the 2D nanoelectronic network "precursors" to be organized into 3D structures by either external manipulation or internal stress.

In Chapter 3, I will introduce the integration of 3D nanoelectronic networks with other non-living materials such as polydimethylsiloxane (PDMS) and gel for building "smart" materials. In these "smart" materials, real-time monitoring of pH or strain field has been demonstrated through active nanodevices embedded in the 3D nanoelectronic networks.

In Chapter 4, I will introduce a general method to increase the long-term stability of NW elements in the physiological environments by coating a thin layer of Al_2O_3 on the surface of NWs. These NW/Al_2O_3 core/shell structures exhibits stability for at least 100 days in physiological solutions at 37 °C, which promises the biological applications of NW nanoelectronics for chronic *in vivo* and *in vitro* studies.

In Chapter 5, I will introduce the fabrication "cyborg" cardiac tissue by culturing cardiac tissues within demonstrated 3D macroporous nanoelectronic scaffolds. We have successfully fabricated more than a hundred NW FETs with subcellular footprint to achieve a sub-millisecond time resolution mapping of cardiac APs in 3D. The cyborg cardiac tissue has been used to investigate tissue maturation process in real-time, and to visualize the 3D spatiotemporal electrophysiological behaviors with drugs modulation, including norepinephrine and 1-heptanol, demonstrating the cyborg cardiac tissue as a powerful tool for drug testing.

In Chapter 6, I will introduce a ventricle arrhythmia model based on cyborg cardiac tissues. In addition, incorporation of electrical stimulator has been demonstrated to artificially control the AP conduction pattern of cardiac tissue. With simultaneous detection and intervention of cardiac electrophysiological behaviors based on 3D macroporous nanoelectronic scaffold, it shows a great promise for novel disease diagnostics and electronic therapeutics.

In Chapter 7, I will further explore a new type of nanodevice using 3D nanocombing technique. Convex NW components can be assembled and fabricated to achieve simultaneous recording of extracellular APs and contraction force from individual cardiomyocyte.

2

Multifunctional Three-dimensional Macroporous Nanoelectronics

2.1 Introduction

The integration of 3D electronics within host materials in a seamless and minimally invasive way could potentially enable "smart" materials systems that are self-monitoring and capable of communication between materials and environments. For example, embedded electronic sensor circuitry could monitor chemical, mechanical, or other changes throughout the host material, thus providing detailed information about the host materials[11, 52]. On the other hand, it can also provide desired feedback to interfere with the host materials and external environments. In order to achieve the seamlessly merging of functional electronic elements with host materials, the addressable electronic networks must be macroporous, not planar, to enable 3D interpenetration with the host materials. Second, to minimize invasiveness of the macroporous electronic network it must have (1) microscale-to-nanoscale feature sizes, (2) a small filling ratio with respect to the host (e.g., $<1\%$), (3) comparable or softer mechanical properties than the host, and (4) an inert chemical response in the host material.

The constraints outlined above require the utilization of 3D nanoelectronic networks that are macroporous and have active elements (nanodevices). Two basic methods have been used to fabricate 3D integrated electronic circuits: the first involves bonding substrates, each containing devices/circuits integrated in 2D, together in a 3D stack[53], and the second exploits bottom-up assembly of nanoelectronic elements in a layer-by-layer manner[39, 41, 54]. However, both methods yield solid or nonporous 3D structures that only allow the top layer of electronic elements to interface directly with a second material thus precluding integration of all of the electronic elements seamlessly with a host material in 3D. In this chapter, I will introduce a general strategy for preparing 3D integrated electronic systems, which are ordered 3D interconnected and addressable macroporous nanoelectronic networks. This 3D macroporous nanoelectronic network is made from ordered 2D NW nanoelectronic network "precursors", which are fabricated by conventional lithography technique.

2.2 Fabrication of Multifunctional Three-dimensional Macroporous Nanoelectronics

We have focused on a bottom-up approach for realizing 3D macroporous nanoelectronic networks as outlined schematically in Figure 2.1. First of all, we use functional NW nanoelectronic elements (Figure 2.1a) in this approach, where variations in composition, morphology, and doping encoded during synthesis[27, 29, 30, 32, 55, 56] define diverse functionality including devices for logic and memory[31, 57], sensors[10, 33], light-emitting diodes[32], and energy production and storage[58, 59]. Second, the macroporous nanoelectronic network with chosen NW elements (Figure 2.1b) is realized through a combination of NW assembly and conventional 2D lithography carried out on a sacrificial substrate; removal of the sacrificial layer yields free-standing and flexible 2D macroporous nanoelectronic networks (Figure 2.1b). Third, the 2D macroporous nanoelectronic networks are organized into 3D macroporous structures by either self-assembly or directed-assembly.

The NW elements were synthesized by CVD method on SiO_2/Si substrates, which were later transferred onto device fabrication substrates using contact-printing method. First of all, gold nanoparticles (Ted Pella Inc.) with 30 nm diameters were dispersed on the oxide surface (600 nm thickness) of SiO_2/Si substrates and placed in the central region of a quartz tube in CVD reactor system. Uniform 30 nm p-type Si NWs were synthesized using reported methods. In a typical synthesis process, the total pressure was set to be 40 torr, and the flow rates of SiH_4, B_2H_6 (100 ppm in H_2), and H_2, (Semiconductor Grade) were 2, 2.5, and 60 standard cubic centimeters per minute (s.c.c.m.), respectively. The Si:boron feed-in ratio was 4000:1, and the total NW growth time was 30 min.

The key steps involved in the fabrication of the macroporous nanoelectronic networks are outlined in Figure 2.2. (1) Lithography and thermal deposition were used to pattern a

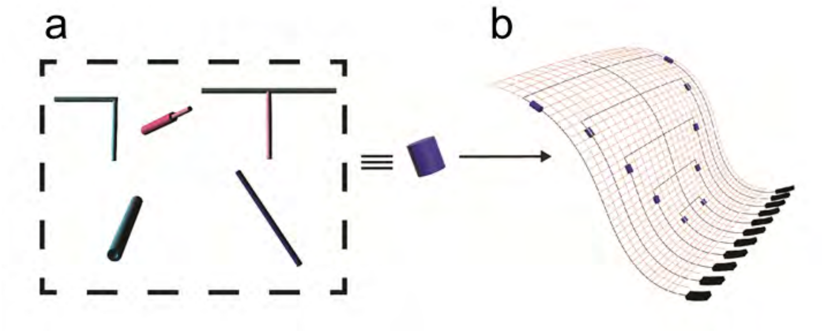

Figure 2.1: Strategy for preparing 3D macroporous nanoelectronic networks. (a) Different NW nanoelectronic elements (from left to right): kinked NW, nanotube, core-shell, straight and branched NW. (b) Free-standing 2D macroporous NW nanoelectronic "precursor". Blue: nanoelectronic element, orange: passivation polymer, black: metal contact and I/O.

100 nm Ni metal layer, where the Ni served as the final relief layer for transforming 2D macroporous NW nanoelectronic networks into free-standing. (2) A 300 to 500nm layer of SU-8 negative photoresist (2000.5, MicroChem Corporation) was deposited over the entire chip by spin-coating, followed by prebaking at 65 °C and 95 °C for 2 and 4 min, respectively, then (3) the synthesized NWs were directly printed from growth substrates onto the SU-8 layer by the contact printing (Figure 2.2a, I). (4) Lithography (photolithography or electron-beam lithography) was used to define regular patterns on the SU-8. After postbaking (65 °C and 95 °C for 2 and 4 min, respectively), SU-8 developer (MicroChem Corporation) was used to develop the SU-8 pattern. Those areas exposed to UV light or electron beam became dissolvable to SU-8 developer, and other areas were dissolved by SU-8 developer. The NWs on the unexposed area will be removed by further twice washing in isopropanol (30 s), leaving those selected NWs on the regular pattern SU-8 structure (Figure 2.2a, II). The SU-8 patterns were cured at 180 °C for 20 min. The NW density and feature size in periodic arrays were chosen such that each element contained on aver-

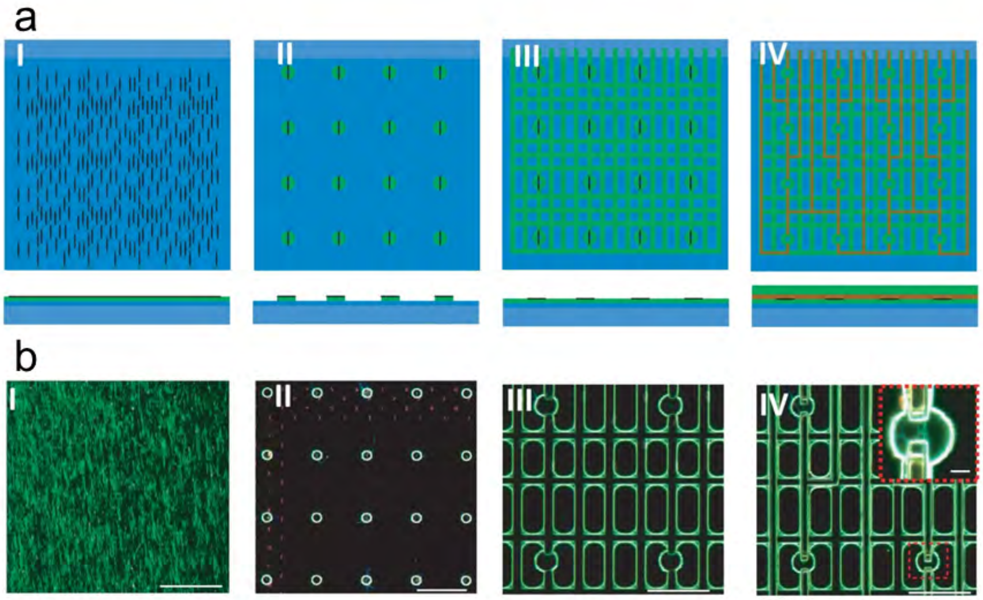

Figure 2.2: Organized 2D macroporous nanoelectronic networks precursors. (a) Schematics of NW registration by contact printing and SU-8 patterning. Gray: Si wafer; Blue: Ni sacrificial layer; Black ribbon: NW; Green: SU-8 negative photoresist; Red: metal contact. Top images show the top views and bottom images show side views. I, NWs assembled on SU-8 via contact printing. II, Regular SU-8 structure was patterned by lithography to immobilize NWs. Extra NWs were washed away during the develop process of SU-8. III, Regular bottom SU-8 structure was patterned by spin coating and lithography. IV, Regular metal contacts were patterned by lithography and thermal evaporation, followed by top SU-8 passivation. (b) Dark-field optical images corresponding to each step of schematics in (a). The NW and SU-8 features appear green in these images. The small red features on the right and lower edges of the image in (b), II correspond to markers used for alignment. The red dashed line highlights metal contacts/interconnects in (b), IV.

age 1–2 NWs. (5) Another 300 to 500 nm layer of SU-8 photoresist was deposited over the entire chip followed by prebaking at 65 °C and 95 °C for 2 and 4 min, respectively. Then lithography was carried out to pattern the bottom SU-8 (Figure 2.2a, III) and then the structure was postbaked, developed, and cured by the same procedure as described above. layer for passivating and supporting the whole device network structure. The SU-8 network serves to interconnect the NW/SU-8 periodic patterns, provides a desirable support and back passivation for the metal interconnections that will be deposited on top. (6) Lithography and thermal deposition were used to define and deposit the metal contact to address each NW device and form interconnections to the input/output pads. Each NW elements were independently addressed (Figure 2.2a, IV). For the mesh networks, in which the metal is non-stressed, symmetrical Cr/Pd/Cr (1.5/50–80/1.5 nm) metal were sequentially deposited followed by metal lift-off in acetone. For the self-organized networks, in which the metal is stressed, nonsymmetrical Cr/Pd/Cr (1.5/50–80/50–80 nm) metal were sequentially deposited followed by metal lift-off in acetone. (7) A 300 to 500 nm layer of SU-8 photoresist was deposited over the entire chip, followed by prebaking at 65 °C and 95 °C for 2 and 4 min, respectively. Then lithography was used to pattern the top SU-8 layer for passivating the metal interconnects for the whole device structure. The structure was postbaked, developed, and cured by the same procedure as described above.

Dark-field optical micrographs of a typical nanoelectronic mesh network fabrication corresponding to each steps described above (Figure 2.2b, I–IV) were acquired on an Olympus FSX100 system using FSX-BSW software to highlight several important features. First, the images recorded after contact printing (Figure 2.2b, I) confirm that NWs are well aligned over areas where NW devices are fabricated. We can achieve good NW alignment on length

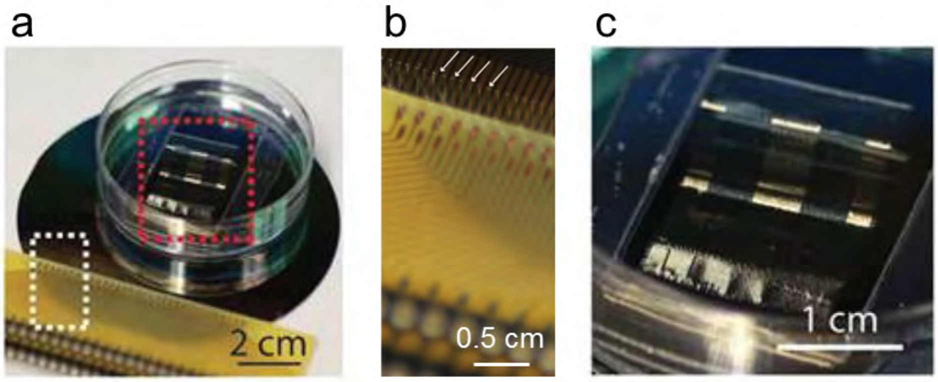

Figure 2.3: Free-standing 2D macroporous nanoelectronic networks. (a) Photograph of wire-bonded free-standing 2D macroporous nanoelectronic network in petri-dish chamber. The white-dashed box encloses the wire-bonded interface between the I/O and printed circuit board (PCB) connectors and the red dashed box highlights the free-standing portion of the nanoelectronic networks. (b) Zoom-in of the region enclosed by the white dashed box in (a). The white arrows highlight several wire bonding points between the PCB connectors and metal pads in the I/O region of the macroporous nanoelectronic networks. (c) Zoom-in of the region enclosed by the red-dashed box in (a), showing the free-standing 2D macroporous nanoelectronic networks in aqueous solution.

scales up to at least several centimeters, as reported elsewhere. Second, a representative dark-field image of the patterned periodic NW regions (Figure 2.2b, II) shows that this process removes nearly all of the NWs outside of the desired features. NWs can be observed to extend outside of the periodic circular feature with one end fixed within the feature; however, these are infrequent and do not affect subsequent steps defining the nanodevice interconnections. Third, images of the underlying SU-8 mesh (Figure 2.2b, III) and final device network with SU-8 passivated metal contacts and interconnects (Figure 2.2b, IV) highlight the regular array of addressable NW devices realized in the fabrication processes.

In order to convert 2D nanoelectronic mesh networks in to 3D configuration, The 2D macroporous NW nanoelectronic networks were released from the substrate by etching of the Ni relief layer (Nickel Etchant TFB; Transene Company Inc.) for 60–120 min at 25 °C. Then the 3D free-standing macroporous NW nanoelectronic networks were dried by a critical point dryer (Autosamdri 815 Series A, Tousimis). Representative images of a free-standing nanoelectronic network (Figure 2.3) highlight the 3D and flexible characteristics of the network structure and show how input/output (I/O) parts of the free-standing networks can be fixed at one end while the other free-standing parts can still be kept in the solution of a petri-dish chamber for further manipulation and integration.

These 2D free-standing macroporous nanoelectronic networks can be transformed into 3D configurations using two general methods. First, 2D macroporous nanoelectronic networks can be manually rolled up into 3D structures (Figure 2.4a), with nanoelectronic elements in different layers of the resulting “scroll”. Second, by introducing built-in stress in metal interconnections with a triple layer metal stack, the mesh can be designed to self-organize into a similar scrolled structure as achieved by manual rolling. A reconstructed 3D

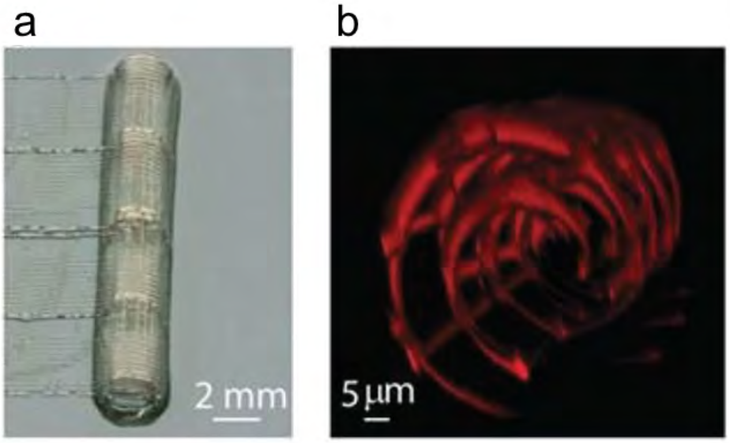

Figure 2.4: 3D macroporous nanoelectronic networks structures. (a) Photograph of a manually scrolled-up 3D macroporous nanoelectronic network. (b) 3D reconstructed confocal fluorescence images of self-organized 3D macroporous nanoelectronic network viewed from side. Nonsymmetrical Cr/Pd/Cr metal layers, which are stressed, were used to drive self-organization. The SU-8 ribbons were doped with Rodamine-6G for fluorescent imaging.

confocal fluorescent image of a 3D nanoelectronic mesh array configured in this manner (Figure 2.4b) shows clearly the 3D macroporous nanoelectronic network and can be used to estimate a void volume of >99%. Fluorescence images of the 3D macroporous nanoelectronic networks were obtained by doping the SU-8 resist with rhodamine-6G (Sigma-Aldrich Corporation) at a concentration of <1 µg/mL before spin-coating and patterning. More generally, these self-organized 3D macroporous nanoelectronic networks could be readily diversified to meet goals for integration with different hybrid materials.

2.3 Characterization of Multifunctional Three-dimensional Macroporous Nanoelectronics

The 3D macroporous nanoelectronic networks consist of single-layer polymer (SU-8) structural and three layer ribbon (SU-8/metal/SU-8) interconnect elements. The effective bending stiffness per unit width of the 3D macroporous nanoelectronic networks can be estimated by Eq. 2.1

$$\overline{D} = a_\mathrm{s} D_\mathrm{s} + a_\mathrm{m} D_\mathrm{m} \tag{2.1}$$

where a_s and a_m are the area fraction of the single-layer polymer and three-layer interconnect ribbons in the networks. $D_\mathrm{s} = E_\mathrm{s} h^3/12$ is the bending stiffness per unit width of the single-layer polymer, where $E_\mathrm{s} = 2$ GPa and h are the modulus and thickness of the SU-8. For a SU-8 ribbon with 500 nm thickness, D_s is 0.02 nN m. D_m is the bending stiffness per unit width of a three-layer structure, which includes 500 nm lower and upper SU-8 layers and 100–130 nm metal layer, and was measured experimentally using an atomic force microcope (AFM) (MFP 3D, Asylum Corporation) system with a calibrated AFM tip as described below.

A Ni sacrificial layer was defined on a SiO_2/Si substrate by electron beam lithography and thermal deposition. SU-8/metal/SU-8 elements with 100 µm long and 5 µm wide segments over the Ni layer were defined by electron beam lithography using the same approach as described above. In brief, a 500 nm thick SU-8 layer was deposited by spin coating and defined by lithography to serve as the bottom SU-8 layer. Then lithography, thermal deposition, and lift-off were used to define an asymmetrical metal layer consisting of a 3 µm wide Cr/Pd/Cr (1.5/80/50 nm) ribbon centered on the bottom SU-8 element.

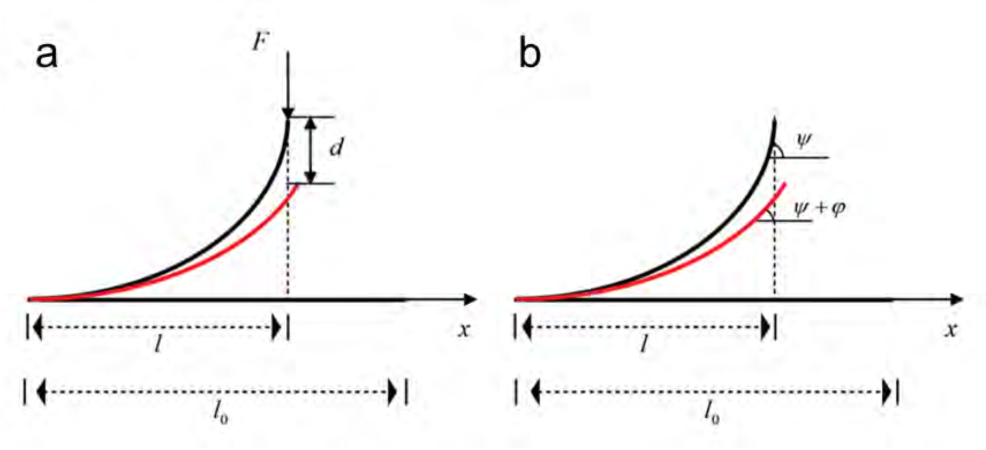

Figure 2.5: Schematics for bending stiffness calculation. (a) A schematic of the position of a free-standing beam before (black) and after (red) applying a calibrated force, F , and vertical displacement, d , at the end of the beam measured by AFM. (b) The angle between the tangential direction of a material point on the beam and the horizontal direction, ψ , of the ribbon before (black) and after displacement, $\psi + \varphi$, (red). l_0 : the total length of the ribbon. l : projection of the ribbon.

Last, the top 500 nm thick SU-8 layer of the SU-8/metal/SU-8 elements were defined, and then the Ni sacrificial layer was removed by Ni etchant, where the final drying step was carried out by critical point dryer. An AFM was used to measure force vesus displacement curves for the SU-8/metal/SU-8 elements. The tip of the AFM was placed at the free end of the ribbon element, and then the applied force and displacement were recorded while the AFM tip was translated down (loading) and then up (unloading). The spring constant of the AFM cantilever/tip assemblies used in the measurements were calibrated by measuring the thermal vibration spectrum.

Qualitatively, the facile manipulation of the macroporous nanoelectronic networks to form 3D structures suggests a very low effective bending stiffness. We have evaluated the effective bending stiffness, $\overline{D}$, using a combination of calculations and experimental measurements. Due to the residual stress, The SU-8/metal/SU-8 elements bend upward from the substrate (due to internal stress of the asymmetric metal layers) with a constant curvature, K_0 , and projected length, l, where l_0 is the free length defined by fabrication. We use the curvilinear coordinate s to describe the distance along the curved ribbon from the fixed end, and the coordinate x to describe the projection position of each material point of the ribbon (Figure 2.5a). For a specific material point with distance s , the projection position x can be calculated as $x = \int \cos \psi ds$, where $\psi = K_0 s$ is the angle between the tangential direction of the curvilinear coordinate s and the horizontal direction (Figure 2.5b). Integration yields $x = \sin(K_0 s)/K_0$ and when $x = l$ and $s = l_0$, $K_0 = 0.0128$ μm^{-1} for typical experimental parameters $l_0 = 100$ μm and $l = 75$ μm.

Because the element is deflected a distance d by the AFM tip with a force F, each material point is rotated by an angle, φ (Figure 2.5b), where the anticlockwise direction is defined as positive. Assuming a linear constitutive relation between the moment M and curvature change $d\varphi/ds$ yields

$$\frac{d\varphi}{ds} = \frac{M}{wD_{\text{m}}} \tag{2.2}$$

where M is the moment as a function of position, x (Figure 2.5), and w is the width.

$$M(x) = xF(l - x) \tag{2.3}$$

Solving for the bending stiffness, D_{m} , with the assumption that φ is small so that $\sin \varphi \simeq \varphi$

yields:

$$D_{\mathrm{m}} = \frac{F}{wd}\left[\frac{ll_0 \sin(K_0 l_0)}{K_0} + \frac{1}{K_0^2}\left(l\cos(K_0 l_0) - l + \frac{l_0}{2}\right) + \frac{1}{K_0^3}\left(\frac{\sin(2K_0 l_0)}{4} - \sin(K_0 l_0)\right)\right] \tag{2.4}$$

The slope of a representative loading force-deflection curve yields $F/d = 12$ nN/μm, and using Eq. (2.4), the calculated bending stiffness per width ($w = 5$ μm) is $D_{\mathrm{m}} = 0.358$ nN m. For typical 3D macroporous nanoelectronic networks, the area fraction for both types of elements (i.e., SU-8 and SU-8/metal/SU-8) can range from 1% to 10%, yielding values of the effective bending stiffness from 0.0038 to 0.0378 nN m.

Electrical characterization of NW device was carried out with a 100 mV DC source voltage, and the current was amplified with a home-built multichannel current/voltage preamplifier with a typical gain of 10^6 A/V. The signals were filtered through a home-built conditioner with bandpass of 0–6 kHz, digitized at a sampling rate of 20 kHz (Digidata 1440A; Molecular Devices, Axon Laboratory), and recorded using pClamp (ver. 10.2, Molecular Devices, Axon Laboratory). I–V measurement of individually addressable NW devices in a free-standing 2D macroporous nanoelectronic network demonstrates that the device yield is typically ∼90% (from 128 device design). The statistics of the electrical measurement demonstrates an average conductance of the devices from a representative free-standing mesh to be 2.85 ± 1.60 μS, which is consistent with 1–2 NWs per device based on measurements of similar (30 nm diameter, 2 μm channel length) p-type Si single NW devices, and thus also agrees with the structural image discussed above.

2.4 Conclusion

In this chapter, I have introduced a general strategy for preparing ordered 3D interconnected and addressable macroporous nanoelectronic networks from ordered 2D NW nanoelectronic “precursors”, which can be fabricated by conventional lithography technique. The 3D networks have porosity larger than 99%, contain 100’s of individually addressable NW devices, and have feature sizes from the 10 μm scale (for electrical and structural interconnections) to 10 nm scale (for the functional NWs) device elements. The network is extremely flexible with effective bending stiffness from 0.0038 to 0.0378 nN m, which is the most flexible electronics reported.

3

Nanoelectronic Scaffolds for Building “Smart” Materials

3.1 Introduction

Seamless integration of electronics with host materials could transfer inactive materials into active materials, which allow the communication between the materials and external environment, and implement multifunction from nanoelectronics into host materials to create a “smart” system. Traditional electronics are planar and rigid, however, most materials and systems in our daily life are 3D and non-planar. To overcome this issue, flexible electronics have been developed to cover on the surface of other systems to implement the functions into host materials. However, those surface electronics are still not able to detect the property change through the whole materials in 3D and provide a full range of control. People can implant the rigid probe into those materials. However, those methods are invasive. The mechanical mismatch between those probes and materials cause further break during the implementation[6–8]. Herein, we introduce a general strategy to 3D integration of electronics described in Chapter 2 with host materials and also show how these electronic networks in the host materials can be used to map chemical and mechanical changes induced by the external environment in 3D.

The 3D macroporous nanoelectronic networks described in Chapter 2 have porosities larger than 99%, contain approximately hundreds of addressable NW devices, and have feature sizes from the 10 μm scale to the 10 nm scale. The macroporous nanoelectronic networks were merged with organic gels and polymers to form hybrid materials in which the basic physical and chemical properties of the host were not substantially altered, and electrical measurements further showed a >90% yield of active devices in the hybrid materials. The semiconductor NW elements can display multiple sensory functionalities, including photon[60], chemical, biochemical[33], and potentiometric as well as strain detection[61], which make them particularly attractive for building active elements in the 3D macroporous nanoelectronic networks.

In this chapter, I will first introduce the 3D photodetection within hybrid materials using 3D macroporous nanoelectronic networks. Relying on the photocurrent measurement, the positions of the NW devices were located within 3D hybrid materials with ∼14 nm resolution. In addition, we explored functional properties of these hybrid materials, including (1) mapping time dependent pH changes throughout a NW network/agarose gel sample

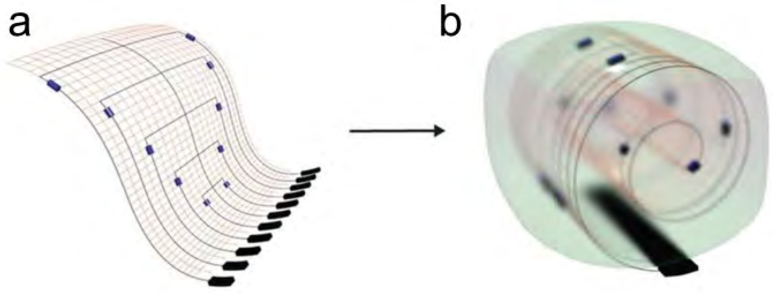

Figure 3.1: Strategy for integration of 3D macroporous nanoelectronic networks with host materials. (a) Free-standing 2D macroporous NW nanoelectronic networks. Blue: Nanoelectronic element; Orange: Passivation polymer; Black: Metal contact and I/O. (b) 3D macroporous nanoelectronic networks integrated with host materials (Green).

during external solution pH changes, and (2) characterizing the strain field in hybrid nanoelectronic elastomer structures subject to uniaxial and bending forces. The seamless incorporation of active nanoelectronic networks within 3D materials reveals a powerful approach towards "smart" materials in which the multifunctional nanoelectronics allow for active monitoring and controlling of host systems.

3.2 Three-dimensional Nanoelectronic Scaffolds for Photodection and Device Localization

The 3D macroporous nanoelectronic networks were used to seamlessly merge with host materials samples using a solution (or liquid) casting process at or near room temperature (Figure 3.1). For instance, a free-standing 2D macroporous nanoelectronic network can be placed on a thin (200–500 μm) piece of cured silicone elastomer sheet (Sylgard 184; Dow Corning). The hybrid macroporous NW network/Si elastomer can be then rolled into a cylinder, infiltrated with uncured silicone elastomer, vacuumed, and cured at 70 °C for 4

h. The resulting hybrid silicone elastomer cylinders had volumes of ∼300 mm^3 with only <0.1% volume occupied by rolled 3D macroporous nanoelectronic networks.

We first characterized photoconductivity changes (i.e., photon detection) of NW elements using a confocal laser scanning microscopy (FluoView FV1000; Olympus America Inc.). NW FETs are being recorded while simultaneously fluorescence images were acquired (Figure 3.2a). The hybrid materials were immersed into deionized (DI) water and imaged under 40× or 100× water immersion objectives. The SU-8 structure was doped with rhodamine-6G for fluorescence imaging. Conventional 405 nm and 473 nm wavelength lasers were used, with 405 nm to produce photocurrents in the NW FET devices, and 473 nm for fluorescence imaging. NW FETs were biased at 100 mV. The photocurrent signal was amplified (SIM 918; Stanford Research System) bandpass filtered (1 Hz–6 kHz, home-built system), and synchronized with laser scanning position using an analog signal input box (F10ANALOG; Olympus America Inc.). The conductance signal from the resulting images was read and analyzed by ImageJ (ver. 1.48v, Wayne Rasband, National Institutes of Health) and OriginPro (ver. 8.1, Origin Lab Corporation).

As the focused laser is scanned across a sample (Figure 3.2a) an increase of conductance due to the photocurrent in NW is recorded when laser spot is on the NW. In addition, we have acquired simultaneous photoconductivity and fluorescence confocal microscopy images in order to locate the positions of NW devices within hybrid 3D materials. Reconstructed 3D images (Figure 3.2b) show that the 12 active NW devices can be readily mapped with respect to x–y–z coordinated in the rolled-up macroporous nanoelectronic network structure. Given the complexity possible in 3D nanoelectric/host hybrid materials, this approach provides straight forward methodology for determining the positions

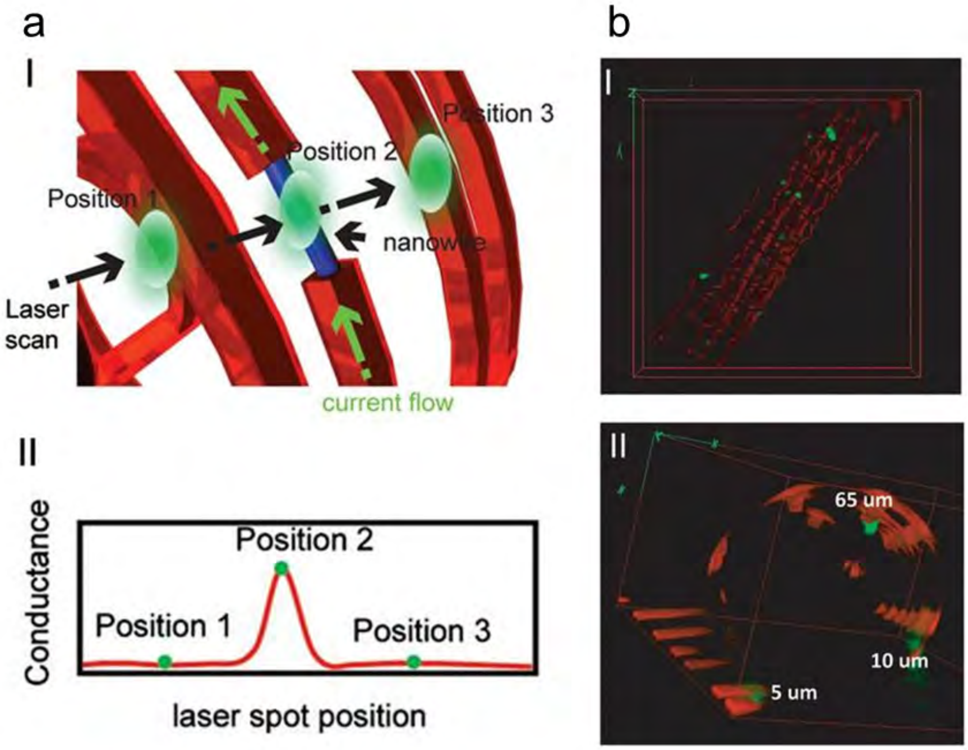

Figure 3.2: 3D macroporous photodetectors and device localization. (a) Schematics of the single 3D macroporous NW photodetector characterization. The green ellipse: Laser spot; Blue cylinder: NW; Orange: SU-8 mesh network. The illumination of the laser spot generated from confocal microscope on the NW device (I) makes the conductance change of NW, which could be (II) correlated with laser spot position. Green spots in (II) correlate to the laser spot positions in (I). (b) 3D reconstructed photocurrent imaging overlapped with confocal microscopy imaging shows the spatial correlation between NW photodetectors with SU-8 framework in 3D. Green: False color of the photocurrent signal; Orange (rhodamine-6G): SU-8 mesh network. Dimensions in (I) are x: 317 μm; y: 317 μm; z: 53 μm; and in (II) are x: 127 μm; y: 127 μm; z: 65 μm. The white numbers in (II) indicate the heights of the NW photodetectors.

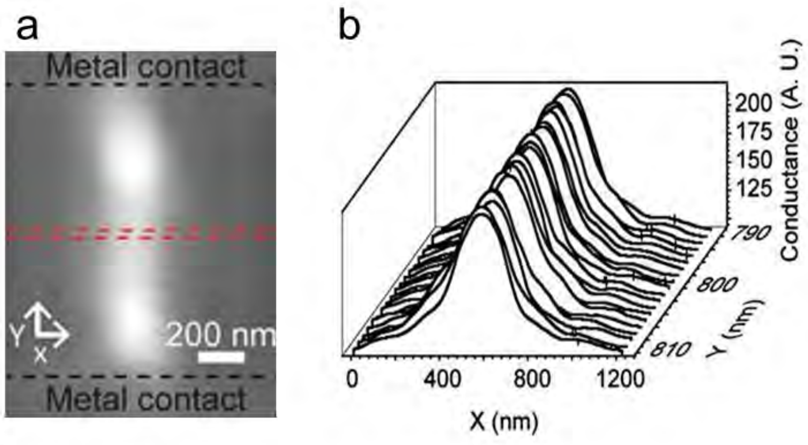

Figure 3.3: Spatial resolution of device localization in 3D hybrid materials. (a) High-resolution (1 nm per pixel) photocurrent image from single NW device (2 μm channel length) on substrate recorded with focused laser spot scanned in x–y plane. The black dash lines indicate the boundary of metal contact in the device. (b) 20 times photocurrent measurements from the red dash box in (a) of the NW device with high resolution (the distance for each trace in x-direction is 1 nm).

of the active nanoelectronic sensory elements with respect to structures within the host materials.

The resolution of the spatial localization can be assessed in two ways. Conventionally, the plot of conductance versus x position perpendicular to the NW axis (Figure 3.2a, II) can be fit with a Gaussian function, and its full-width at half-maximum (FWHM) reflects the diffraction limited resolution of the illuminating light spot. For our case, it is 314 ± 32 nm ($N = 20$), which is consistent with confocal microscopy imaging resolution (202 nm). Second, we can use methods similar to superresolution imaging technologies to locate the NW at a much higher precision by identifying the peak position from the Gaussian fit, recognizing that the NW is line-like and the diameter is ~30 nm. The NW position determined from the peaks of Gaussian fits (Figure 3.3) yielded a standard deviation of 14 nm

($N = 20$), and shows that the position of devices can be localized with a precision better than the diffraction limit. We note that a similar concept as exploited in stochastic super-resolution imaging to resolve close points can be implemented in our photoconductivity maps because individual devices can be turned on and off as needed.

3.3 Three-dimensional Nanoelectronic Scaffolds for pH sensing

Second, we have used macroporous NW nanoelectronic networks to map pH changes in 3D through agarose gel using a macroporous nanoelectronic/gel hybrid, and for comparison, in aqueous solution using a free-standing 3D nanoelectronic sensory network. The hybrid nanoelectronic/gel material was prepared by casting the agarose around a rolled-up macroporous nanoelectronic network. Agarose (Sigma-Aldrich Corporation) was dissolved into DI water, made as 0.5%, and heated up to 100 °C. The gel was drop-cast onto the device and cooled to room temperature. 4',6-diamidino-2-phenylindole (DAPI) (Molecular Probes, Invitrogen) was used to dope the gel for the confocal 3D reconstructed imaging. A microfluidic PDMS chamber with I/O tubing and Ag/AgCl electrodes was sealed with the Si substrate and the device or device/gel hybrid using silicone elastomer adhersive (Kwik-Sil; World Precision Instruments). SU-8 mesh of the nanoelectronic network were doped with rhodamine-6G. A reconstructed 3D confocal microscopy image of the hybrid material (Figure 3.4a) shows clearly the 3D device mesh fully embedded within an agarose gel block without phase separation.

To carry out sensing experiments, either the 3D nanoelectronic/gel hybrid material or a 3D nanoelectronic mesh was contained within a microfluidic chamber (Figure 3.4b). Fresh medium was delivered to the device region through both inner and outer tubing. The so-

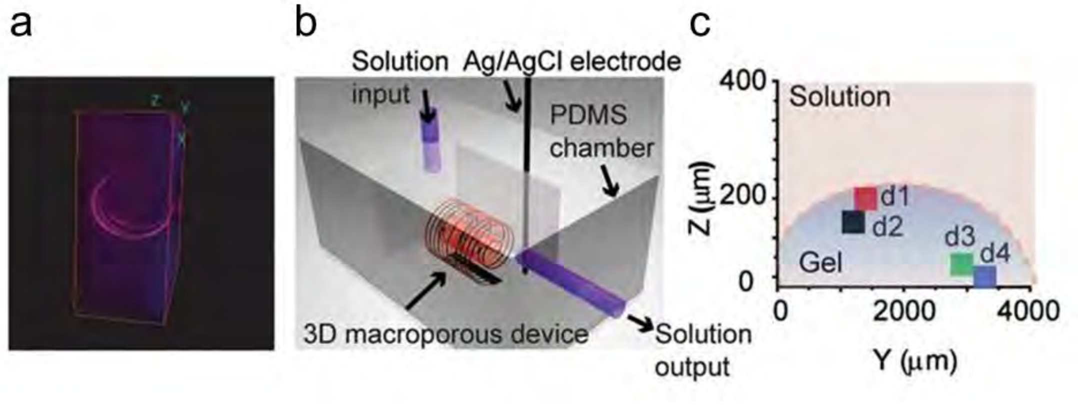

Figure 3.4: The 3D macroporous chemical sensors ambedded in gel. (a) The x–z view of 3D reconstructed image of the 3D macroporous nanoelectronic network in gel. Red (rhodamine-6G): SU-8 mesh network; Blue (DAPI): agarose gel. Dimensions: x = 317 μm; y = 317 μm; and z = 144 μm. (b) Schematic of the experimental setup. (c) The projection of four NW devices in the y–z plane. Red dashed line corresponds to the approximate gel boundary, and the red and blue areas correspond to aqueous solution and agarose gel, respectively.

lution pH was varied stepwise inside the channel by flowing (20 mL/h) 1× phosphate buffered saline (PBS) with fixed pH values from 6.0 to 8.0. The recorded device signals were filtered with a bandpass filter of 0–300 Hz. Positions of NW FET devices, which can function as very sensitive chemical/biological detectors, were determined by the photocurrent mapping method described above. For both 3D nanoelectronic networks and nanoelectronic/gel hybrid materials, we recorded signals simultaneously from four devices chosen to span positions from upper to lower boundary of mesh or gel, where representative z-coordinates of the devices positions within the hybrid sample are highlighted in Figure 3.4c; a similar z-range of devices for the free nanoelectronic mesh was also used.

Representative data recorded from p-type NW FET devices in 3D mesh network without gel (Figure 3.5a, I) and in the hybrid 3D nanoelectronic mesh/agarose gel materials (Figure 3.5a, II) highlight several important points. First, the device within 3D macrop-

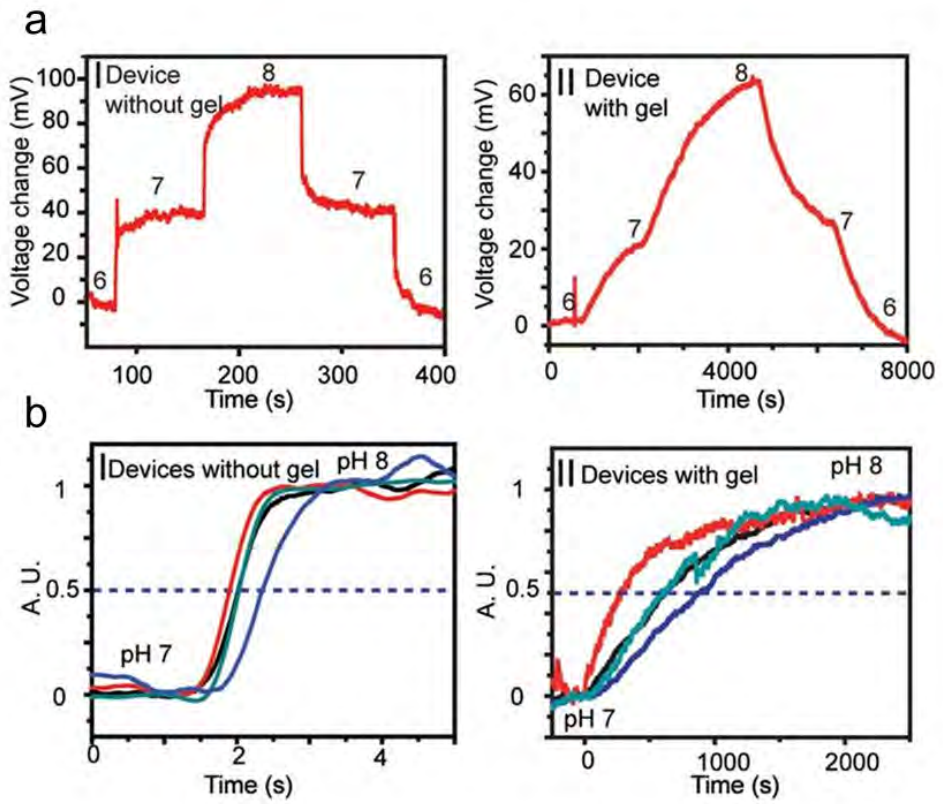

Figure 3.5: 3D mapping of pH gradient in macroporous nanoelectronic network/gel hybrid structure. (a) Representative change in calibrated voltage over time with pH change for 3D macroporous NW chemical sensors (I) in solution and (II) embedded in agarose gel. (b) Calibrated voltage with unit pH value change in solution for four different devices located in 3D space. (I) Four devices without gel and (II) four devices embedded in agarose gel.

orous network without gel showed fast stepwise conductance changes (<1 s) with solution pH changes. The typical sensitivity of these devices was $\sim$40 mV/pH, and is consistent with values reported for similar NW devices. Second, the device within the 3D nanoelectronic mesh/gel hybrid exhibited substantially slower transition times with corresponding changes of the solution pH; that is, signal change required on the order of 2000 s to reach steady state, and thus was 1000-fold slower than in free solution. Third, the device within the 3D nanoelectronic mesh/gel hybrid exhibited lower pH sensitivity in terms of mV/pH; that is, 20–40 mV/pH for the device in gel compared with 40–50 mV/pH for the device in free solution. Direct comparison of the temporal responses of four devices at different 3D positions in the two types of samples (Figure 3.5b) provides additional insight into the pH changes. The time to achieve half-unit pH change for the four different devices in 3D macroporous network without gel (Figure 3.5b, I) is $\sim$0.5 s with difference between devices as only $\sim$0.01 s. We note that the time delay in the data recorded from device d4 is consistent with the downstream position of this device within the fluidic channel. In contrast, the time to achieve half-unit pH change for the four devices in the 3D nanoelectronic mesh/gel hybrid (Figure 3.5b, II) range from 280 to 890 s for devices d1–d4, respectively (Figure 3.4c). The results show that the device response time within the agarose is 500–1700 times slower than in solution and is proportional to the distance from the solution/gel boundary, although the detailed variation suggests heterogeneity in the diffusion within the agarose gel. Significantly, the ability to map the diffusion of molecular and biomolecular species in 3D hybrid systems using the macroporous nanoelectronic sensory networks offers opportunities for self-monitoring of gel, polymers, and tissue systems relevant to many areas of science and technology.

3.4 Three-dimensional Nanoelectronic Scaffolds for Strain Sensing

Third, we have used embedded 3D macroporous nanoelectronic networks to map strain distributions in elastomeric silicone host materials. Previous studies have shown that Si NWs have a high piezoresistance response, making them good candidates for strain sensors. To explore the potential of Si NW device arrays to map strain within materials, we have prepared and characterized 3D macroporous nanoelectronic network/elastomer hybrid materials. The resulting hybrid macroporous nanoelectronic network/elastomer cylinders had volumes of $\sim$300 mm^3 with volume ratio of device to elastomer of $<0.1\%$. The structure of the macroporous electronics/elastomer hybrid was determined using a HMXST X-ray micro-CT system with a standard horizontal imaging axis cabinet (HMXST225; Nikon Metrology Inc.). In a typical imaging experiment, the acceleration voltage was 60–70 kV, the electron beam current was 130–150 mA, and no filter was used. BGStudioMAX (ver. 2.0; Volume Graphics GmbH) was used for 3D reconstruction and analysis of the micro-CT images, which resolve the 3D metal interconnect structure and NW S/D contacts; the Si NWs were not resolved in these images but were localized at the scale of the S/D contacts (Figure 3.6a). The alignment of NW elements along the cylinder axis was confirmed by dark-field optical microscopy images (Figure 3.6b), which show the NWs lying along the cylinder (z) axis. The good axial alignment of the NW devices was exploited to calibrate the strain sensitivity of each device within the 3D hybrid structure under a pure tensile strain field. The pure tensile strain field was applied by using a mechanical clamp device to apply tensile strain, where the strain was calculated from the length change of the cylindrical hybrid structure. A 10% tensile strain along the cylinder axis (Figure 3.6c) yielded decreases in conductance up to 200 nS for the individual devices, d1–d11. Because

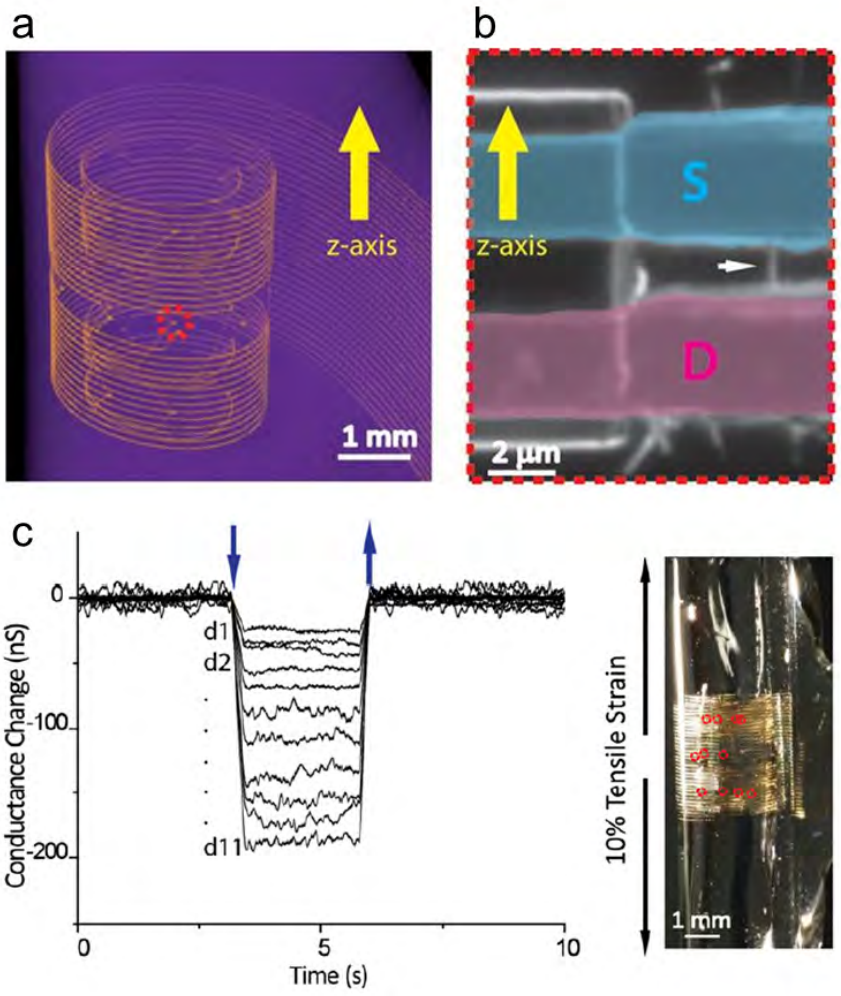

Figure 3.6: The 3D macroporous strain sensors embedded in elastomer. (a) Micro-CT 3D reconstruction of the macroporous strain sensor array embedded in a piece of elastomer. Pseudo-colors are applied: Orange, Metal; Purple, Elastomer. (b) Dark-field microscopy image of a typical NW device indicated by red dash circle in (a). All of the functional NWs are intentionally aligned parallel to the axial axis of the elastomer cylinder. The white arrow points to a NW. (c) Conductance change versus time as a 10% tensile strain was applied to hybrid 3D macroporous nanoelectronic networks/PDMS cylindrical sample. The downward and upward pointing arrows denote when the strain was applied and released, respectively. The direction of strain on the cylindrical hybrid sample and projected position of the macroporous nanoelectronic networks are indicated in the right optical micrograph. The conductance changes of 11 measured NW devices (labeled arbitrarily in terms of increasing sensitivity) were recorded and used for calibration.

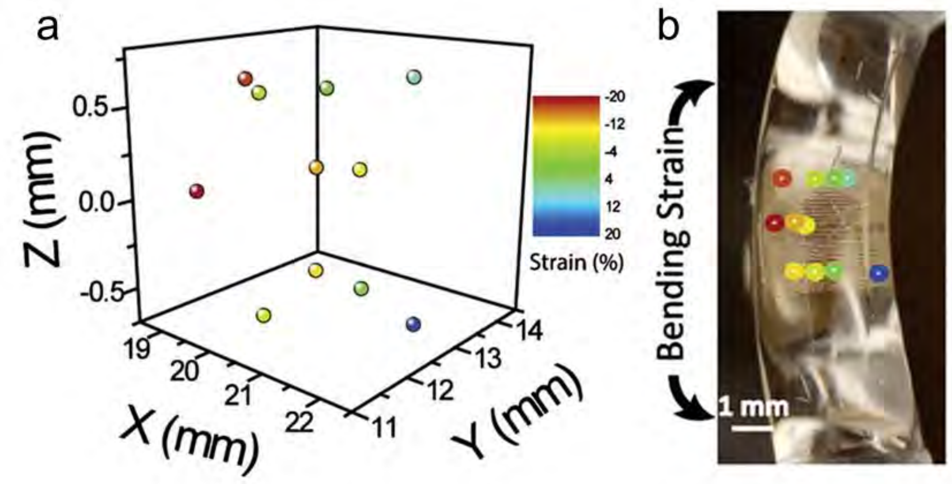

Figure 3.7: 3D mapping of a bending strain field in a macroporous nanoelectronic network/elastomer hybrid structure. (a) A bending strain field was applied to the elastomer piece. The 3D strain field was mapped by the NW strain sensors using the sensitivity calibration of the NW devices. (b) The positions of the devices used for detecting strain fields.

the conductance immediately returned to baseline when strain was released, and under compressive loads the conductance change had the opposite sign, we can conclude that these changes do reflect strain transferred to the NW sensors.

From the specific response of the devices within the hybrid structure we calculate and assign a calibrated conductance change/1% strain value for each of the 11 sensor elements shown in Figure 3.6, and use this calibration for 3D mapping of other arbitrary applied strains. For example, we applied a bending strain to the hybrid cylinder structure, and from the recorded conductance changes and calibration values were able to map readily the 3D strain field as shown in Figure 3.7. We note that the one-dimensional geometry of NWs gives these strain sensors nearly perfect directional selectivity, and thus, by developing a macroporous nanoelectronic network with NWs devices aligned parallel and perpendicular to the cylinder axis, enables mapping of all three components of the strain field in the future.

3.5 Conclusion and Prospective

We have demonstrated a general strategy for integrating 3D macroporous nanoelectronic networks with organic gels and polymers to form hybrid materials in which the basic physical and chemical properties of the host were not substantially altered, and electrical measurements further show >90% yield of active devices in the hybrid materials. We further demonstrated a unique approach to determine the positions of the NW devices within 3D hybrid materials with ∼14 nm resolution that involves simultaneous NW device photocurrent/confocal microscopy imaging measurements. This method also could have substantial impact on localizing device positions in macroporous nanoelectronic/biological samples, where it provides the capability of determining positions of sensory devices at the subcellular level. In addition, we explored functional properties of these hybrid materials. First, we showed that it was possible to map time-dependent pH changes throughout a NW network/agarose gel sample during external solution pH changes. These results suggest the substantial promise of 3D macroporous nanoelectronic networks for real-time mapping of diffusion of chemical and biological species through polymeric samples as well as biological materials such as synthetic tissue[62, 63]. Second, we demonstrated that Si NW elements can function as well-defined strain sensors, and thereby characterize the strain field in hybrid nanoelectronic elastomer structures subject to uniaxial and bending forces. More generally, we believe our approach to fabrication of multifunctional 3D electronics and integration with host materials suggests substantial promise for (1) general fabrication of truly 3D integrated circuits based on conventional fabrication processes via assembly from a 2D “precursor”, and (2) seamless 3D incorporation of multifunctional nanoelectronics into living and nonliving systems leading to the realization of “smart” material systems and “cyborg” tissues.

4

Long-term Stability of Nanowire Nanoelectronics in Physiological Environments

4.1 Introduction

NW nanoelectronic devices have been exploited as highly-sensitive detectors for biological systems at subcellular resolution. It has been used for recording extracellular and intracellular signals from cells, as well as natural and engineered tissues, and in this capacity open many opportunities for fundamental biological research and biomedical applications[10, 11, 33, 46, 56, 64–75]. For example, Si NW FETs have been used for real-time *in vitro* detection of disease markers proteins and even single virus particles[33, 46, 68–70], recording extracellular APs from cells and acute brain tissue slices with subcellular spatial resolution[71–74], recording intracellular APs from beating cardiac cells[10, 56, 75], and the development of electronically-innervated 3D cyborg tissues[11] Some of the directions being pursued with NW nanoelectronic devices, such as *in vitro* sensing, do not require long-term stability and biocompatibility, yet applications focused on chronic *in vitro* cell recording, implantable cyborg tissues, and more general implantable devices do require long-term NW stability in physiological environments.

In the previous chapters, I have demonstrated the advantage of NW nanoelectronics for building 3D macroporous nanoelectronic networks as well as "smart" materials. Before applying 3D macroporous nanoelectronic networks into biological applications, I would like to introduce our investigation on NW stablity in physiological environments in this chapter. We demonstrate a general approach to enhance the stability of NW nanoelectronic devices for long-term physiological studies by passivating the NW elements with ultrathin metal oxide shells. Studies of Si and Si/Al_2O_3 core/shell NWs in physiological solutions at 37 °C demonstrate long term stability extending for at least 100 days in samples coated with 10 nm thick Al_2O_3 shells. In addition, investigations of NWs FETs demonstrate that the Si/Al_2O_3 core/shell NW FETs exhibit good device performance for at least 4 months in physiological model solutions at 37 °C. The generality of this approach was also tested with in studies of Ge/Si and InAs NWs, where Ge/Si/Al_2O_3 and InAs/Al_2O_3 core/shell materials exhibited stability for at least 100 days in physiological model solutions at 37 °C.

In addition, investigations of HfO_2/Al_2O_3 nanolaminated shells indicate the potential to extend NW stability well-beyond 1 year time scale. These studies demonstrate that straightforward core/shell NW nanoelectronic devices can exhibit the long-term stability needed for a range of chronic *in vivo* studies in animals as well as powerful biomedical implants and pave the path for using NW nanoelectronics in biomedical applications.

4.2 Long-term Stability of Silicon Nanowires in Physiological Environments

Previous studies of cultured neurons with Si NW devices[11, 71] and silica nanopillars have demonstrated functional stability on at least a 2–3 week time scale, although other work[76] has reported dissolution of nanoscale Si under physiological conditions on a shorter times. Taking Si NWs as a prototypical nanoelectronic system, it is interesting to consider possible degradation pathways as well as methods for stabilization. Si NWs and FETs will have a native SiO_2 surface passivation layer under standard fabrication conditions due to oxidation in air[77]. The SiO_2 layer is stable in the dry state, but can dissolve by hydrolysis in aqueous solutions[78] with a rate accelerated at higher ionic strengths typical of physiological environments[79]. Dissolution of Si structures can occur by a cycle in which the Si surface is re-oxidized and dissolved. The fact that previous studies have reported different stabilities[11, 71, 76] may reflect the complexity of inorganic nanostructure/cell interfaces where protein absorption[80] and/or lowered oxygen concentrations could substantially slow dissolution steps.

Given the hypothesis for Si NWs degration described above, it should be straightforward to enhance the stability of Si NWs in a rational manner by introducing a stable conformal shell material. To demonstrate this concept for improving the intrinsic long-term stability

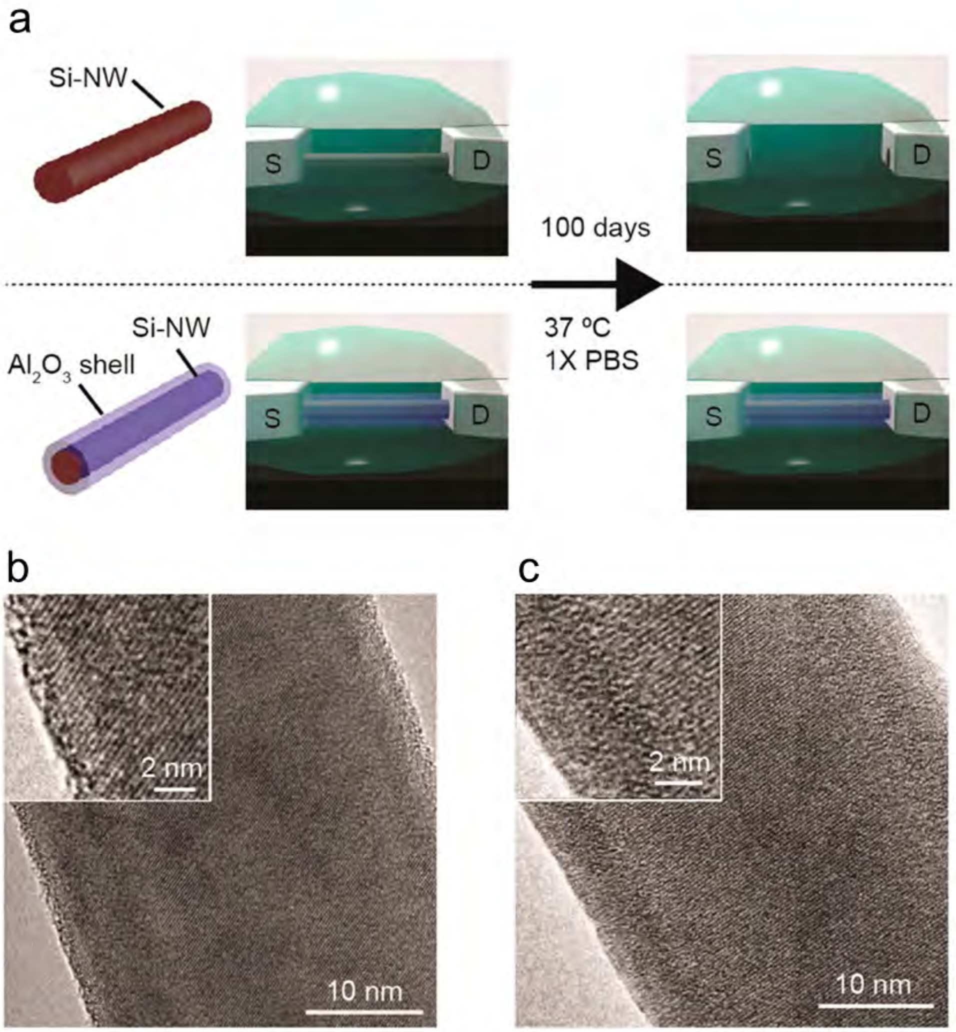

Figure 4.1: Core/shell heterostructures stabilize of Si NWs in physiological environments. (a) Schematic illustration of long-time evolution of Si NW FET devices with and without Al_2O_3 protective shell in physiological mimicking $1\times$ PBS (pH $= 7.4$) at 37 °C. (b) TEM image of a Si NW with native surface oxide. (c) TEM image of a Si NW with a 5 nm thick Al_2O_3 shell. The Al_2O_3 was annealed at 400 °C for 1 min prior to sample preparation.

of NW nanoelectronics in physiological environments, we adopted a core/shell architecture, where the shell is a metal-oxide such as Al_2O_3. Our overall experimental strategy (Figure 4.1a) involves direct comparison of the stability of Si and Si/Al_2O_3 core/shell NWs alone or configured as FET devices in biologically relevant solutions at 37 °C and room-temperature. Al_2O_3 was chosen as the NW shell material in the majority of our studies for several reasons. First, Al_2O_3 has excellent chemical stability in the physiological environments, and moreover, has been explored as a material for implanted dental and orthopedic applications[81, 82]. Second, the Al_2O_3 shells should not adversely affect the performance of NW FETs since Al_2O_3 is a high dielectric constant gate material[83]. Third, it is easy to achieve high-quality, pinhole free, conformal shells of Al_2O_3 on NWs with accurate control of thickness in the nanometer scale by ALD technique[84, 85].

The Si NWs (30 nm diameter) were grown by our previously reported gold nanoparticle catalyzed VLS method[22, 86]. Briefly, the growth substrate (600 nm SiO_2/Si) was cleaned by oxygen plasma (50 W, 1 min), treated with poly-L-lysine solution (0.1%, Ted Pella Inc.) for 5 min, and then rinsed thoroughly with DI water. For Si-NW synthesis, 30 nm gold nanoparticles were dispersed on growth substrates, and then NW growth was carried out at 450 °C under a constant pressure of 40 torr, with SiH_4 (2.5 s.c.c.m.), diluted B_2H_6 (100 ppm in He, 3 s.c.c.m.) and H_2 (60 s.c.c.m.) as reactant, doping and carrier gases, respectively. The growth time was 30 min, producing an average NW length of 25 μm. Si NWs on their respective growth substrates were placed in an ALD reactor (Savannah 200, Cambridge Nanotechnology Inc.), and Al_2O_3 shells were deposited using a standard protocol. Trimethylaluminum and H_2O were sequentially introduced into the ALD chamber with 0.015 s pulses with intervening 20 s N_2 purging (20 s.c.c.m.) with the substrate temperature of 150 °C and a background pressure of 0.2 torr. 50 cycles were used for the deposition of ca. 5 nm of Al_2O_3 and 100 cycles for the deposition of ca. 10 nm of Al_2O_3. Post-deposition rapid thermal annealing (RTA) at 400 °C for 1 min was used to improve the quality of Al_2O_3 layers[87].

A TEM image of a representative Si NW (Figure 4.1b) reveals a $\sim$0.5 nm thick amorphous layer on the surface, which can be attributed to the Si oxide[77] and a crystalline Si structure for the NW core. In contrast, a TEM image of a Si/Al_2O_3 core/shell NW (Figure 4.1c) shows a uniform 5–6 nm thick amorphous Al_2O_3 shell on a crystalline Si NW core. The thickness of the shell is consistent with that expected for the 50 ALD cycles used for deposition, and moreover, the amorphous structure after 400 °C/1 min RTA is consistent with previous studies showing that $>$650 °C temperatures are required to initiate the crystallization of amorphous Al_2O_3[88].

We initially investigated the stability of Si and Si/Al_2O_3 core/shell NW under different aqueous solution conditions using the method shown schematically in Figure 4.2a[89]. First of all, blank substrates (600 nm SiO_2/Si) were coated with a 15 nm thick ALD coated HfO_2 film (150 cycle, 150 °C substrate temperature, and 1 min post RTA at 550 °C) to prevent etching of the SiO_2 during studies. Si NWs with and without Al_2O_3 coatings were transferred to substrates by contact printing as described before[5]. Second, a $\sim$10 nm thick Cr film was deposited on NWs to prevent etching of Al_2O_3 shells by the basic developer (MicroChem MF CD 26) used during the photoresist patterning/developing process. A 4 mm pitch periodic Shipley 1805 photoresist stripes were patterned by photolithography, where regions of the photoresist crossing NWs will be protected from solution. The Cr metal in unprotected regions of the stripe design was removed with a Cr etchant (Cr etchant

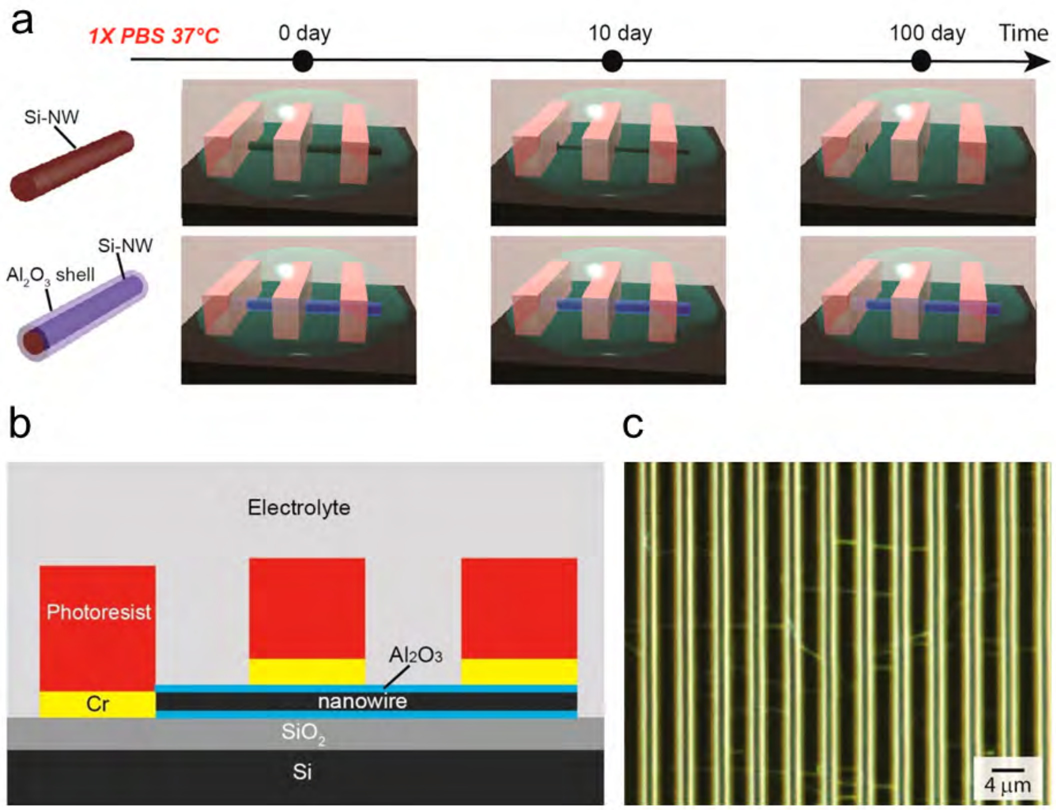

Figure 4.2: Experiment design for NW stability test. (a) Schematic illustrating the experiment methodology. (b) Cross-section schematic illustrating the patterned photoresist stripes (end-on) used in the experiments. (c) Top-view dark-field image of Si NWs covered by photoresist stripe patterns. The Si NWs are oriented in the horizontal direction and the photoresist stripes in the vertical direction in the image. The regions of the NWs not covered by photoresist were exposed to either $1\times$ PBS (pH $= 7.4$) or $1\times$ Neurobasal solutions (pH $= 7.3$) at either 37 °C or at a room temperature for fixed time periods. After removal of photoresist stripes (and underlying Cr) on the NWs and substrates, the dissolution of NW in the solution exposed regions can be sensitively assessed using dark-field optical microscopy by comparing contrast in the exposed and protected regions.

1020; Transene Company Inc.). (Figure 4.2b,c) Third, following treatment in physiological electrolytes (e.g., in 1× PBS at 37 °C, and in Neurobasal at 37 °C) for a specific time duration, the patterned photoresist was removed using Remover PG (MicroChem Corporation), and then the Cr layer was removed by Cr etchant. Last, NW/substrate samples can be characterized using dark-field microscopy.

Samples stability were firstly tested in either 1× PBS (pH $=$ 7.4) or 1× Neurobasal solutions[40] (pH $=$ 7.3) at either 37 °C in the incubator or at a room temperature for fixed time periods. Dark-field imaging of NWs provides a sensitive assessment of dissolution since the Rayleigh scattering intensity depends on NW diameter to sixth power (i.e., $I_{\text{scattering}} \propto d^6$ on the nanometer scale[90]. Dark-field images recorded from Si NW samples have 0, 5 and 10 nm Al_2O_3 shell thicknesses following immersion in in 1× PBS at 37 °C 10, 50 and 100 days (Figure 4.3a) show several key features. First, Si NWs without Al_2O_3 shells exhibited dissolution in the NW regions not protected by photoresist after 10 days, although the NW structures remain continuous. Second, Si NW samples exposed for 50 or 100 days showed complete dissolution of the Si in regions exposed to solution and not protected by photoresist. In contrast, the Si NWs with 5 and 10 nm thick Al_2O_3 shells, where all Al_2O_3 shells were annealed for 1 min at 400 °C , exhibited substantially greater stability in 1× PBS at 37 °C. For example, Si NWs with 5 nm shells remained showing little dissolution at 50 days, and NWs with 10 nm shells were similar at 100 days.

In addition, we have investigated stability of these different core/shell Si NWs at room temperature since many sensing and diagnostic applications NW FET detectors are carried out under ambient conditions. Dark-field images recorded from similar Si NW samples having 0, 5 and 10 nm Al_2O_3 shell following immersion in 1× PBS at room tempera-

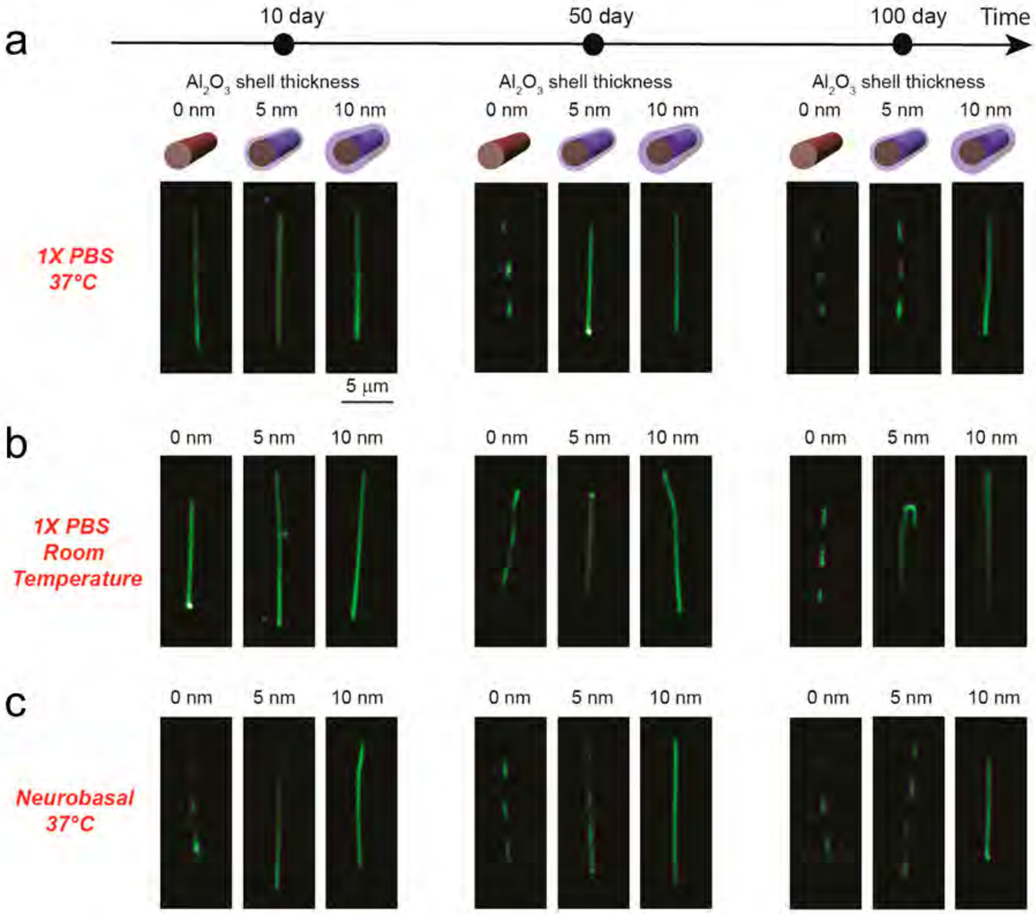

Figure 4.3: NW stability test in physiological electrolytes. (a-c) Dark-field microscope images showing morphology evolution of Si NWs with different Al_2O_3 shell thickness in $1\times$ PBS at 37 °C (a), $1\times$ PBS at room temperature (b), and Neurobasal at 37 °C (c).

ture (Figure 4.3b) showed substantially greater stability. For example, the Si NWs without Al_2O_3 shells do not show obvious signs of dissolution until ca. 40–50 days and are still continuous structures at this point. This corresponds to ~4–5 times slower rate and is consistent with expectations for an activated process (at lower temperatures). Moreover, the Si/Al_2O_3 core/shell NWs with 5 and 10 nm shell thicknesses did not show any obvious dissolution after even 100 days in solution.

We also carried out stability studies in 1× Neurobasal neuron cell culture media[40] as a closer analog (than PBS) to *in vivo* environments, where this medium contains amino acids and other organic components in addition to inorganic ions[40]. Dark-field images recorded at different times from NW samples having 0, 5 and 10 nm Al_2O_3 thick shell following immersion in this medium at 37 °C (Figure 4.3c) show similar behavior as 1× PBS at 37 °C. The comparable dissolution behavior for the two media is consistent with their similar ionic strength and pH values. Significantly, these studies show the Si/Al_2O_3 core/shell NWs with 10 nm thick shells remain stable for at least 100 days in both media at 37 °C.

4.3 Improvement of Silicon Nanowire Field-effect-transistors Stability in Physiological Environments by Al_2O_3 Surface Coating

To assess the long-term stability of NW bioelectronic sensor devices we fabricated FETs with Si and Si/Al_2O_3 core/shell NWs, and monitored the device characteristics when immersed in 1× PBS solutions at 37 °C for extended time periods. The S/D contacts on the NWs were fabricated using standard procedures and passivation with SU-8 photoresist[91]. Device conductance and transconductance versus time data recorded[92] for Si NWs (Fig-

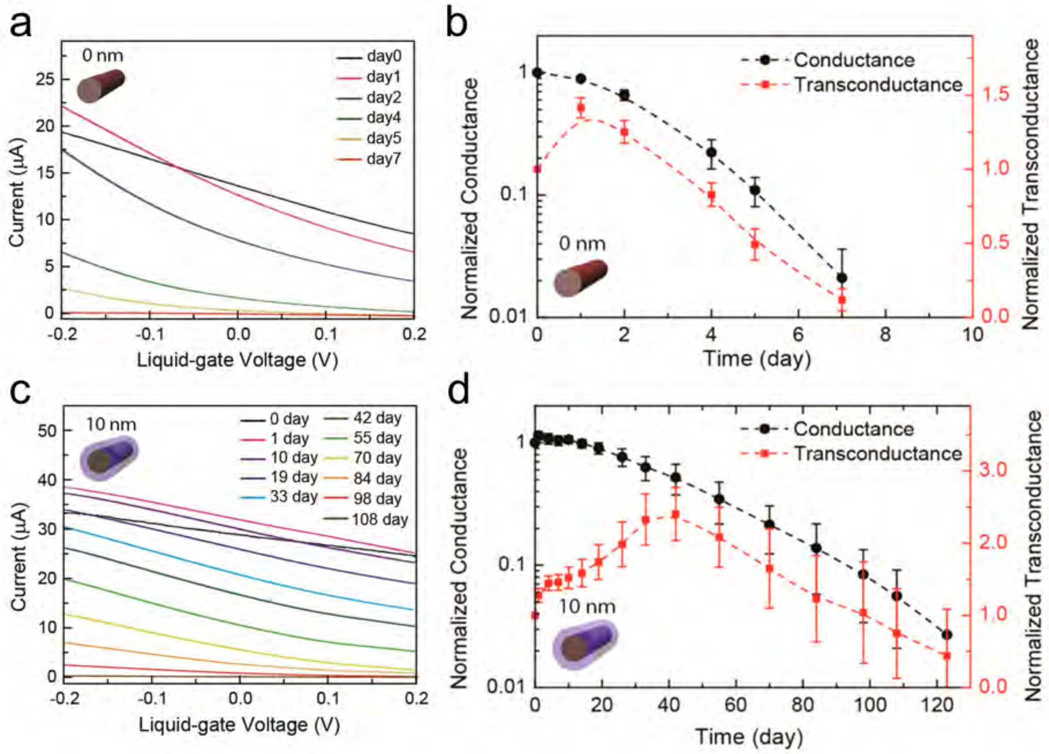

Figure 4.4: Si and Si/Al$_2$O$_3$ NW FETs stability in solution at 37 °C. (a) Time-dependent evolution of current versus solution-gate-voltage curves for a representative Si NW FET in $1\times$ PBS at 37 °C. (b) The normalized conductance and transconductance change for Si NW FETs in $1\times$ PBS at 37 °C. (c) Time-dependent evolution of current versus solution-gate-voltage curves for a representative Si/Al$_2$O$_3$ core/shell (10 nm thick shell) NW FET in $1\times$ PBS at 37 °C. (d) The normalized conductance and transconductance change for Si/Al$_2$O$_3$ core/shell (10 nm thick shell) NW FETs in $1\times$ PBS at 37 °C. The average results in (b) and (d) were determined at solution $V_{\mathrm{g}} = 0$ V from 30 devices.

ure 4.4a, b) revealed several key features. First, the normalized average ($N = 30$) conductance decreased to less than 3% of the initial value at day 7. The transconductance initially exhibited an increase at day 1 but then decreased as observed for the conductance. However, the decrease in transconductance was much slower than conductance and at day 7 was still 13% of the initial value. For this reason, it is possible to utilize the Si NW FETs until nearly the point of complete failure.

Similar measurements carried out for Si/Al_2O_3 core/shell NW (10 nm thick shell) FETs demonstrate long-term stability as expected based on our NW dissolution studies. Specifically, we found that the normalized average ($N = 30$) conductance of Si/Al_2O_3 NW FETs was constant for ca. 20 days, and then decreased slowly until ca. 3% of the initial value at day 120. In addition, the normalized average transconductance of the Si/Al_2O_3 NW increased over during the first 50 days, and then decreased to ca. 50% the initial value at day 120. These data demonstrate clearly that the Al_2O_3 shell can open chronic studies on a 4 month time-scale with functional NW nanoelectronic devices. Moreover, we believe that the observed changes in conductance and transconductance (Figure 4.4c, d) indicate that defects in the Al_2O_3 shells may play an important role in the device changes, and hence that efforts focus on improving the shell quality could further improve the NW stability.

Indeed, in a preliminary studies of using HfO_2/Al_2O_3 nanolaminated shells, we observed even dramatically enhanced stability revealed from an accelerated tests in 10× PBS. which can be projected to cooresponding chemical stablity in the normal 1× PBS for over 600 days at 37 °C.

4.4 Improvement of Different Types of Nanowires Stability in Physiological Environments by Al_2O_3 Surface Coating

Last, we have explored the generality of Al_2O_3 shells to stabilize NWs by exploring Ge/Si core/shell[31, 93, 94] and InAs NWs[95, 96], which have been shown to exhibit higher hole and electron mobilities, respectively, than Si NWs. The Ge/Si core-shell NWs were grown by a nanocluster-catalyzed VLS growth method. Briefly, 30 nm diameter gold nanoparticles were dispersed on the growth substrate, and then the germanium-core NW was grown at 270 °C and 450 torr, with GeH_4 (30 s.c.c.m., 10% in H_2) and H_2 (200 s.c.c.m.) as the reactant and carrier gases, respectively, for 50 min (average length = 30 μm), and the the epitaxial Si shell was grown at 460 °C and 5 torr for 2 min using SiH_4 (5 s.c.c.m.). The InAs NWs were prepared in a two-zone furnace. In a typical growth, a few grams of InAs (99.9999%, Alfa Aesar) were loaded into a quartz transfer tubes located at the upstream end of the reactor, while the growth substrate (600 nm SiO_2/Si) with well dispersed 50 nm gold nanoparticles was placed downstream in zone II of the tube furnace. The reactor was then evacuated to 15 mtorr, and after zone I and zone II had reached set temperatures of 690 °C and 530 °C, respectively, the transfer tube with InAs powder was inserted into the center of zone I to initiate the growth. A total pressure of 2 torr was maintained during the growth process, with a 20 s.c.c.m. flow of H_2 and the growth time was 30 min.

Dark-field images recorded from Ge/Si and Ge/Si/Al_2O_3 NWs (Figure 4.5a) as well as InAs and InAs/Al_2O_3 NWs (Figure 4.5b) following immersion in 1× PBS at 37 °C for 10, 50 and 100 days show similar features to Si NWs described above. The Ge/Si and InAs NWs exhibited relatively rapid dissolution with areas exposed to solution completed removed within 10 days at 37 °C. In contrast, our data show that the Al_2O_3 shells

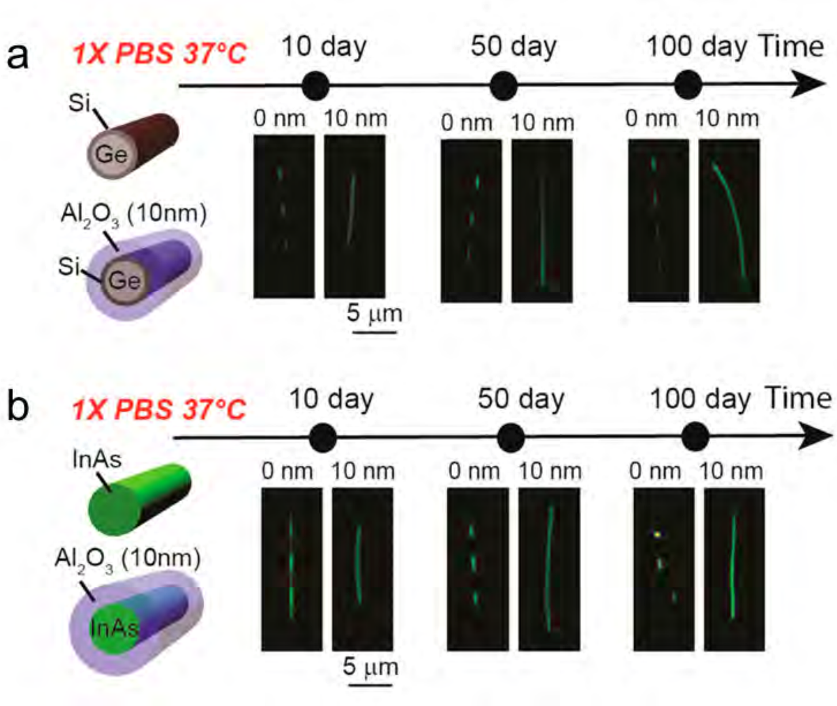

Figure 4.5: Improved stability of other semiconductor NWs with Al_2O_3 shells. (a-b) Dark-field microscope images showing time-dependent evolution of Ge/Si core/shell NWs (a) and InAs/Al_2O_3 core/shell NWs in $1\times$ PBS at 37 °C (b).

improve substantially the long-term stability to over 100 days for both Ge/Si and InAs NWs. Therefore, by using this oxide shell strategy it is possible to extend the use of non-Si nanoelectronic devices to chronic biomedical applications in physiological conditions.

4.5 Conclusion and Prospective

In conclusion, we have demonstrated the capability to take full advantage of the attractive capabilities of NW nanoelectronic devices for long-term physiological studies by passivating the NW elements with ultrathin metal oxide shells. Studies of Si and Si/ Al_2O_3 core/shell NWs in physiological solutions at 37 °C show long term stability extending for at least 100 days in samples coated with 10 nm thick Al_2O_3 shells. In addition, investigations of NWs configured as FETs demonstrate that the Si/Al_2O_3 core/shell NW FETs exhibit good device performance for at least 4-months in physiological model solutions at 37 °C. The generality of this approach was also tested with in studies of Ge/Si and InAs NWs, where Ge/Si/Al_2O_3 and InAs/Al_2O_3 core/shell materials exhibited stability for at least 100 days in physiological model solutions at 37 °C. In addition, investigations of HfO_2/Al_2O_3 nanolaminate shells indicate the potential to extend NW stability well beyond 1 year time scale. These studies demonstrate that straight forward core/shell NW nanoelectronic devices can exhibit the long-term stability needed for a range of chronic *in vivo* studies in animals as well as powerful biomedical implants that could improve monitoring and treatment of disease.

5

Three-dimensional Macroporous Nanoelectronic Scaffolds for Building "Cyborg" Tissues

5.1 Introduction

The development of engineered 3D tissues of electrogentic cells such as neurons[97–99], cardiomyocytes[100–103] and other cells[104] has attracted substantial attention due to their potentials in both *in vitro* biomedical models[104–110] and *in vivo* implantation for regenerative medical treatment[111, 112]. Since the quality and the functionality of engineered 3D electrogentic tissues are fundamentally relevant to the microscopic electrophysiology behaviors in the cellular network, it is crucial to find an effective way to achieve large-scale 3D real-time mapping of APs conduction in engineered 3D tissues[111–115]. However, real-time optical mapping approaches[116–120] using voltage-sensitive dyes for visualizing APs, are limited by a relatively slow time-resolution to scan a 3D region because it takes at least 0.1–10 s to scan each plane while maintaining a high in-plane spatial resolution either by confocal microscopy[120, 121] or by selective plane illumination microscopy[122]. Besides, the imaging depth in optical microscopy is restricted by strong light scattering in the tissues. On the other hand, conventional multiplex electrical recording techniques by planar microelectrode arrays[6, 9, 110, 123–125] and FET arrays[11, 43, 72, 73, 126, 127] have the intrinsic advantage for fast mapping of APs with a sub-millisecond temporal resolution, but they are limited to resolve APs signals in 2D cultured cells or on the surface of the 3D tissues. To achieve APs recordings deep into 3D tissues with high spatial and temporal resolution, conceptually new methods are required.

The 3D macroporous nanoelectronic networks[11, 128], as we described in previous chapters, can mimic the synthetic or natural extracellular matrix in terms of (1) microscale-to-nanoscale feature size compatible with cellular or subcellular structures, (2) high porosity good for complete cell interpenetration and growth in the scaffolds, (3) tunable mechanical properties required optimized for tissue growth, and (4) inert biochemical properties for long physiological study[113, 129, 130]. By using 3D macroporous nanoelectronic networks as tissue scaffolds and growing tissue on them, active electronic components can be seamlessly and non-invasively integrated into 3D engineered tissues. The development of electronics-innervated tissues — "cyborg" tissues — has led to new opportunities for large-scale 3D mapping of electrical activities by co-culturing the nanoelectronic sensors with the tissues. However, previously demonstrated cyborg cardiac tissue still has several limitations. First, size of S/D electrodes of FET as potentiometric sensors is over 100 μm, thus doesn't enable subcellular spatial detection. Second, the mismatch of mechanical properties between scaffolds and tissues leads to a non-optimal device/cell affinity and a low recording yield of 4 channels out of 60 FET sensors, not sufficient for a large-scale 3D mapping of APs.

As significant achievements, we (1) successfully designed and fabricated over a hundred Si NW based FET sensors with size 1–10 μm for subcellular scale detection; (2) maintained 50 kHz sampling rate in simultaneous multiplexed recording to achieve sub-millisecond temporal resolution; (3) improved device/cell junction affinity and thus reached ∼100% successful measurement from all recordable devices; and (4) further demonstrated multi-function. The cyborg cardiac tissues enabled by multifunctional macroporous nanoelectronic scaffolds were used in the applications including real-time monitoring of tissue development process; spatiotemporal visualization of electrophysiology activities modulated by drugs and electrical stimulation.

5.2 Fabrication of "Cyborg" Cardiac Tissues

The nanoelectronic tissue scaffolds were synthesized via a three steps strategy. First of all, an on-substrate mesh-like nanoelectronic networks containing 2D arrays of 64 to 256 nanoelectronic devices were fabricated through conventional photolithography patterning, which was then released into a free-standing form by lift-off process[128]. (Figure 5.1a)

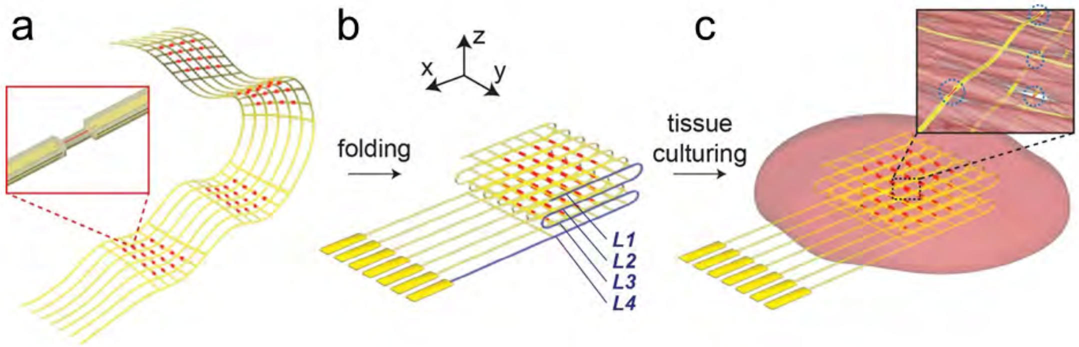

Figure 5.1: Schematics of fabricating macroporous nanoelectronic scaffolds and cyborg cardiac tissue. (a–c) Schematic illustrations of nanoelectronic scaffold fabrication and culture of cyborg cardiac tissue. (a) Free-standing macroporous nanoelectronic scaffold with NW FET arrays (red dots); inset, one NW FET. (b) Folded free-standing scaffolds with four layers, *L1*–*L4*, each containing addressable FET arrays, and overall forming a 3D sensor array. (c) Schematic highlighting primary culture of cardiac cells within the scaffold to form cyborg cardiac tissues, where all the nanoelectronic sensors (blue circles, inset) innervate the 3D cell network.

Second, the free-standing nanoelectronic networks were folded to form 3D nanoelectronic scaffolds with a desirable 3D distribution of device arrays (Figure 5.1b) Third, primary culture of neonatal rat ventricle cells was conducted on the 3D nanoelectronic scaffolds (Figure 5.1c). Here, we adopted Si NW FET arrays as potentiometric sensors and designed z= 4 regions with x × y = (4 × 4) devices in each region to form a (4 × 4 × 4) distributed 3D devices arrays after triple folding (Figure 5.1b), as an example for illustration.

The Si NWs were grown by a gold nanoparticle-catalyzed VLS growth method. Briefly, the growth substrate (600 nm SiO_2/Si) was cleaned by oxygen plasma (100 W, 3 min), treated with poly-L-lysine solution for 5 min, and then rinsed thoroughly with DI water. 30 nm gold nanoparticles were dispersed on growth substrates for 2 min and then then rinsed thoroughly with DI water to coat catalysts. Then NW growth was carried out at 450

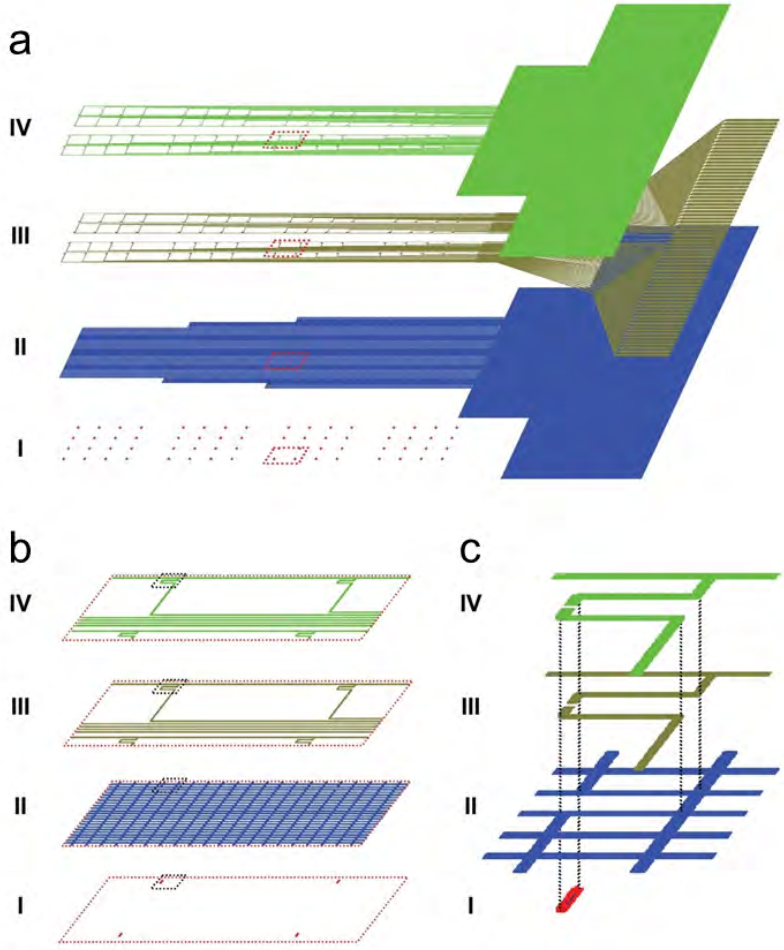

Figure 5.2: Nanoelectronic mesh fabrication layouts. Schematics with increasing magnification (a–c) of four basic layers (I–IV) in the nanoelectronic mesh scaffolds. The four layers (bottom to top) are (I) NW assembly patterning layer consisting of an array of SU-8 rectangular pads (red), (II) bottom SU-8 mesh structure/passivation layer (blue), (III) metal S/D contact and interconnect layer (gold), and (IV) top SU-8 passivation layer (green). (a) Overall mesh structure, including I/O at right of schematic. (b) Zoom-in structure of the four layers within a 1.8×2.0 mm^2 area (red dashed boxes in (a) containing a 2×2 device array. (c) Zoom-in structure of the four layers around one individual NW device (black dashed boxes in b). (a–c) Top SU-8 passivation layer shown in green is 350 nm in thickness and 4 μm in line width. Metal S/D contacts and interconnects (Cr/Pd/Cr with thickness of $1.5/50/1.5$ nm) shown in yellow with 2 μm line width. Bottom SU-8 supporting layer shown in blue is 350 nm in thickness and 4 μm in line width. NW assembly patterning layer is periodic array of rectangular SU-8 pads with 350 nm in thickness, 4 μm width and 20 μm length.

°C under a constant pressure of 30 torr with SiH_4 (2 s.c.c.m.), diluted B_2H_6 (100 ppm in He, 2.5 s.c.c.m.), and Ar (10 s.c.c.m.) as reactant, doping, and carrier gases, respectively. The Si:boron feed-in ratio was 4000:1 and the growth time was 30 min to produce an average NW length of 30 μm.

The free-standing macroporous mesh-like nanoelectronic scaffolds containing $(4\times4\times4)$ Si NW FETs were fabricated on the oxide surface of Si substrates (600 nm SiO_2, n-type 0.005 V cm, Nova Electronic Materials) before relief from the substrate. Key steps (Figure 5.2) used in the fabrication of the free-standing mesh-like nanoelectronic scaffolds were as follows:

(1) Lithography defined Ni metal film (100 nm thick) was deposited by thermal evaporation on the oxide surface of Si substrate (600 nm SiO_2), serving as the final relief layer for the free free-standing mesh-like nanoelectronic scaffolds. (2) A 300 nm layer of SU-8 photoresist (2000.5) was spin coated over the entire substrate, followed by prebaking at 65 °C and 95 °C for 1 and 3 min, respectively. Photolithography was then used to define the SU-8 layer into UV exposed region of rectangular pad arrays. After post-baking (65 °C and 95 °C for 1 and 3 min, respectively), the surface of SU-8 layer was made to be hydrophilic by oxygen plasma treatment (30 W, 20 s). (3) The substrate was then mounted onto a movable stage controlled by a micromanipulator. Approximately 40 μL oil (heavy mineral oil; Sigma-Aldrich Corporation) was drop-cast onto the target substrate as the lubricant. The Si NW growth substrate (1.2×1.2 cm^2) was then brought into contact with the target substrate with a constant pressure of 4.8 N cm^{-2}. During contact printing of Si NWs[39, 40], the target substrate was moved by the micromanipulator at a constant velocity of 5 mm/min with respect to the fixed growth substrate. After being rinsed by hexane

to remove the mineral oil, the SU-8 substrate with well-aligned Si NWs was put into SU-8 developer for 1 min and sonicated for 10 s to develop the SU-8 layer. Since the NWs on the non-UV-exposed SU-8 region will be removed from the substrate during the development, NW arrays were selectively transferred on UV-exposed SU-8 pad arrays predefined by the photolithography. The developed SU-8 patterns with NWs on the surface were cured at 180 °C for 20 min. (This procedure can minimize the effect of the scratching on the SU-8 layer during contact printing process.) (Figure 5.2a–c, I) (4) A 300 nm layer of SU-8 photoresist was spin-coated over the entire chip followed by prebaking at 65 °C and 95 °C for 1 and 3 min, respectively. Then photolithography was used to pattern the bottom SU-8 layer into mesh-like structures connecting SU-8 pad arrays with NWs, which serve for passivating and supporting the later fabricated NW nanoelectronic device networks. The structure was postbaked, developed, and cured by the same procedure described in step (2). (Figure 5.2a–c, II) (5) Photolithography and thermal evaporation were used to define and deposit the metal S/D contacts to create arrays of Si NW FET sensors on the SU-8 mesh structures. Symmetrical Cr/Pd/Cr (1.5/50–80/1.5 nm) metal was sequentially deposited followed by liftoff process in Remover PG (MicroChem Corporation). (Figure 5.2a–c, III) (6) A 300 nm layer of SU-8 photoresist was deposited over the entire chip, followed by prebaking at 65 °C and 95 °C for 1 and 3 min, respectively. Then photolithography was used to pattern the top SU-8 layer for passivating the whole device structure. The structure was postbaked, developed, and cured by the same procedure as described above. (Figure 5.2a–c, IV)

After the removal of the underlying sacrificial Ni layer, a free-standing mesh can be obtained. An optical image of the free-standing network floating in DI water (Figure 5.3)

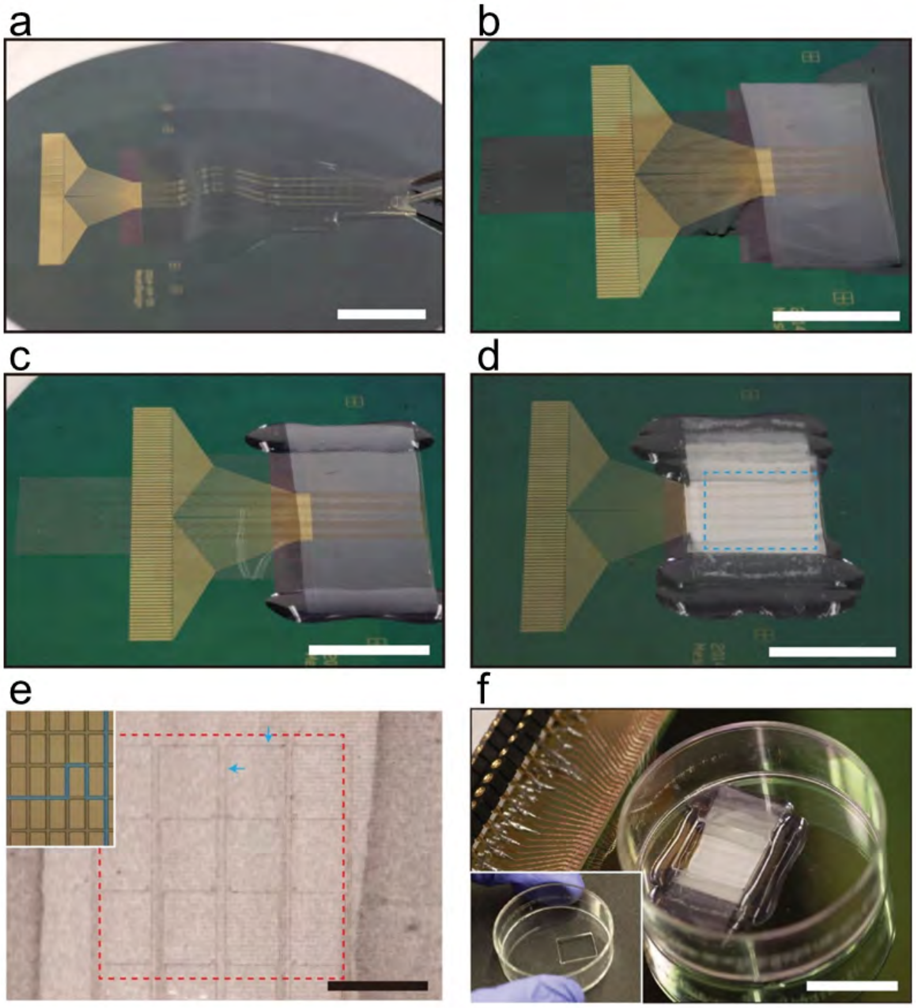

Figure 5.3: Folding process to form 3D nanoelectronic scaffolds. (a) Photograph of a free-standing nanoelectronic mesh suspended in the DI water. (b) Photograph showing folding step of two layers of the nanoelectronic mesh layers and a $25\ \mu\mathrm{m}$ thick PLGA electro-spun fiber film (white). (c) Photograph showing upper and lower edges of the folded nanoelectronic mesh layers were glued. (d) Photograph showing nanoelectronic mesh folded three times (four mesh layers). (e) Zoomed-in image of blue dashed-box in (d) showing the nanoelectronic scaffold lying on the electro-spun PLGA fiber film. Gray vertical/horizontal lines (highlighted by blue arrows) correspond to the SU-8/metal/SU-8 mesh elements. Inset: Bright-field optical microscopy image of $\sim 100 \times 120\ \mu\mathrm{m}^2$ region shows the SU-8 ribbon with metal (false-colored in blue) and without metal lines. (f) Photograph of modified petri dish with $\sim 10 \times 10$ mm^2 opening mounted on the scaffold substrate. Inset: Modified petri dish with opening in the bottom. (a–f) Scale bar, 1 cm.

shows its flexibility that enables further manipulation to fold it into 3D structures.

The free-standing macroporous mesh-like nanoelectronic scaffolds were then released from the substrate by dissolving the Ni layer in Nickel Etchant TFB for 60–120 min at 25 °C. The mesh-like nanoelectronic scaffolds were rinsed and soaked into a mixture of DI water and ethanol with desirable surface tension (Figure 5.3a). The free-standing nanoelectronic networks were folded by manual manipulation. With tweezers, the protruding end free-standing scaffold was manually flipped to the opposite side. Two device regions were carefully aligned and then overlaid under optical microscope (Figure 5.3b). After gently removing the DI water by pipet, the mesh structures were temporarily folded and stacked together with a good preserved alignment. In order to permanently immobilize the mesh scaffold with desired alignment during later 3D tissue culture process, we used silicone elastomer adhersive to fix the boundary of overlaid mesh layers. (Figure 5.3c) Then DI water was added to float the rest parts of scaffold and the previous steps were conducted repeatedly to fold the mesh scaffolds into multiple layers (Figure 5.4d,e). Ultimately, multiple layers of nanoelectronic scaffolds consisting of a 3D matrix of nanoelectronic devices were fixed and mounted with a self-modified polystyrene petri-dish (VWR Inc.) for the following cyborg cardiac tissue culture (Figure 5.3f). In order to control the separation distance between different mesh layers after folding, a specific thickness of Poly(lactic-co-glycolic acid) (PLGA) electrospun fiber film can be placed in between scaffold mesh structures during each folding steps. PLGA electro-spun fibers, which is a commonly used tissue scaffold for cardiac tissue engineering[96, 113, 114, 131], were electro-spun into thin films and characterized. Thickness of ∼25 µm and an averaged fiber diameter of 1 µm were chosen and used to be placed between each layer of mesh networks to space the devices in each layer with specific distance in vertical z direction.

The device was sterilized by UV-light illumination for 0.5 h and soaking in 70% ethanol solution for 0.5 h, followed by oxygen plasma (50 W, 1 min) treatment. Then the cyborg cardiac tissue scaffolds were thoroughly immersed in fibronectin/gelatin solution for 2 h before cell plating for surface modification. The fibronectin/gelatin surface coating solution was made by 0.5% fibronectin (Sigma-Aldrich Corporation) and 0.02% gelatin (Fisher Scientific). Primary neonatal rat cardiomyocytes were prepared according to previously published procedures[11, 72]. Briefly, intact ventricles were isolated from 1–3 day old Sprague/Dawley rats and were then digested at 37 °C in Hanks' balanced salt solution (HBSS) containing collagenase (class II, Worthington Biochemical). Isolated cells were suspended in the culture medium comprising 5% fetal bovine serum (FBS) and 95% Medium 199, supplemented with 0.12 mmol/L $CuSO_4$, 0.1 mmol/L $ZnSO_4$ and 1.5 mmol/L VB_{12}, 500 U ml^{-1} penicillin and 100 mg ml^{-1} streptomycin. The cell suspension was pre-plated in a flask for 2 h to reduce the percentage of non-cardiomyocyte cells. Then the collected supernant was concentrated and plated at a cell density of $3–6 \times 10^7/cm^2$. Cyborg cardiac tissues were incubated at 37 °C in a humidified atmosphere with 5% CO_2, with medium changed every other day.

Cyborg cardiac tissue was immunostained for confocal imaging. Firstly, cyborg cardiac tissue was fixed with 4% paraformaldehyde (Electron Microscope Sciences) in 1× PBS for 30 min, followed by 3 times washes with ice-cold 1× PBS. Second, tissue was permeabilized with 0.25% Triton X-100 in 1× PBS for 1 h at room temperature, followed by 3 times washes with ice-cold 1× PBS. Tissue was pre-blocked with 1% bovine serum albumin in 1× PBS for 1 h at room temperature. Third, tissue was incubated with primary antibodies in BlockAid solution (Molecular Probes, Invitrogen) for 1 h at room temperature, followed by 3 times washes with ice-cold 1× PBS. Last, tissue was incubated with the secondary antibodies with fluorophores, followed by 3 times washes with ice-cold 1× PBS in dark. For counter staining of cell nuclei, cells were incubated with 0.2 μg/mL DAPI for 1 min and then rinsed with 1× PBS in dark. Anti-sarcomeric α-actinin mouse monoclonal antibody (1:250; Clone EA-53, Sigma-Aldrich Corporation) was used to label sarcomere in cyborg cardiac tissue. And AlexaFluor-488 goat anti-mouse (1:400; Molecular Probes, Invitrogen) were used as the secondary antibodies. In parallel, the macroporous nanoelectronic scaffolds, SU-8, which was used to form the backbones, was pre-doped with 1 μg/mL rhodamine-6G during photolithography for confocal imaging.

Confocal imaging was carried out using an Olympus Fluoview FV1000 confocal laser scanning microscope. Confocal images were acquired using 405, 473 and 559 nm wavelength lasers to excite cellular components labeled with DAPI, AlexaFluor-488 and rodamine-6G fluorescent dyes, respectively. ImageJ was used for 3D reconstruction and analysis of the confocal images. Bright-field optical images and videos were taken on an Olympus FSX100 system using Andor SOLIS X-4238 software. Footage was generated using ImageJ and Adobe Photoshop CS6 (Adobe Systems Inc.). The seamlessly integrated nanoeletronics and engineered cardiac tissue were simultaneously visualized from 3D reconstructed confocal microscopy image (Figure 5.4a). In the higher magnification confocal images (Figure 5.4b,c), the cardiomyocytes can be seen to be well-aligned along the scaffold ribbons, which demonstrates the affiliative interface between the nanoelectronic scaffolds and cells. Besides, the sarcomere length of 2.1 ± 0.1 μm (Figure 5.4c) depicts healthy cardiac tissue synthesized on the nanoelectronic scaffolds[132].

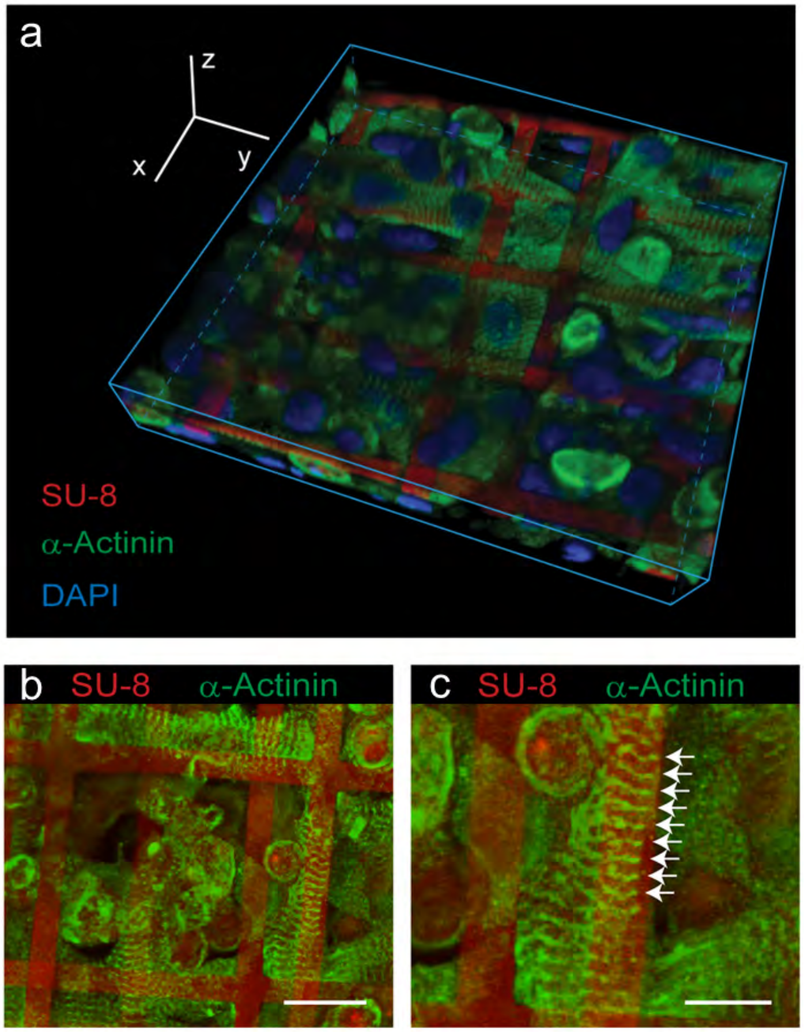

Figure 5.4: Confocal laser scanning microscopy characterization of cyborg cardiac tissue. (a) Confocal laser scanning microscopy 3D reconstruction image of cyborg cadiac tissue consists of interwoven cell networks/nanoelectronic scaffolds. Scale bar, 25 μm. (b) A zoom-in confocal laser scanning microscopy image of $100 \times 100\ \mu m^2$ area. Cardiomyocytes grown on the nanoelectronic scaffold shows clear alignment along the SU-8 ribbons, which is revealed by the sarcomere chain arrangement. Scale bar, 20 μm. (c) A high magnification confocal laser scanning microscopy image shows a characteristic sarcomere length of $2.1 \pm 0.1\ \mu m$. Scale bar, 10 μm. Electronic scaffold backbones are labeled in red by rhodamine-6G. Sarcomeric α-actinin and nucleus of cardiomyocytes are stained in green and blue, respectively.

The electrical transport performance of the FET sensors was assessed and demonstrated virtually free of failure and revealed noise level below 0.3 mV undergoing the tissue culture, which demonstrates the good robustness and the high sensitivity of the nanoelectronic scaffolds. All studies were carried out at 37 °C by precisely controlled using temperature controller (Warner Instruments Corporation) and in Tyrode solution (Sigma-Aldrich Corporation). A Ag/AgCl wire was used as a reference electrode. The conductance of Si NW FET was measured with DC bias set to 100 mV using a battery source. The drain current was amplified with a variable-gain amplifier (1211 current preamplifier; DL Instruments, Inc.) and the output data were recorded at an acquisition rate of 20–100 kHz by using a 16-channel A/D converter (Digidata 1440A) interfaced with a PC running pClamp electrophysiology software. Postanalysis was completed in OriginPro and Matlab (ver. R2011a, Mathworks).

We used the internally distributed FET in the cyborg cardiac tissue for spatiotemporal mapping experiment to investigate the 3D conduction behavior of cardiac APs. For one nanoelectronic scaffold consisted of $4 \times 4 \times 4$ FET arrays, 64 devices have independent I/O interconnections and thus can be recorded simultaneously. The yield of successful extracellular cardiac APs recording from FET arrays achieves $\sim$100% for more than 12 samples. Figure 5.5a shows one representative measurement of multiplexed cardiac AP recording from 16 FET sensors selected from layer 1 (top layer) of nanoelectronic scaffold. The recorded extracellular cardiac AP depicts a beating rate of $\sim$1.8 Hz, amplitude of 1–5 mV and peak width of $\sim$1 ms, which are consistent with typical results in previous works[72]. The high signal-to-noise ratio (up to 20), together with recording yield ($\sim$100%

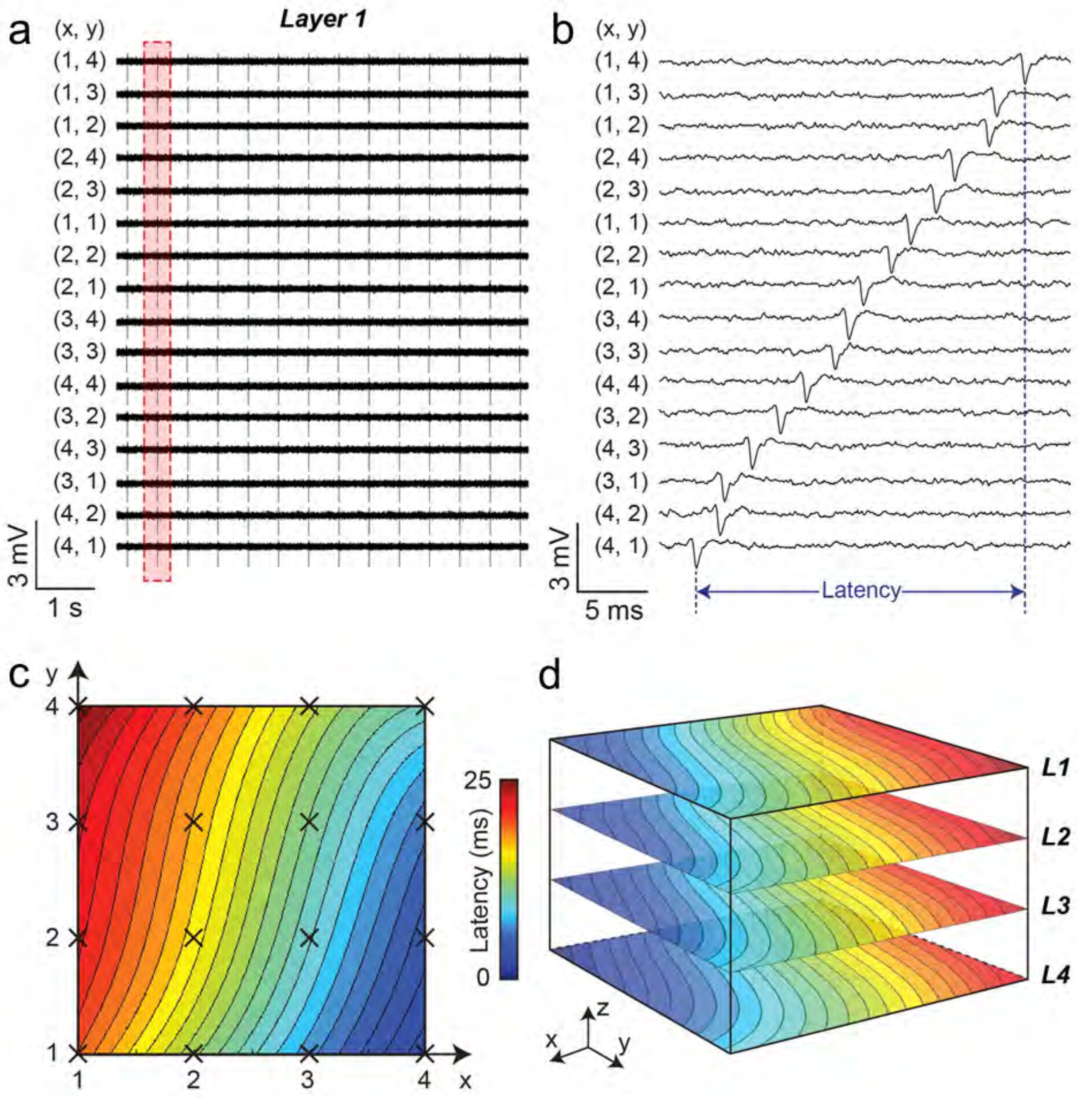

Figure 5.5: **3D spatiotemporal mapping of APs.** (a) Simultaneous traces recorded from 16 sensors in the top layer (*L1*) from cyborg cardiac tissue. The (x, y) coordinates of each element from the 4×4 array are shown. (b) Zoom of single AP recorded from each device in at the time indicated by the dashed box in (a). The time latency between APs recorded from different (x, y) devices is evident and indicated for $(4,\ 1)$ versus $(1,\ 4)$ sensors. (c) Isochronal map of time latency in *L1*; mapping area is ~ 25 mm^2. (d) 3D isochronal map of time latency through the sample, where *L1*–*L4* correspond to the four layers of 4×4 device array innervating the cardiac tissue. Mapping area is $\sim 5 \times 5 \times 0.2\ \mu\mathrm{m}^3$.

for >12 samples) and confocal microscopy image (Figure 5.4) confirms a favorable and robust nanoelectronic scaffold/cell interface and tissue healthiness.

The temporal resolution for the cardiac AP measurement is 0.02 ms corresponding to the data acquisition rate at 50 kHz. Thus, sub-millisecond time latency between APs collected from different channels can be easily observed from simultaneously multiplexed recording (Figure 5.5b). The APs in the cardiac tissue conduct from the pace-maker foci and spread over the whole tissue, therefore each FET sensor records the spikes when the AP wave front reaches the position of device. As a result, FET sensors at different locations record the AP at different time.

To better visualize the AP conduction behavior in cyborg cardiac tissue, we correlate the time latencies and the coordinates of each sensor, from which an isochronal map can be easily drawn (Figure 5.5c). The observed conduction pattern of AP wave shows an irregular anisotropic shape, which is likely due to the anisotropic cell alignment in the 3D cyborg cardiac tissue. In addition, the averaged diagonal conduction velocity is calculated about 28 ± 2 cm/s, which is very similar with that of *in vivo* neonatal rat heart tissue, 21–27 cm/s[110, 132, 133], and 40–130% higher than 2D cell culture samples, 12–19 cm/s. Our measured conduction velocity and 3D confocal images (Figure 5.4) confirm the 3D network connections in the cultured cardiac tissues integrated with nanoelectronic scaffolds and distinct behavior compared to 2D cultures. Combining the spatiotemporal measurement from all the FET sensors, AP conduction pattern in 4 layers at different depth can be visualized at the same time (Figure 5.5d). This 3D isochronal map can display the AP conduction behavior not only on the surface of cardiac tissues but also their interiors, which cannot be achieved by any other reported methods with a sub-millisecond time resolution.

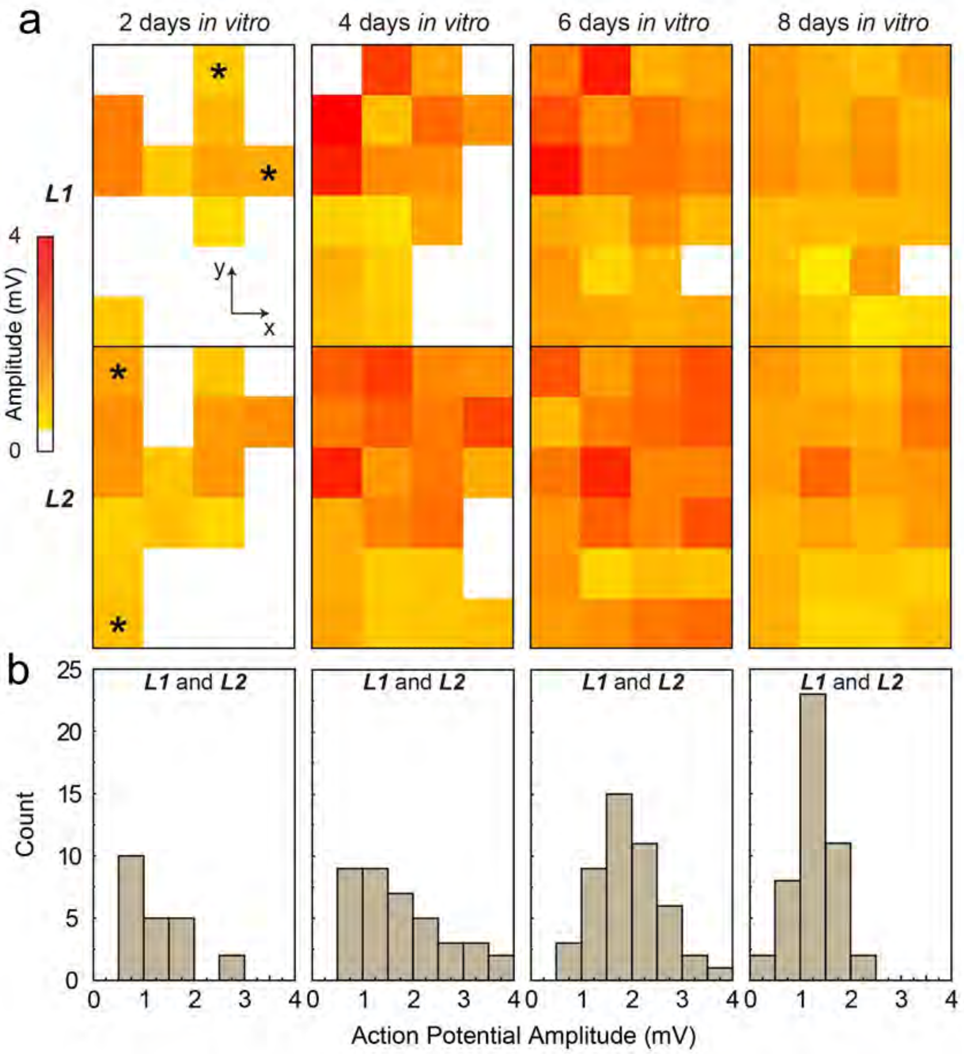

Figure 5.6: AP evolution during tissue development. (a) Amplitudes of spontaneous APs recorded from 4 × 6 NW FET arrays in two layers at 2, 4, 6, 8 DIV. White squares correspond to coordinates where APs are absent or below the detection limit (1× standard deviation of noise level). Time-dependent data recorded from four devices (2× *L1* and 2× *L2*) indicated with asterisks at 2 DIV are shown in Figure 5.7. (b) Histogram of AP amplitudes recorded from the cyborg cardiac tissue sample at 2, 4, 6 and 8 DIV.

It is worth pointing out that the AP conduction patterns looks similar between the different 4 layers (Figure 5.5d), which is due to the small z distance between neighboring layers (∼50 μm) compared to the distance between sensors in the x–y plane. This is due to a common thickness limitation for 3D tissue engineering because of nutrition diffusion and it could be overcome by methods such as vascularization[96, 105, 114].

This platform of cyborg cardiac tissue serves as a unique *in vitro* model to investigate electrophysiological activities across the whole 3D tissue without any labeling processes. Therefore we applied the cyborg cardiac tissue to investigate the evolution of electrophysiological activity during culture and tissue development. 3D real time mapping of APs in from two layers of FET arrays of the cyborg cardiac tissue sample was carried out at 2, 4, 6 and 8 days *in vitro* (DIV) (Figure 5.6a). Qualitatively, analyses of recorded AP maps show that the spontaneous beating volume expands to the entire sample for 6 DIV, while through quantitative analysis, the percentage volume showing detectable beating at 2, 4, 6 and 8 DIV are ca. 46, 79, 98 and 98%, respectively. Interestingly, even for the sparse data at 2 DIV (Figure 5.6a), the detected beating is synchronized within and between device layers (Figure 5.7). These data suggest that 3D conducting pathways, which have been difficult to study in cardiac tissue development with conventional methods, develop early in the engineered tissue, and thus our approach should provide a unique opportunity to address this important issue in the future.

In addition, analysis of the AP data further demonstrates that at 2, 4, 6 and 8 DIV, the beating rate values are 346, 470, 52 and 38 per minute, respectively. The beating rate shows a substantial decrease after 4 DIV, as expected during maturation of rat cardiac tissue. The average extracellular AP amplitude from the sample at 2, 4, 6 and 8 DIV

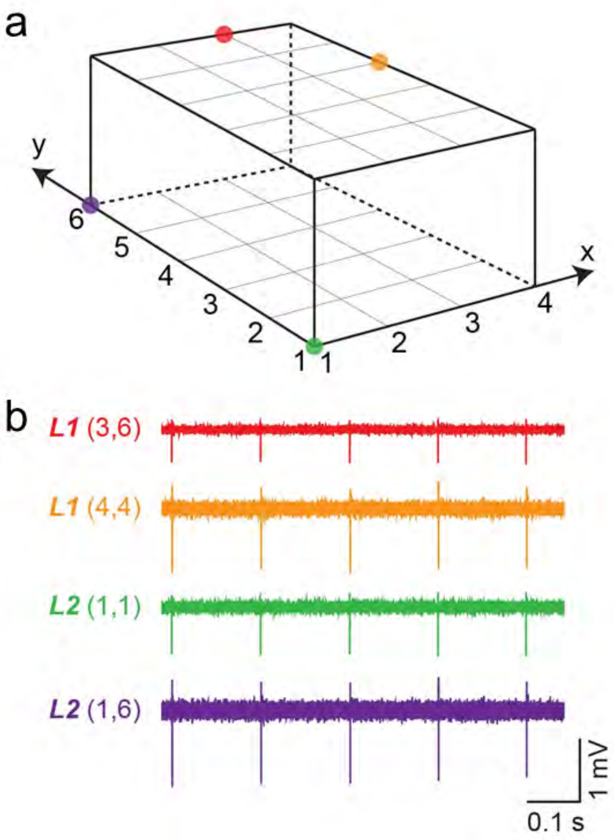

Figure 5.7: Synchronized beating at 2 DIV. Representative recording of APs sequences from four sensors at 2 DIV in the same cyborg cardiac tissue sample as shown in Figure 5.6. (a) Four dots corresponding to the relative positions of the four selected sensors distributed in two layers. (b) Multiplexed recording traces from the four selected sensors showing synchronization of APs.

(Figure 5.6b), 1.27 ± 0.53, 1.77 ± 0.86, 1.92 ± 0.66 and 1.27 ± 0.41 mV, respectively, shows amplitude variation as the tissue develops; that is, initial increase at 2–6 DIV and then decrease at 8 DIV. The observation of an initial increase and subsequent decrease of AP amplitude agrees with a similar trend in maximum upstroke slope[134, 135], since the extracellular AP is directly related to the first-order derivative of intracellular potential, but also an increase in uniformity with the smallest variation through the sample at 8 DIV. We believe these results show that cyborg cardiac tissue can offer detailed insight into the electrophysiological development in 3D, and thus could have impact on studies of different factors relevant to cardiac tissue engineering, including stem cell differentiation, growth factors and ischemia, etc.

5.4 "Cyborg" Cardiac Tissues for Studying Pharmacological Repsonses

We further explore the potential applications of cyborg cardiac tissues for dynamic mapping of 3D cardiac activities in response to the addition of pharmacological chemicals. 1-heptanol and norepinephrine were used to validate the advantages of cyborg cardiac tissue as a powerful platform for pharmacological investigation (Figure 5.8a).

1-heptanol, which is a gap-junction blocker and is used to interfere with the cardiac AP conduction, has been tested first in cyborg cardiac tissue[110]. Figure 5.8b shows the recording of 4 representative sensors selected from each different layer before (Figure 5.8b, top) and 20 minutes after (Figure 5.8b, bottom) adding 20 μM 1-heptanol. The conduction velocity was measured to decrease by ∼17% as a result of 1-heptanol adding. The corresponding 3D isochronal maps before (Figure 5.8c, top) and after (Figure 5.8c, bottom) 1-heptanol addition show unaltered conduction patterns. This result depicts a uniform conduction velocity decrease among the whole tissue.

The ability to determine AP conduction velocity with high-resolution at the single peak level without averaging, provides unique insight into drug diffusion in the tissue. Specifically, time latency changes Δt_1, Δt_2, Δt_3 plotted for the first 30 s following 1-heptanol addition (Figure 5.8d) show that the steady-state ∼17% increase in latency is achieved in only 30 s, but that the onset of the latency increase varies from 8 to 10 s for *L1*–*L2*, to *L3*–*L4*. Importantly, these latter results show clearly our ability to monitor the diffusion and action of 1-heptanol from the top surface through the interior of the tissue in real-time. In comparison, previously reported optical methods can only scan either 3D static structures[122], or to visualize 3D dynamic changes requiring averaging multiple scans to achieve good resolution[120], and thus have difficulty in resolving such behavior in 3D cardiac tissue. Both of them lack the capability to track dynamic processes in a 3D fashion. Based on this advantage, we are able to track different types of fast electrophysiological processes in cyborg cardiac tissues such as acute disease syndrome and responsive electrophysiology under fast electrical stimulations.

Norepinephrine (also known as noradrenaline) has positive chronotropic effects on cardiomyocytes through β-1 adrenergic receptors, as it opens chemical- or ligand-gated ion channels and thus increases the depolarization rate and the heart beating rate (Figure 5.9a)[136]. It is interesting that the conduction velocity also shows a transient increase by 20% at ∼30 s after adding of norepinephrine revealed by latency mapping from simultaneously multiplex recording results (Figure 5.9b). This conduction velocity increase diminished in ∼2 min. Figure 5.9c shows that APs conduction pattern was not altered by norepinephrine during the whole process. This phenomenon is unexpected and has not

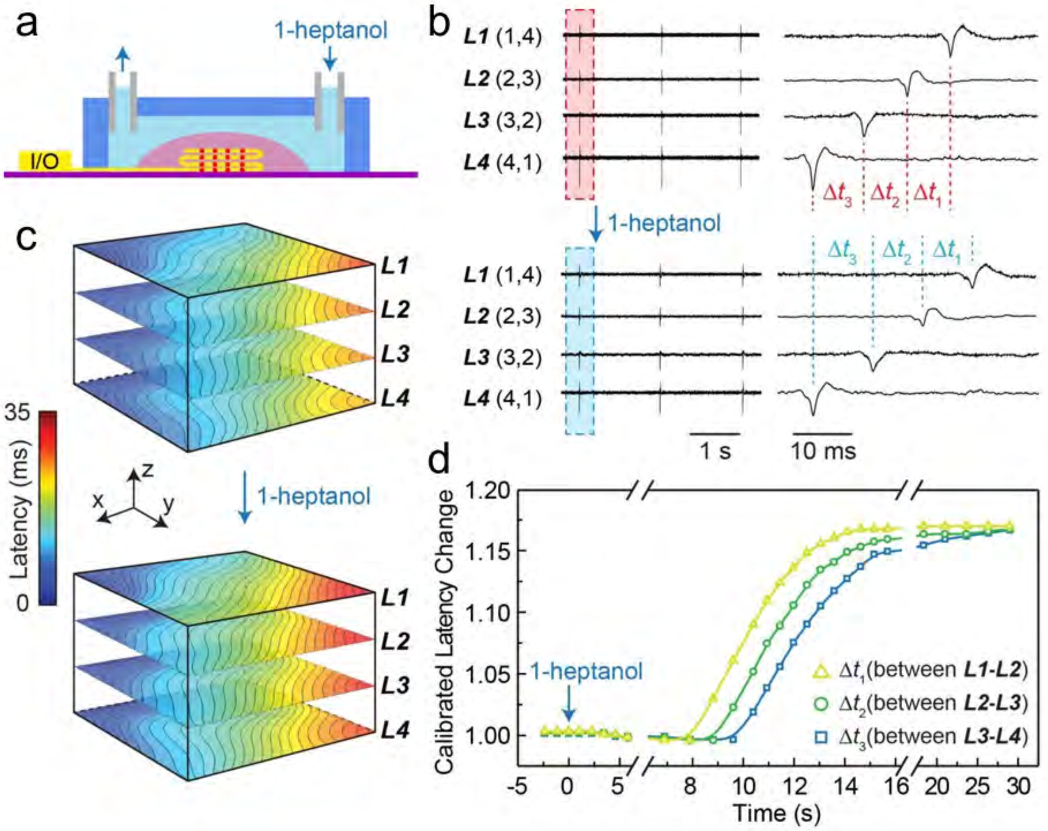

Figure 5.8: 3D mapping of 1-heptanol modulated electrophysiology. (a) Schematic of 1-heptanol perfusion and measurement setup. (b) Representative time-dependent recording from sensors in each of the four layers (*L1*–*L4*) before (top) and after (bottom) adding $20\ \mu\mathrm{M}$ 1-heptanol/Tyrode solution. Time latency Δt_1, Δt_2, Δt_3 correspond to the latency between APs recorded in *L1*–*L2*, *L2*–*L3*, *L3*–*L4*, respectively. (c) 3D isochronal maps of time latency before (top) and after (bottom) adding 1-heptanol. (d) Dynamic changes of the latency Δt_1, Δt_2, Δt_3 between four representative devices versus time before and after adding 1-heptanol.

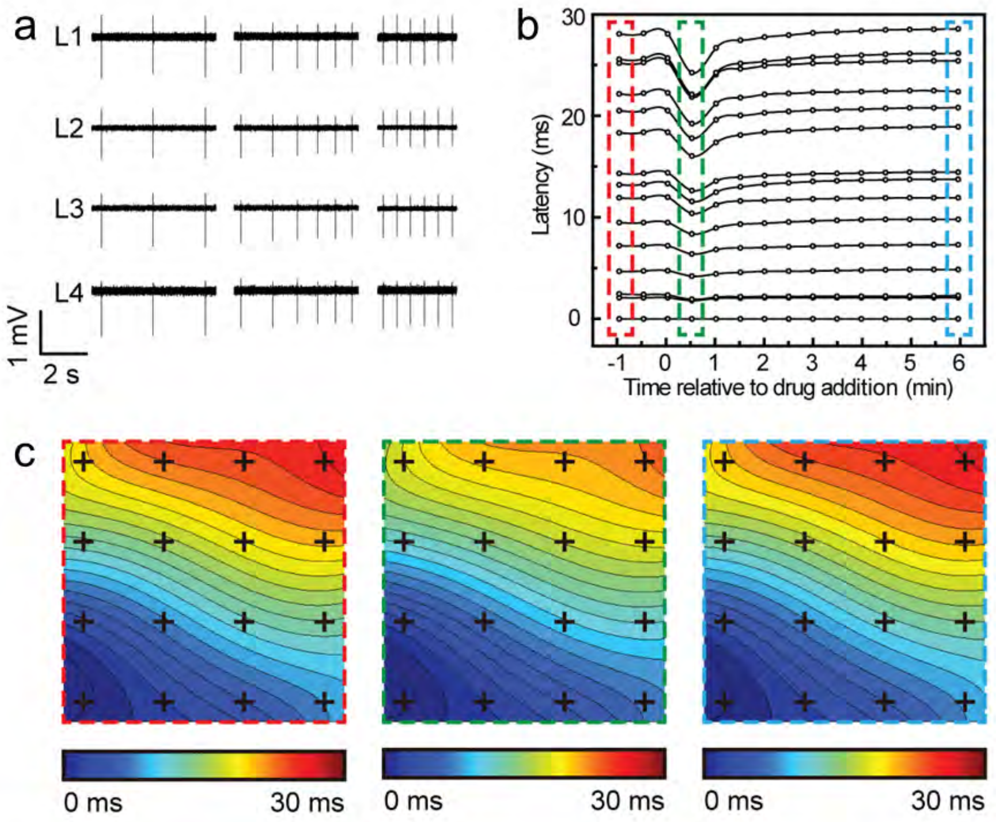

Figure 5.9: Spatiotemporal mapping of norepinephrine modulated electrophysiology. (a) Representative multiplex recording of synchronous extracellular APs in cyborg cardiac tissue before adding norepinephrine (Left), around 30 s after starting perfusing Tyrode medium containing $10\ \mu\mathrm{M}$ norepinephrine (Middle), and after 5 min of adding norepinephrine (Right). Four representative devices were chosen from each of the four layers as labeled. The beating rate continuously increases after adding norepinephrine and reaches stable at $\sim$$150\%$ increase. (b) Simultaneous mapping traces from 16 sensors in layer 1 (top layer) depict the evolution of time latency between each channels after addition of $10\ \mu\mathrm{M}$ norepinephrine. Calculated conduction velocity shows an increase of $\sim$$20\%$ after $\sim$$30$ s of norepinephrine addition and returns to original value after $\sim$$2$ min. (c) Isochronal maps of the extracellular AP conduction in cyborg cardiac tissue at three representative time points (-1 min, 30 s, 6 min relative to norepinephrine addition) show the conduction pattern was unchanged corresponding to norepinephrine addition. Mapping area is 5×5 mm^2.

been observed before because other reported methods are not able to monitor whole tissue fast enough to resolve small difference between two consecutive APs. However, this unexpected transient increase in conduction velocity may indicate a potential acute risk for ventricle arrhythmia which has been neglected before. It can be implied from this example that a more powerful tool may be able to detect more detailed but non-trivial information where the cyborg cardiac tissue shows its potential.

5.5 Conclusion and Prospective

In this chapter, I have demonstrated an approach for building cyborg cardiac tissues by integrating 3D macroporous nanoelectronic scaffolds and engineered cardiac tissue. Based on cyborg cardiac tissues, real-time monitoring of electro-physiological behaviors in 3D engineered cardiac tissues with high spatiotemporal resolution can be possible. We have successfully fabricated more than a hundred detectors with a subcellular device footprint (1–10 μm) and achieved a sub-millisecond time resolution (<0.02 ms) to map cardiac APs in tissue samples of $\sim 5 \times 5 \times 0.2\,\mathrm{mm}^3$ in size. The mechanical and electrical characterization of 3D macroporous nanoelectronic scaffolds has been carried out and state-of-art flexibility leads to an affiliative interface between nanoelectronic scaffolds and engineered tissue. Extracellular APs have been recorded successfully from nearly 100% devices. The cyborg cardiac cardiac tissue has been used to investigate tissue maturation process in real-time, and to visualize the 3D spatiotemporal electrophysiological behaviors with drugs modulation, such as norepinephrine and 1-heptanol. Due to the high temporal resolution of this platform, 3D dynamic evolution of AP characteristics can be first-ever observed, demonstrating the cyborg cardiac tissue as a powerful tool for next generation of drug testing.

Further exploring the cyborg cardiac tissue as a pathological model would be more interesting. To take full advantage of large-scale spatiotemporal mapping of engineered cardiac tissues using cyborg cardiac tissue, diseases/syndromes as a more complicated system happening over cardiac tissues can be visualized as well. Besides, two-way communication between nanoelectronics and tissues can be achieved in the future based on cyborg tissue systems and will potentially lead to simultaneous reading and controlling of biological systems.

6

“Cyborg” Cardiac Tissues as a Potential Platform for Disease Diagnostics and Electronic Therapeutics

6.1 Introduction

The cyborg cardiac tissue has been used to investigate tissue development process in real-time, and to visualize the 3D spatiotemporal changes of APs with drugs. And it has shown its advantages in 3D high spatiotemporal resolution mapping of electrophysiological signals. As a significant advance, more complicated behavior such as diseases or syndromes can also be possible to visualize using cyborg cardiac tissue. In this chapter, I will first introduce a pharmacological method to trigger ventricle arrhythmia tissue model and corresponding diagnostics based on cyborg cardiac tissues.

In addition, we also demonstrated simultaneous monitoring and modulation of AP conduction by incorporating both electrical stimulators with nanoelectronic detectors into 3D cardiac tissues. By applying desirable artificial electrical stimulation, cardiac APs conduction behavior can be altered to the opposite direction of disease syndromes. Our results show that cyborg cardiac tissue may serve as a promising tool not only for electrophysiological and pharmacological studies, but also for potential disease diagnostics and electronic therapeutics.

6.2 "Cyborg" Cardiac Tissues for Building a Ventricle Arrhythmia Disease Model

To further explore the cyborg cardiac tissue as a pharmacological and pathological model, we developed a method to generate transient arrhythmia by adding high dosage norepinephrine. According to the positive chronotropic effects of norepinephrine, it can increase the ventricle automaticity, which can lead to ventricle arrhythmia at high drug dosage. We continuously monitor three sensors I, II and III from layer 1, 2 and 3, with sensor I near the drug adding position and sensor III near the pace-maker while locally adding 100 μM norepinephrine with needle injection (Figure 6.1a). Representative real-time recordings from FET sensors I, II and III in different layers before and following norepinephrine injection near sensor I (Figure 6.1b,c) highlight an instability of several beats post-injection. Specifically, examination of time-correlated AP peaks from these three devices from be-

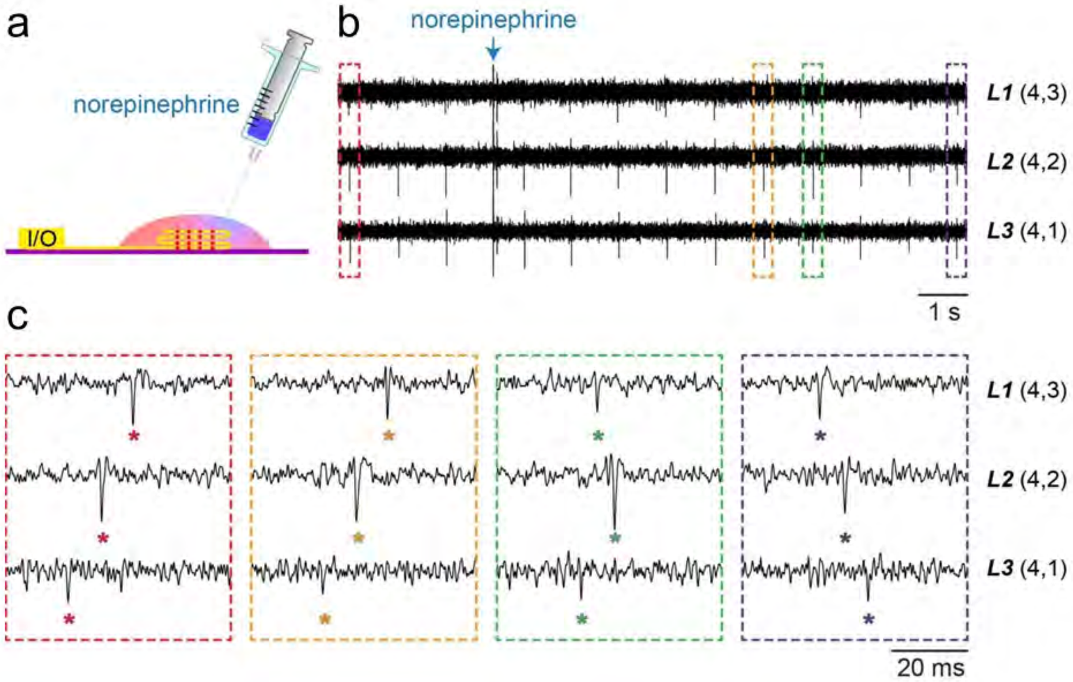

Figure 6.1: Transient arrhythmia induced by locally injected norepinephrine. (a) Schematic of measurement setup highlighting the syringe injection of norepinephrine at a localized spot on the cyborg cardiac tissue. (b) Time-dependent traces from three sensors in *L1*, *L2*, *L3* with synchronized and periodic APs. Blue arrow indicates the injection time point of $\sim 25\ \mu\mathrm{L}$ norepinephrine at concentration of $100\ \mu\mathrm{M}$. (c) Zoom of the four dashed box regions in (b) depicting time latency between action APs before and 5–10 s after norepinephrine addition.

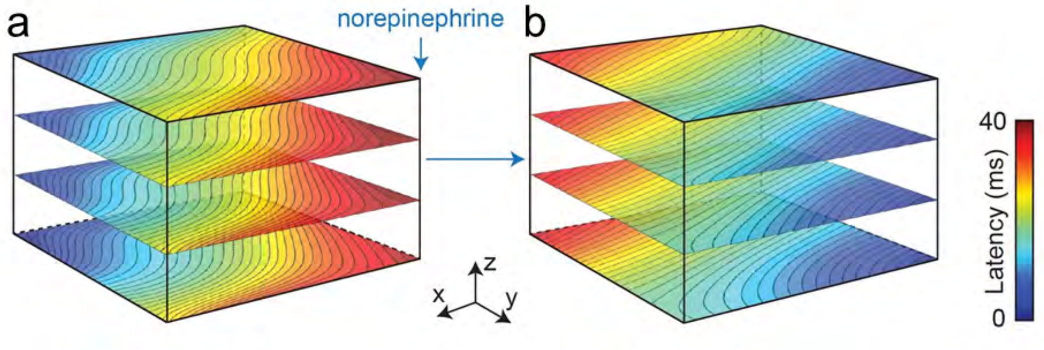

Figure 6.2: Pace-maker shift observed under high dosage norepinephrine. The 3D isochronal maps show the extracellular APs conduction direction and pattern before (I) and 5 min after (II) local norepinephrine injection. Blue arrow in (I) indicates the position at which the norepinephrine was injected. Pace-maker shifts to the position opposite to the norepinephrine addition region.

fore and 5–10 s post-injection (Figure 6.1c) shows that the AP propagates initially from sensor III to I, but that ∼10 s after drug injection the propagation direction is reversed. In the intermediate regime, the recorded peaks indicate a transient increase in beating rate around sensor I, which then leads to the reversal of the overall propagation direction. At steady-state, the full 3D AP isochronal maps (Figure 6.2b) show clearly the stable reversal of propagation direction post-injection. Homogeneous perfusion of norepinephrine (Figure 5.9a) exhibits the typical increase in beating rate to steady-state without a change in propagation direction.

The observed transient beating instability (Figure 6.1b,c) is analogous to ventricular arrhythmia, and can be interpreted similarly for our case. Specifically, the positive chronotropic effect of the locally-delivered norepinephrine induces cells close to sensor I to beat faster than the original pace-maker foci, and after a short intermediate phase when there are two competing pace-maker foci, the new propagation direction (from drug injection region to original pace-maker foci) stabilizes (Figure 6.1d). The capability to spatially and temporally resolve such instabilities within cardiac tissue suggest that the nanolectronics-innervated cardiac tissue could serve as an *in vitro* tissue model for investigating arrhythmia and developing potential therapies using drugs and/or physical stimulation.

6.3 "Cyborg" Cardiac Tissues for Simultaneous Detection and Regulation

In order to demonstrate the capability for real-time active control of the AP conduction in our cyborg cardiac tissue platform, we incorporated electrical stimulators together with FET sensors for simultaneously recording and controlling of cardiac activities. Specifically, four circular metal electrodes with 50/50 nm thick platinum/palladium were integrated into the nanoelectronic scaffold as electrical stimulators at four corners in the layer 4 (Figure 6.3a). The typical impedance of the electrodes is below 100 kΩ (Figure 6.3b) at frequency of 1 kHz (the characteristic frequency for extracellular cardiac activity) and the size of stimulator can be reduced by further surface engineering[137, 138].

Figure 6.4b shows representative recording from the nanoelectronic scaffold containing both FET sensors and stimulators. Explicit measurement of APs is not influenced by the incorporation of electrodes. Then we investigate and the dependence of cardiac activities in the cyborg cardiac tissue on the stimulation voltage amplitudes. When stimulation voltage amplitude is below 100 mV, the APs were not time-correlated to stimulation spikes (Figure 6.4b,d), and AP propagation direction remain unchanged, which is evident from the absence of correlation between AP and stimulation peaks. However, when stimulation voltage was increased above 1 V, the APs from all sensors were observed to synchronize with the stimulation rhythm (Figure 6.4c,d). The AP propagation direction also changes

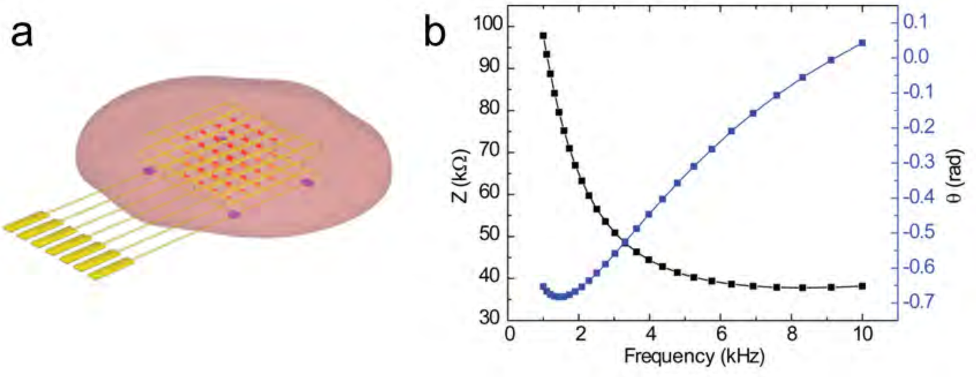

Figure 6.3: Stimulators in 3D macroporous nanoelectronic scaffolds for cyborg cardiac tissue AP control. (a) Schematics illustrates that micro electrodes are incorporated into electronic scaffold for artificial regulation of APs in cyborg cardiac tissue. (b) Frequency dependent impedance characterization of stimulators in 3D macroporous nanoelectronic scaffolds depicts modulus (Z) and phase (θ) for a typical Pt electrodes on the SU-8 mesh structures immersed in a PBS solution.

such that the origin of propagation shifts to the location of stimulator in a manner similar to our observations following focal norepinephrine addition. Under this condition ∼10 μA AC current was injected into the cardiac tissue. The artificially controlled activation successfully overwrites the intrinsic pace-maker foci in the cyborg cardiac tissue, which suggests the possibility to regulate a desired AP conduction overwriting arrhythmia *in vivo*.

In addition, we also explored the electrophysiological effects of different stimulation frequencies in the cyborg cardiac tissue. For example, stimulation data results acquired for at higher frequencies (Figure 6.4e) shows that synchronized and coherent beating can be achieved at up to 2.5 Hz. More interestingly, in a different sample with stable beating rate at ∼1.25 Hz, and measured the cardiac activities are silenced (i.e., there is no beating) under 3.3 Hz stimulation at a stimulation voltage of 1 V (Figure 6.5), although normal beating is observed once the stimulator is turned off. These results show clearly that it is possible to

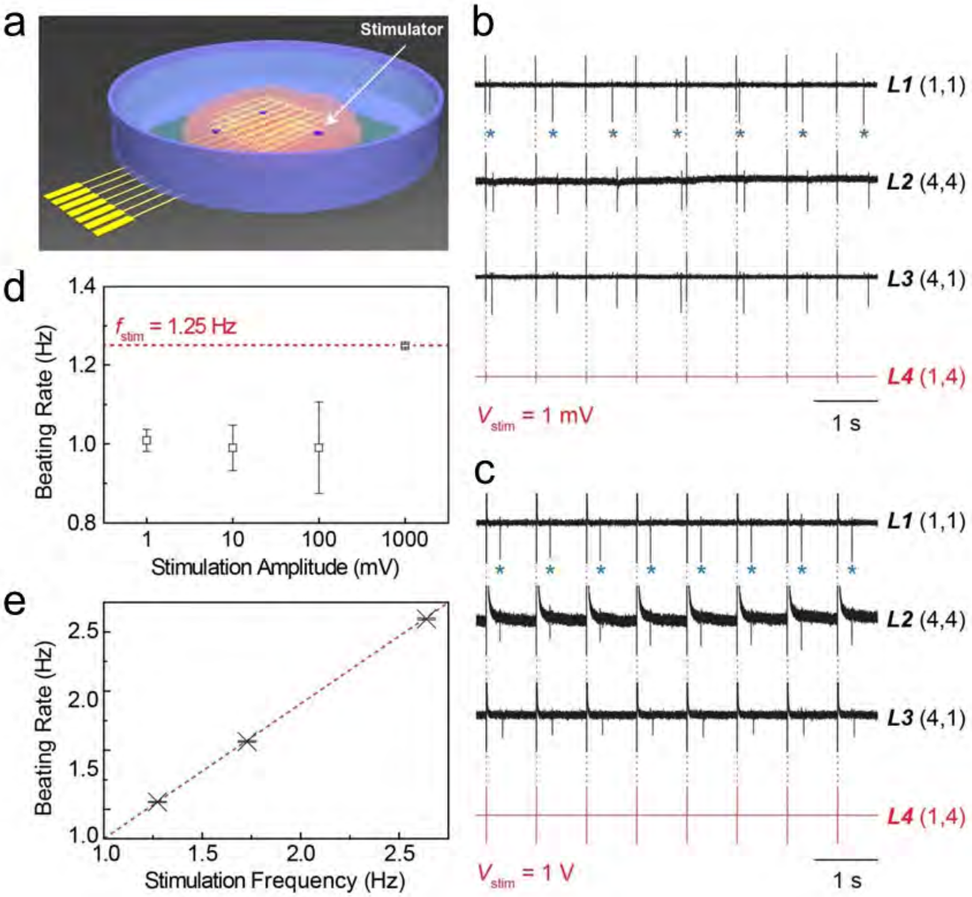

Figure 6.4: Active regulation of APs and tissue beating. (a) Schematic illustrating position of electrode stimulators (purple dots) incorporated in the nanoelectronic scaffold. (b–c) Representative time-dependent traces recorded from NW FETs in layers *L1*, *L2*, *L3* and the periodic stimulation spikes (red) in *L4*; all device coordinates were indicated. Stimulation peak width and frequency were 1 ms and 1.25 Hz, respectively. The stimulation amplitude in (b) and (c) were 1 mV and 1 V, respectively. Red dashed lines align the stimulation spikes and capacitive coupling spikes recorded from FET sensors; recorded AP peaks (primarily downward spikes) occur at distinct times, and are indicated by blue asterisk in *L1* of (b) and (c). (d) Plot showing the beating rate as a function of stimulation amplitude; error bars correspond to ± standard deviation. The stimulation frequency was 1.25 Hz in all experiments. (e) Plot of beating rate versus stimulation frequency; error bars correspond to ± standard deviation. The stimulation amplitude was constant at 1 V, and stimulation frequencies were 1.25, 1.67, 2.50 Hz.

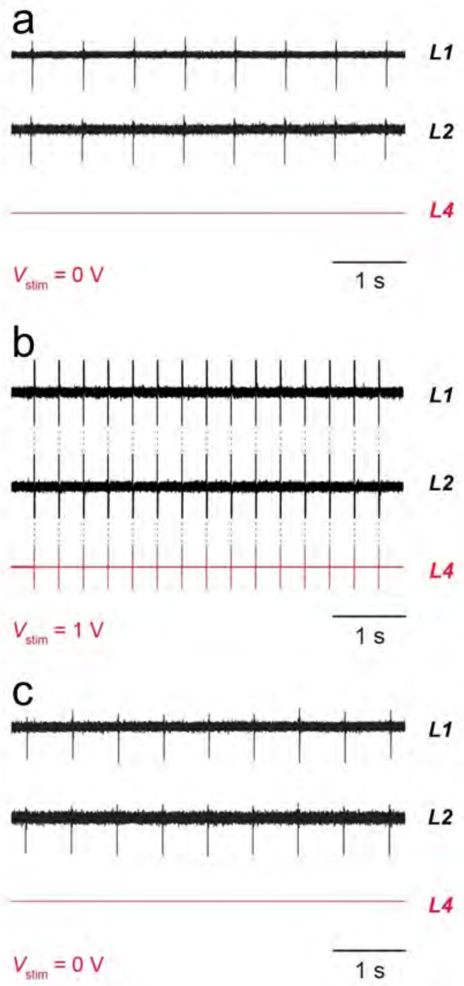

Figure 6.5: Suppression and recovery of tissue beating. (a) Representative multiplexed recordings show spontaneous AP from *L1* and *L2* (black traces) without stimulation. The device coordinates are *L1*(1, 2) and *L2*(3, 1). Beating rate is $\sim$1.5 Hz. (b) Multiplexed AP recordings from the same sensors at a stimulation frequency of 3.33 Hz (red trace), where the stimulator is near *L4*(4, 4). The AP of cyborg cardiac tissue was suppressed throughout the tissue during stimulation; only capacitive coupling from the stimulator was observed from the sensors. (c) Representative multiplex recordings of APs from the same sensors after stopping the 3.33 Hz stimulation as shown in (b). The recorded data shows full recovery of the AP/beating of cyborg cardiac tissue to its original beating frequency of $\sim$1.5 Hz.

inhibit on demand of cardiac activity, and thus could be important for regulating abnormal beating.

6.4 Conclusion and Prospective

In this chapter, simultaneous mapping and controlling of cardiac activities based on cyborg cardiac tissue have been demonstrated. It may open many new opportunities for real time monitoring and artificial intervention of tissues. The fast detection speed of nanoelectronics can reveal electrophysiological changes of cardiac beating from individual cells in the 3D cellular networks, and thus can be used to study the details of AP conduction pattern or acute symptoms in the 3D tissue models for drug testing and disease modeling. We developed a ventricle arrhythmia model based on cyborg cardiac tissues for demonstrating it as a novel platform for disease investigation. In parallel, local stimulation with embedded microelectrodes will allow us to artificially alter the current conduction pattern, which could open a new era of electronic therapeutics. Along with this direction, more sophisticated and powerful nanoelectronic systems could be promised through the exploration of more functionality based on other types of nanodevices such as active and logic nanoelectronics[57, 139].

7

Convex Nanowire Field-effect-transistors for Simultaneous Detection of Action Potential and Contraction Force

7.1 Introduction

The cyborg cardiac tissue has been demonstrated its advantages in 3D high spatiotemporal resolution mapping of electrophysiological signals. As a significant parameter, the contraction force of synthetic heart tissue serves as a key value for assessing the functionality.

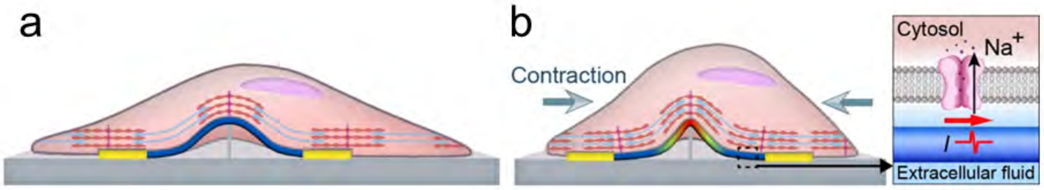

Figure 7.1: Design of convex Si NW FET for simultaneous detection of AP and contraction force. (a) Schematic of convex NW device interfacing with cardiomyocyte. (b) Mechanism for mechanical and electrical sensing.

However, previous methods for measuring the AP and contraction are distinct and exclusive to single function, however, two parameters are intricately correlated. To date, a nanoscale bioprobe that can integrate both functionalities for simultaneous probing bioelectrical and biomechanical processes with the potential for bioelectronic integration has been largely absent. Si NWs, as demonstrated in Chapter 3, are an ideal material for both electrical and mechanical response, therefore can build potential nanodevices for simultaneous detection of APs and contraction force. In this chapter, I will introduce a fine tuned NWs geometry to fully take the advantages of their sensitivity for force and electrical signals (Figure 7.1). Deterministic nanocombing, which is introduced in Chapter 1, is used to assemble and bend the NWs into "Ω" shape. FETs made of these convex NWs demonstrate force sensitivity down to pN, which made simultaneous detection of APs and contraction force from one single cardiomyocyte possible. Synchronous AP and contraction force peaks were decoupled by adding blebbistatin to validate the signals. Further tests on the correlation between NW/cell alignment angle and peak amplitude depict a localized and directional detection of cardiomyocyte contraction. These results reveal the potentials of novel multifunctional cell probes using well-designed nanomaterials and nanodevices.

7.2 Fabrication and Characterization of Convex Nanowire Field-effect-transistors

The Si NWs were grown by a nanocluster-catalyzed VLS method described previously. Briefly, the growth substrate (600 nm SiO_2/Si) was cleaned by oxygen plasma (80 W, 1 min), treated with poly-L-lysine solution for 5 min, and then rinsed thoroughly with DI water. Gold nanoparticles were then dispersed on the growth substrate at a nanoparticle density of ca. $30/\mu m^2$. Specifically, gold nanoparticles with diameters of 15–20 nm were used for the Si NW synthesis. The growth was carried out at 450 °C under a constant pressure of 40 torr, with SiH_4 (2.5 s.c.c.m.), diluted B_2H_6 (100 ppm in He, 3 s.c.c.m.) and H_2 (60 s.c.c.m.) as reactant, doping and carrier gases, respectively. The growth time was ca. 50 min, producing an average length of ca. 60 μm.

The deterministic nanocombing technique relies on pre-patterning of anchoring regions and aligning regions on the NW transfer receiver substrate. Conceptually, laterally deterministic assembly can be enabled by controlling the width and position of the anchoring windows, such that could produce predetermined pitch NW array (Figure 7.2a). For a 3D nanocombing, an array of transverse can also be pre-patterned besides every anchoring window, in order to assemble "Ω"-shaped convex NW array. Detailed steps involve: (1) SU-8 (MicroChem 2002, 1:1 (vol:vol) diluted in MicroChem Thinner-P) was spin-coated and patterned to form transverse with 0.8 μm in height and 1 μm in width at expected device locations. (2) Resist (MicroChem S1805, 1:3 (vol:vol) diluted in MicroChem Thinner-P) at a thickness of ca. 70 nm was spin-coated, exposed using UV light to pattern anchoring regions and aligning regions right beside each transverse on the target substrate. Photoresist was developed (MicroChem MF CD 26 or MF 319) for 50 s, followed by a short DI water rinse (10 s) and nitrogen drying. (3) Immediately after rinsing, substrate was mounted onto

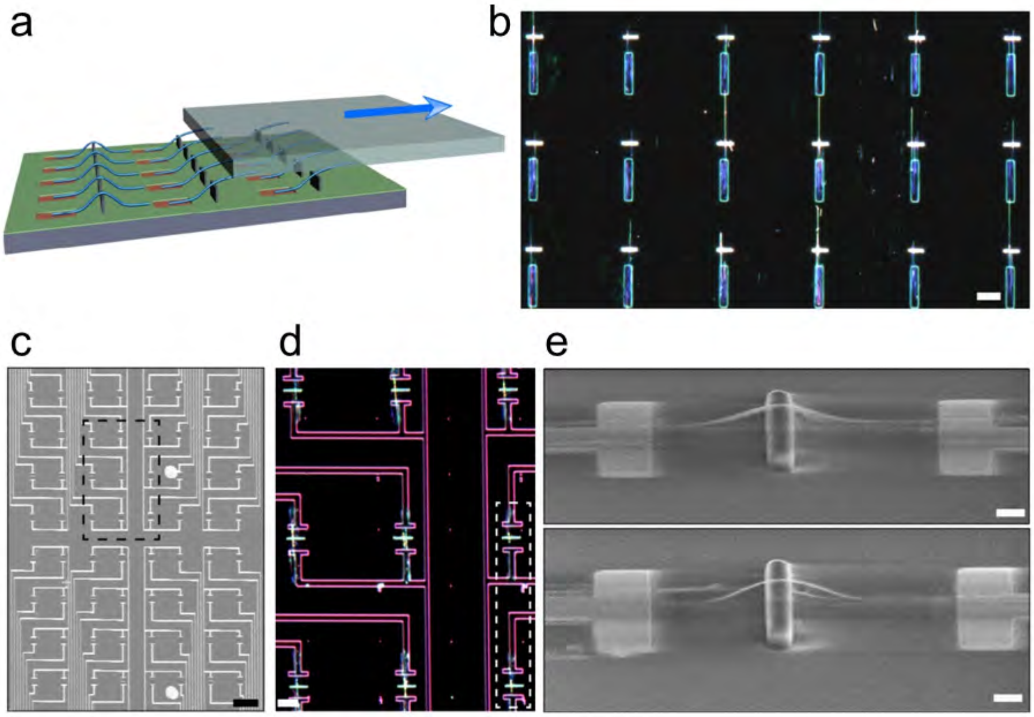

Figure 7.2: Design and fabrication of convex Si NW FET arrays. (a) Schematic of deterministic nanocombing for convex-NW structures. (b) Representative optical image of assembled array. (c) A 8×8 fabricated device array. (d) Zoom-in image of a 3×3 array. (e) Two SEM images of devices corresponding to the dashed box in (d).

a movable stage controlled by a micromanipulator. Approximately 40 μL oil was drop-cast onto the target substrate as lubricant. The growth substrate (ca. 1.2 × 1.2 cm^2) was then brought into contact with the target substrate with a constant pressure of ca. 4.8 N/cm^2. The target substrate was moved by the micromanipulator at a constant velocity of ca. 5 mm/min with respect to the fixed growth substrate for coming. The above procedure can be readily applied to different target substrates such as silicon nitride (Si_3N_4) and sapphire (Al_2O_3) using the same or different resist (SU-8). Following nanocombing transfer, the oil and resist layer were removed with octane.

Dark-field optical images of the convex Si NW arrays obtained from 3D nanocombing (Figure 7.2b) reveal several important points. First, anchoring region with 15 μm in length shows excellent alignment. Second, this high degree of NW alignment was confirmed over macroscopic dimension imaging; that is, nanocombed NWs in 40 arrays over a 2 × 2 mm^2 area of a substrate chip. Statistical analysis of the number of NWs demonstrates over 43% of the device regions contain single NW, with over 75% of the device regions contain 1–6 NWs. Nanocombing ensures that all the aligned NWs deterministically start from the anchoring/combing interface patterned by lithography. Hence, registration of one end can be readily controlled on a substrate. Photolithography was used to define pairs of electrodes around each site of aligned NWs for FET fabrication which can be easiliy scaled up to whole wafer. Each individual NW was then connected using electron-beam lithography. SEM and dark-field optical images (Figure 7.2c,d) demonstrate the high yield of individual NW devices for each site, which is readily achieved due to the excellent NW alignment and end-to-end registration. SEM images (Figure 7.2e) show the fine-tuned "Ω"-shaped NW structure. A typical device yield of convex NW FETs over 90% can be

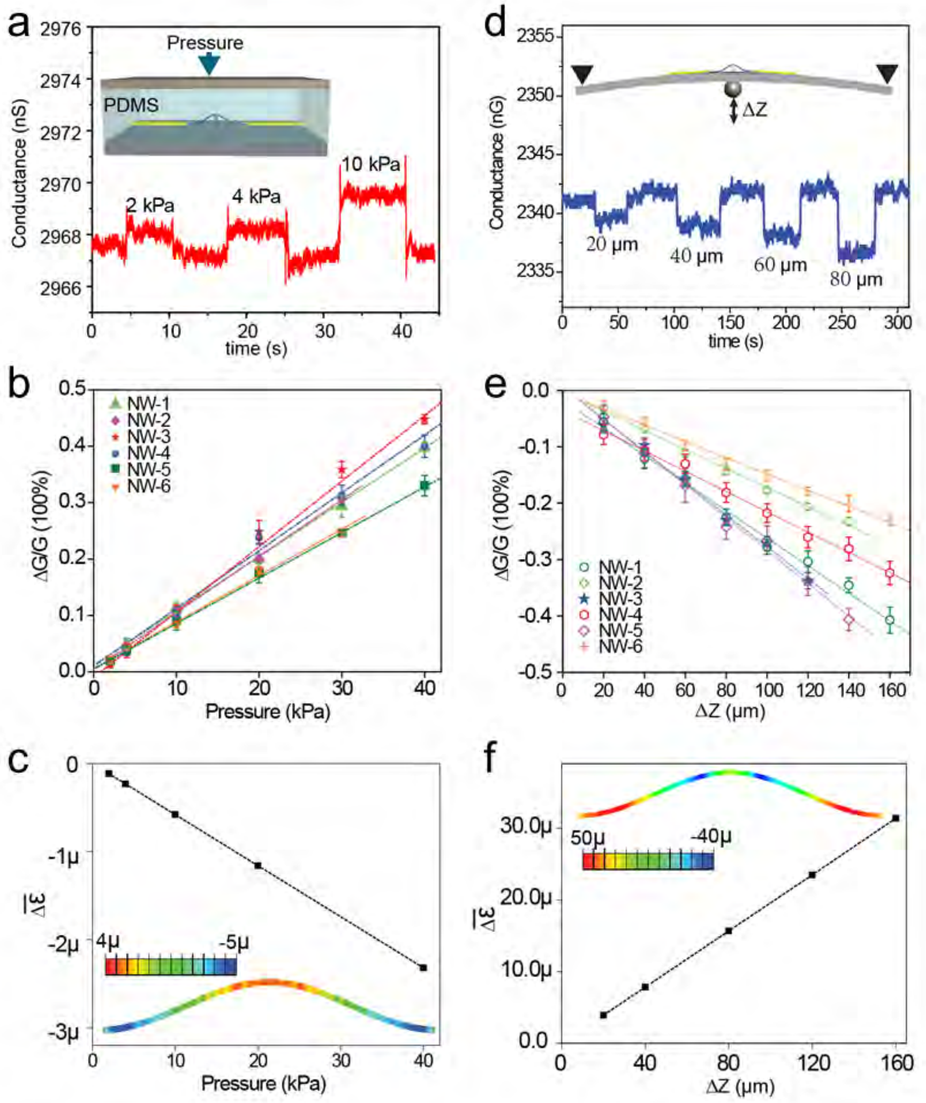

Figure 7.3: Force sensing from convex Si NW FET. (a) Representative signal and schematic shows the characterization experiment of force sensing capability of convex Si NW FETs. The NW FETs are encapsulated within as-casted PDMS elastomer. Arbitrary pressure is applied on the devices. (b) Statistical and linear relationship between conductance and pressure. (c) Simulation reveals strain profile in NW with respect to pressure. (d) Representative signal and schematic shows the characterization experiment of force sensing capability of convex Si NW FETs. Edge of the substrate are fixed while the center region is pushed up to bend the substrate. (e) Statistical and linear relationship between conductance and z-displacement. (f) Simulation reveals strain profile in NW with respect to bending.

achieved by this approach.

The force sensing capability of convex NW FET has been characterized (Figure 7.3). In order to semi-quantitatively apply external stress, two independent experiments were carried out to apply controllable strain to the convex NW FET arrays. (1) The convex NW FET were firstly encapsulated by PDMS, using direct drop-casting and in-situ curing approach. Pressure was then applied on top of the sensor region, which is in the center of wafer and conductance of each sensor is individually measured in parallel (Figure 7.3a). (2) The substrate was fixed while the center region was pushed up by a sapphire sphere controlled by a micromanipulator. At the same time, each sensor is individually measured (Figure 7.3d). Collected signals were filtered through a home-built conditioner with band-pass of 0–6 kHz, digitized at a sampling rate of 20 kHz (Digidata 1440A).

Collected electrical measurement results reveal linear relationship between the conductance change and the applied pressure or z-displacement. Notably, compression was generated by the pressure on top of the PDMS and tension was generated by the bending of the substrate (Figure 7.3b,d). Force sensitivity can be calculated by the dependence between averaged force along NW and the detection limit (1× standard deviation) of conductance change. Finite element analysis was carried out to estimate the averaged strain along NW under certain uniform pressure on top of the silicone elastomer or z-displacement to the center of the substrate (Figure 7.3c,f).

7.3 Simultaneous Detection of Action Potential and Contraction Force from Individual Cardiomyocyte

Convex NW FET arrays were used for simultaneous detection of extracellular APs and contraction from cardiomyocytes (Figure 7.1b). A self-modified polystyrene petri-dish was mounted onto device ship using Kwik-Sil silicone elastomer adhersive. Then device was sterilized by UV-light illumination for 0.5 h and soaking in 70% ethanol solution for 0.5 h, followed by oxygen plasma (50 W, 1 min) treatment. Then the cyborg cardiac tissue scaffolds were thoroughly immersed in fibronectin/gelatin solution for 2 h before cell plating for surface modification as described before. Primary neonatal rat cardiomyocytes were prepared according to previously published procedures[11, 72]. Briefly, intact ventricles were isolated from 1–3 day old Sprague/Dawley rats and were then digested at 37 °C in HBSS containing collagenase (class II, Worthington Biochemical). Isolated cells were suspended in the culture medium comprising 5% FBS and 95% Medium 199, supplemented with 0.12 mmol/L $CuSO_4$, 0.1 mmol/L $ZnSO_4$ and 1.5 mmol/L VB_{12}, 500 U ml^{-1} penicillin and 100 mg ml^{-1} streptomycin. The cell suspension was pre-plated in a flask for 2 h to reduce the percentage of non-cardiomyocyte cells. Then the collected supernant was concentrated and plated at a cell density of $2.5\times10^5/cm^2$. Cells are cultured for 1–7 day before conducting electrical measurement.

Electrical measurement was carried out in Tyrode solution at 37 °C by precisely controlled using temperature controller. All the studies were carried out and in. A Ag/AgCl wire was used as a reference electrode and the conductance of Si NW FET was measured with DC bias set to 100 mV. Figure 7.4a,b show negatively peaked extracellular APs and contraction force obtained from three representative devices. Contraction signals have a

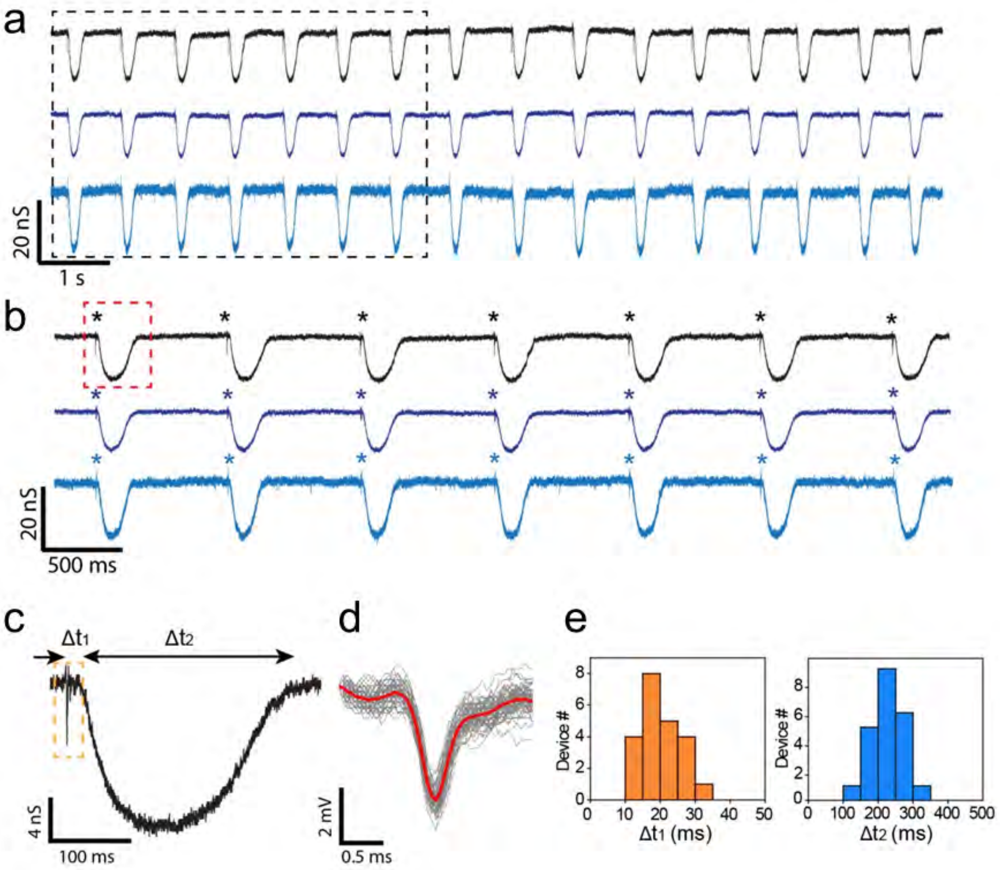

Figure 7.4: Simultaneous recording of extracellular AP and contraction force from single cardiomyocyte. (a) Representative recording traces show both extracellular AP and contraction force are clearly measured simultaneously. (b) Zoom-in of black dashed-box in (a) showing 7 periods of beating. Extracellular AP peaks are marked by asterisks. (c) Zoom-in of red dashed-box in (b) showing details in one period with the overlaying signal of AP and contraction. Delay time between electrical and mechanical signal is labeled as Δt_1, and the duration of the mechanical signal is labeled as Δt_2. (d) Overlay of collected extracellular APs showing the typical features. (e) Histogram of the delay time between electrical and mechanical signal, Δt_1, and the duration of the mechanical signal, Δt_2.

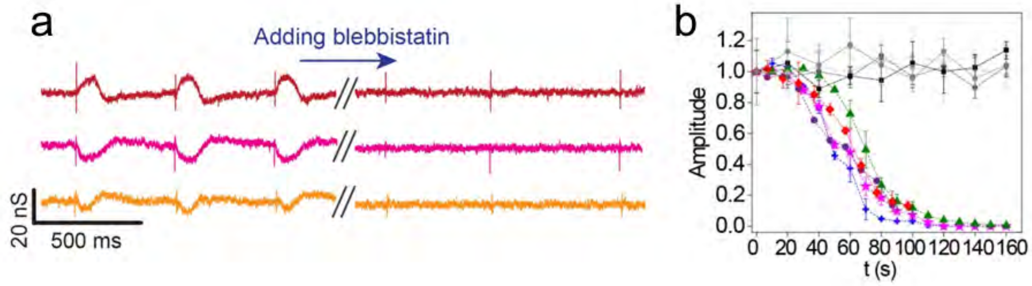

Figure 7.5: Recording of extracellular AP and contraction force from blebbistatin modulated cardiomyocyte. (a) Representative recording traces before (left) and after (right) applying 100 μM blebbistatin solution. (b) Time-dependent evolution of mechanical signals (color curves) and electrical signal (dark curves) amplitudes.

characteristic peak width at ca. 250 ms and amplitude at 100 nS (Figure 7.4c,e); extracellular APs have a characteristic peak width at 1 ms and amplitude at 50 nS (Figure 7.4d,e). The two peaks are corresponding to the intracellular calcium induced calcium release process and sodium channel openning of AP process, and can be easily differentiated. The calculated contraction force for single cardiomyocytes is ca. 3 nN, which is consistent from previously reported results. In order to further verify the classification of extracellular AP and contraction peaks, blebbistatin, which is a cardiomyocyte contraction inhibitor, has been used for drug control test (Figure 7.5). Under 100 μM of blebbistatin the contraction of cardiomyocytes are fully suppressed but the extracellular AP peaks are still intact (Figure 7.5b), which demonstrates that both clear and clean sensing of extracellular AP and contraction was achieved from convex NW FET device.

As seen from the electrical measurement from blebbistatin modulated cardiomyocytes (Figure 7.5a), both positive and negative contraction peaks have been detected, which may due to different compression/tension from cells contracting along different directions. To

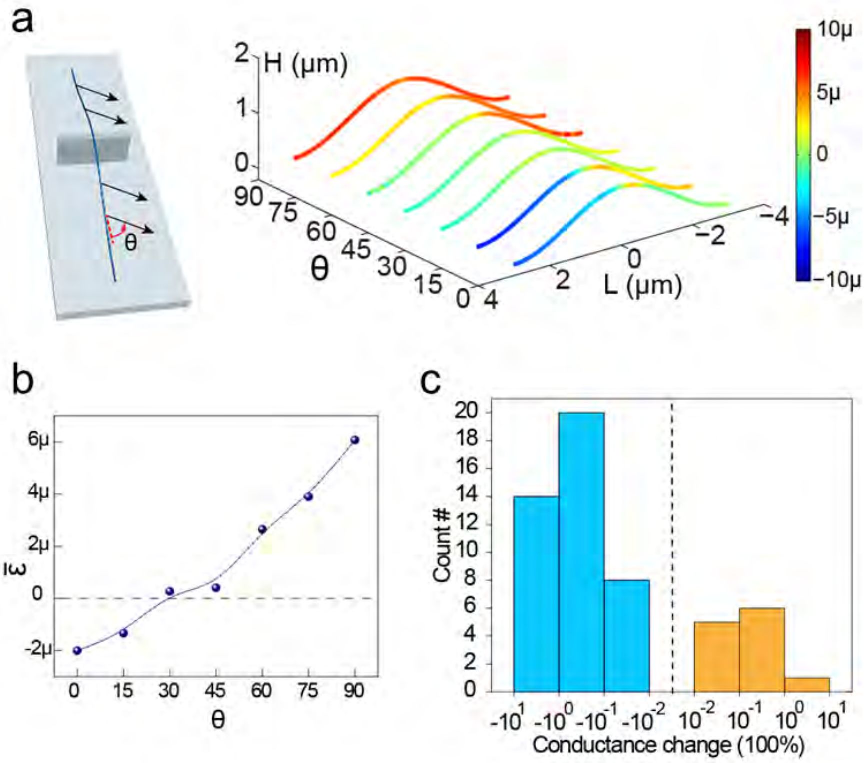

Figure 7.6: Angle dependent force sensitivity. (a) A schematic (left) of directional forces exerted on NW by cell with a angle θ between force direction and NW. Simulation (right) of the strain profile of the NW interfacing with cell, characterized by the angle θ. (b) Simulation result of the average strain built up in the NW with respect to angle θ, highlighting a transition/threshold angle at $\sim 30^\circ$. (c) Histogram of statistical distribution of observed mechanical signals with different sign and amplitude.

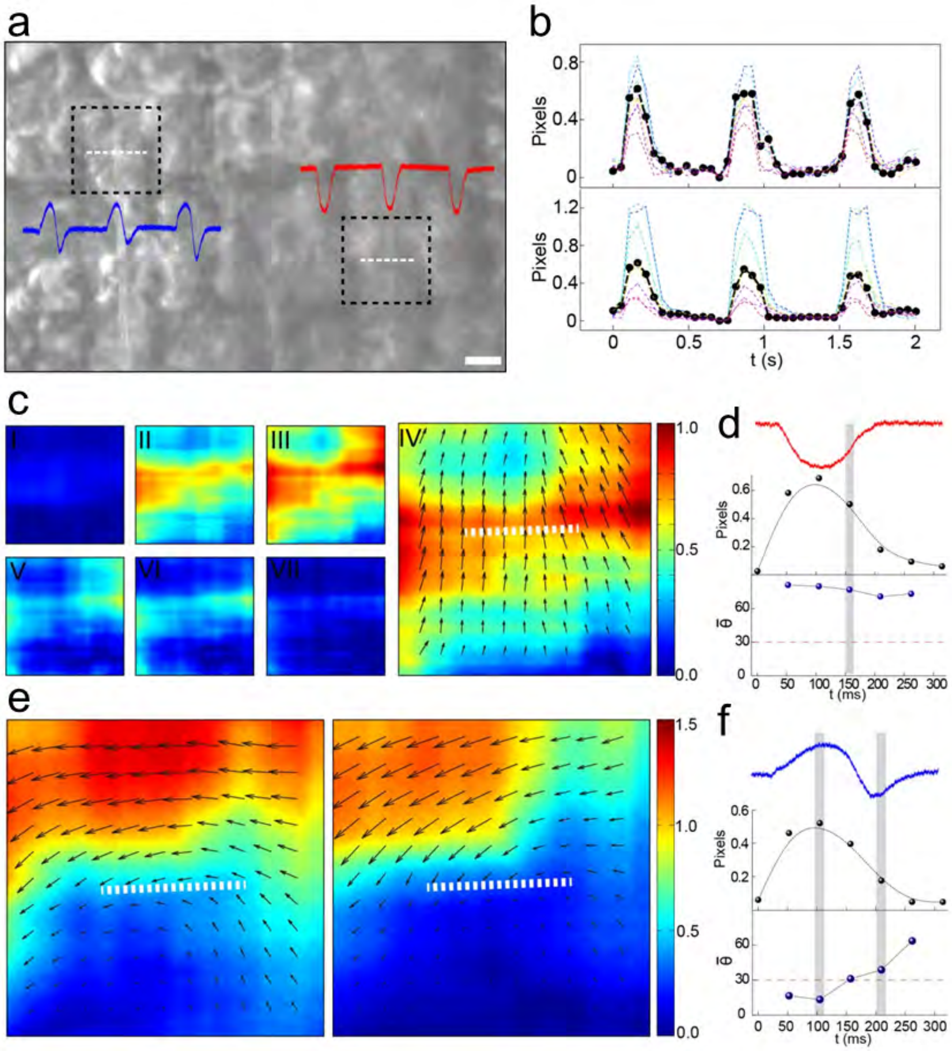

Figure 7.7: Mechanical signals from cells contracting at different angles. (a) Optical image of cardiomyocytes cultured on device arrays, with two devices highlighted in dashed boxes along with their corresponding electrical signals. (b) Pixel displacements at local region are all consistent with electrical recording. (c) A serials of contour maps (pixel shift) for one contraction period for the red signal in (a); one key frame (IV) also included shift vectors with white dashed line indicating NW. (d) Averaged pixel shift (middle panel) and angle (bottom panel), correlating to electrical signal. (e) Two highlighted frames contour maps (pixel shift) for one contraction period for the blue signal in (a), showing the changing of the vector direction. (f) Averaged pixel shift (middle panel) and angle (bottom panel), correlating to electrical signal.

prove this hypothesis, finite element analysis was carried out to estimate the averaged strain along NW with cell contracting in different directions. Figure 7.6a shows the strain profile along NW when cell is contracting at an angle θ comparative to the direction of NW. The averaged strain shifts from compression to tension when the angle θ changing from 0° to 90°, with the threshold angle at $\sim$30° (Figure 7.6b). By having randomly distributed cardiomyocyte on top of entire convex NW FET arrays, the statistics of conductance change based on the simulation results has been analyzed. The approximate 70%/30% negative/positive conductance change is consistent with our collected electrical measurement statistical results (Figure 7.6c).

Here we show two representative cases with different measured electrical signal polarities (Figure 7.7a). Motion tracking analysis was carried out using Lucas-Kanade algorithm through Matlab to visualize the displacement amplitude and direction of each pixel around the device locations. Scatter plots of displacement amplitude over several beating periods show stable and replicable feature between diffenent beating cycles (Figure 7.7b). Detailed displacement mapping across each beating behavior reveals several important points around the convex NW FET device shown on the right side of Figure 7.7a. (1) Displacement amplitude shows an initial increase from 1st to 4th frame and subsequent decrease to nearly 0 from 4th to 7th frame, which is consistent of time scale the contraction of cardiomyocyte beating (Figure 7.7c,d). (2) Displacement angle θ shows a constant $\sim$90° across the entire beating cycle, which is consistent with a compressive strain based on the angle-dependent force sensitivity as shown above (Figure 7.7c,d). On the other hand, around the convex NW FET device shown on the left side of Figure 7.7a, the 3rd and 5th frame of one beating cycle reveal clearly the contraction direction change from $<$30° to $>$30°, corresponding to an averaged strain change from compression to tension (Figure 7.7e,f). This result is also consistent with the biphasic contraction force signals recorded from each single beating cycle. The perfectly matched simulation and recording results validate the proposed relationship of electrical measurement peak polarity and cell/NW angle θ.

7.4 Conclusion and Prospective

In this chapter, we have demonstrated a subcellular scale nanodevice built by "Ω"-shaped NWs. 3D nanocombing on elastomer transverse has been developed to achieve high yield assembly of "Ω"-shaped NW arrays. Nanoscale FET made of single "Ω"-shaped NW with protruding channel interfacing with cultured cells realize the simultaneous detection of extracellular APs and cardiac contraction force. Force sensitivity achieved by convex Si NW FET is ca. 6 pN, which is consistent with finite element analysis. Besides, the detection of cellular motion is highly dependent on the local geometry between cardiomyocyte and convex NW. It has been observed that cardiomyocyte contraction can generate tension or compression on the NW under different angle θ between cell contraction and NW. This strategy successfully take the advantages of high controllability of "bottom-up" synthesized nanomaterials and proves the capability of detecting dual cellular parameters in parallel. To this end, with further development in the integration of novel nanoscale devices and 3D macroporous nanoelecronic networks, multifunctional interaction between nanoelectronics and living tissues can be achieved in the coming generation of cyborg tissues.

References

[1] G. H. Gelinck, H. E. Huitema, E. van Veenendaal, E. Cantatore, L. Schrijnemakers, J. B. van der Putten, T. C. Geuns, M. Beenhakkers, J. B. Giesbers, B. H. Huisman, E. J. Meijer, E. M. Benito, F. J. Touwslager, A. W. Marsman, B. J. van Rens, and D. M. de Leeuw. Flexible active-matrix displays and shift registers based on solution-processed organic transistors. *Nature Materials*, 3:106–110, 2004.

[2] G. Yu, J. Gao, J. C. Hummelen, F. Wudl, and A. J. Heeger. Polymer photovoltaic cells - enhanced efficiencies via a network of internal donor-acceptor heterojunctions. *Science*, 270:1789–1791, 1995.

[3] M. Reyes-Reyes, K. Kim, J. Dewald, R. Lopez-Sandoval, A. Avadhanula, S. Curran, and D. L. Carroll. Meso-structure formation for enhanced organic photovoltaic cells. *Organic Letters*, 7:5749–5752, 2005.

[4] D. Y. Khang, H. Jiang, Y. Huang, and J. A. Rogers. A stretchable form of single-crystal silicon for high-performance electronics on rubber substrates. *Science*, 311: 208–212, 2006.

[5] S. R. Forrest. The path to ubiquitous and low-cost organic electronic appliances on plastic. *Nature*, 428:911–918, 2004.

[6] D. H. Kim, J. Viventi, J. J. Amsden, J. L. Xiao, L. Vigeland, Y. S. Kim, J. A. Blanco, B. Panilaitis, E. S. Frechette, D. Contreras, D. L. Kaplan, F. G. Omenetto, Y. G. Huang, K. C. Hwang, M. R. Zakin, B. Litt, and J. A. Rogers. Dissolvable films of silk fibroin for ultrathin conformal bio-integrated electronics. *Nature Materials*, 9: 511–517, 2010.

[7] D. H. Kim, N. S. Lu, R. Ma, Y. S. Kim, R. H. Kim, S. D. Wang, J. Wu, S. M. Won, H. Tao, A. Islam, K. J. Yu, T. I. Kim, R. Chowdhury, M. Ying, L. Z. Xu, M. Li,

H. J. Chung, H. Keum, M. McCormick, P. Liu, Y. W. Zhang, F. G. Omenetto, Y. G. Huang, T. Coleman, and J. A. Rogers. Epidermal electronics. *Science*, 333:838–843, 2011.

[8] E. W. Keefer, B. R. Botterman, M. I. Romero, A. F. Rossi, and G. W. Gross. Carbon nanotube coating improves neuronal recordings. *Nature Nanotechnology*, 3:434–439, 2008.

[9] D. H. Kim, N. S. Lu, R. Ghaffari, Y. S. Kim, S. P. Lee, L. Z. Xu, J. A. Wu, R. H. Kim, J. Z. Song, Z. J. Liu, J. Viventi, B. de Graff, B. Elolampi, M. Mansour, M. J. Slepian, S. Hwang, J. D. Moss, S. M. Won, Y. G. Huang, B. Litt, and J. A. Rogers. Materials for multifunctional balloon catheters with capabilities in cardiac electrophysiological mapping and ablation therapy. *Nature Materials*, 10:316–323, 2011.

[10] B. Z. Tian, T. Cohen-Karni, Q. Qing, X. J. Duan, P. Xie, and C. M. Lieber. Three-dimensional, flexible nanoscale field-effect transistors as localized bioprobes. *Science*, 329:830–834, 2010.

[11] B. Z. Tian, J. Liu, T. Dvir, L. H. Jin, J. H. Tsui, Q. Qing, Z. G. Suo, R. Langer, D. S. Kohane, and C. M. Lieber. Macroporous nanowire nanoelectronic scaffolds for synthetic tissues. *Nature Materials*, 11:986–994, 2012.

[12] E. M. Vogel. Technology and metrology of new electronic materials and devices. *Nature Nanotechnology*, 2:25–32, 2007.

[13] M. A. Meitl, Z. T. Zhu, V. Kumar, K. J. Lee, X. Feng, Y. Y. Huang, I. Adesida, R. G. Nuzzo, and J. A. Rogers. Transfer printing by kinetic control of adhesion to an elastomeric stamp. *Nature Materials*, 5:33–38, 2006.

[14] A. Dodabalapur. Organic and polymer transistors for electronics. *Materials Today*, 9: 24–30, 2006.

[15] T. Someya, Y. Kato, T. Sekitani, S. Iba, Y. Noguchi, Y. Murase, H. Kawaguchi, and T. Sakurai. Conformable, flexible, large-area networks of pressure and thermal sensors with organic transistor active matrixes. *Proceedings of the National Academy of Sciences of the United States of America*, 102:12321–12325, 2005.

[16] J. Y. Ouyang, C. W. Chu, C. R. Szmanda, L. P. Ma, and Y. Yang. Programmable polymer thin film and non-volatile memory device. *Nature Materials*, 3:918–922, 2004.

[17] P. F. Baude, D. A. Ender, M. A. Haase, T. W. Kelley, D. V. Muyres, and S. D. Theiss. Pentacene-based radio-frequency identification circuitry. *Applied Physics Letters*, 82: 3964–3966, 2003.

[18] E. C. P. Smits, S. G. J. Mathijssen, P. A. van Hal, S. Setayesh, T. C. T. Geuns, K. A. H. A. Mutsaers, E. Cantatore, H. J. Wondergem, O. Werzer, R. Resel, M. Kemerink, S. Kirchmeyer, A. M. Muzafarov, S. A. Ponomarenko, B. de Boer, P. W. M. Blom, and D. M. de Leeuw. Bottom-up organic integrated circuits. *Nature*, 455:956–959, 2008.

[19] C. B. Murray, C. R. Kagan, and M. G. Bawendi. Synthesis and characterization of monodisperse nanocrystals and close-packed nanocrystal assemblies. *Annual Review of Materials Science*, 30:545–610, 2000.

[20] V. F. Puntes, K. M. Krishnan, and A. P. Alivisatos. Colloidal nanocrystal shape and size control: The case of cobalt. *Science*, 291:2115–2117, 2001.

[21] S. Iijima. Helical microtubules of graphitic carbon. *Nature*, 354:56–58, 1991.

[22] A. M. Morales and C. M. Lieber. A laser ablation method for the synthesis of crystalline semiconductor nanowires. *Science*, 279:208–211, 1998.

[23] X. S. Li, W. W. Cai, J. H. An, S. Kim, J. Nah, D. X. Yang, R. Piner, A. Velamakanni, I. Jung, E. Tutuc, S. K. Banerjee, L. Colombo, and R. S. Ruoff. Large-area synthesis of high-quality and uniform graphene films on copper foils. *Science*, 324:1312–1314, 2009.

[24] K. S. Kim, Y. Zhao, H. Jang, S. Y. Lee, J. M. Kim, K. S. Kim, J. H. Ahn, P. Kim, J. Y. Choi, and B. H. Hong. Large-scale pattern growth of graphene films for stretchable transparent electrodes. *Nature*, 457:706–710, 2009.

[25] D. Whang, S. Jin, Y. Wu, and C. M. Lieber. Large-scale hierarchical organization of nanowire arrays for integrated nanosystems. *Nano Letters*, 3:1255–1259, 2003.

[26] C. M. Lieber. Nanoscale science and technology: Building a big future from small things. *MRS Bulletin*, 28:486–491, 2003.

[27] W. Lu and C. M. Lieber. Semiconductor nanowires. *Journal of Physics D-Applied Physics*, 39:387–406, 2006.

[28] X. C. Jiang, Q. H. Xiong, S. Nam, F. Qian, Y. Li, and C. M. Lieber. Inas/inp radial nanowire heterostructures as high electron mobility devices. *Nano Letters*, 7: 3214–3218, 2007.

[29] B. Z. Tian, P. Xie, T. J. Kempa, D. C. Bell, and C. M. Lieber. Single-crystalline kinked semiconductor nanowire superstructures. *Nature Nanotechnology*, 4:824–829, 2009.

[30] X. C. Jiang, B. Z. Tian, J. Xiang, F. Qian, G. F. Zheng, H. T. Wang, L. Q. Mai, and C. M. Lieber. Rational growth of branched nanowire heterostructures with synthetically encoded properties and function. *Proceedings of the National Academy of Sciences of the United States of America*, 108:12212–12216, 2011.

[31] J. Xiang, W. Lu, Y. J. Hu, Y. Wu, H. Yan, and C. M. Lieber. Ge/si nanowire heterostructures as high-performance field-effect transistors. *Nature*, 441:489–493, 2006.

[32] F. Qian, S. Gradecak, Y. Li, C. Y. Wen, and C. M. Lieber. Core/multishell nanowire heterostructures as multicolor, high-efficiency light-emitting diodes. *Nano Letters*, 5: 2287–2291, 2005.

[33] Y. Cui, Q. Q. Wei, H. K. Park, and C. M. Lieber. Nanowire nanosensors for highly sensitive and selective detection of biological and chemical species. *Science*, 293: 1289–1292, 2001.

[34] F. Patolsky, G. Zheng, and C. M. Lieber. Fabrication of silicon nanowire devices for ultrasensitive, label-free, real-time detection of biological and chemical species. *Nature Protocols*, (4):1711–1724, 2006.

[35] X. F. Duan, C. M. Niu, V. Sahi, J. Chen, J. W. Parce, S. Empedocles, and J. L. Goldman. High-performance thin-film transistors using semiconductor nanowires and nanoribbons. *Nature*, 425:274–278, 2003.

[36] Y. Huang, X. F. Duan, Y. Cui, L. J. Lauhon, K. H. Kim, and C. M. Lieber. Logic gates and computation from assembled nanowire building blocks. *Science*, 294:1313–1317, 2001.

[37] A. R. Tao, J. X. Huang, and P. D. Yang. Langmuir-blodgettry of nanocrystals and nanowires. *Accounts of Chemical Research*, 41:1662–1673, 2008.

[38] D. W. Wang, Y. L. Chang, Z. Liu, and H. J. Dai. Oxidation resistant germanium nanowires: Bulk synthesis, long chain alkanethiol functionalization, and langmuir-blodgett assembly. *Journal of the American Chemical Society*, 127:11871–11875, 2005.

[39] A. Javey, S. Nam, R. S. Friedman, H. Yan, and C. M. Lieber. Layer-by-layer assembly of nanowires for three-dimensional, multifunctional electronics. *Nano Letters*, 7: 773–777, 2007.

[40] Z. Y. Fan, J. C. Ho, Z. A. Jacobson, R. Yerushalmi, R. L. Alley, H. Razavi, and A. Javey. Wafer-scale assembly of highly ordered semiconductor nanowire arrays by contact printing. *Nano Letters*, 8:20–25, 2008.

[41] S. Nam, X. C. Jiang, Q. H. Xiong, D. Ham, and C. M. Lieber. Vertically integrated, three-dimensional nanowire complementary metal-oxide-semiconductor circuits. *Proceedings of the National Academy of Sciences of the United States of America*, 106: 21035–21038, 2009.

[42] M. C. McAlpine, H. Ahmad, D. W. Wang, and J. R. Heath. Highly ordered nanowire arrays on plastic substrates for ultrasensitive flexible chemical sensors. *Nature Materials*, 6:379–384, 2007.

[43] B. P. Timko, T. Cohen-Karni, G. H. Yu, Q. Qing, B. Z. Tian, and C. M. Lieber. Electrical recording from hearts with flexible nanowire device arrays. *Nano Letters*, 9:914–918, 2009.

[44] K. Takei, T. Takahashi, J. C. Ho, H. Ko, A. G. Gillies, P. W. Leu, R. S. Fearing, and A. Javey. Nanowire active-matrix circuitry for low-voltage macroscale artificial skin. *Nature Materials*, 9:821–826, 2010.

[45] J. Yao, H. Yan, and C. M. Lieber. A nanoscale combing technique for the large-scale assembly of highly aligned nanowires. *Nature Nanotechnology*, 8:329–335, 2013.

[46] G. F. Zheng, F. Patolsky, Y. Cui, W. U. Wang, and C. M. Lieber. Multiplexed electrical detection of cancer markers with nanowire sensor arrays. *Nature Biotechnology*, 23:1294–1301, 2005.

[47] B. M. Venkatesan and R. Bashir. Nanopore sensors for nucleic acid analysis. *Nature Nanotechnology*, 6:615–624, 2011.

[48] J. M. Rothberg, W. Hinz, T. M. Rearick, J. Schultz, W. Mileski, M. Davey, J. H. Leamon, K. Johnson, M. J. Milgrew, M. Edwards, J. Hoon, J. F. Simons, D. Marran, J. W. Myers, J. F. Davidson, A. Branting, J. R. Nobile, B. P. Puc, D. Light, T. A. Clark, M. Huber, J. T. Branciforte, I. B. Stoner, S. E. Cawley, M. Lyons, Y. T. Fu, N. Homer, M. Sedova, X. Miao, B. Reed, J. Sabina, E. Feierstein, M. Schorn, M. Alanjary, E. Dimalanta, D. Dressman, R. Kasinskas, T. Sokolsky, J. A. Fidanza, E. Namsaraev, K. J. McKernan, A. Williams, G. T. Roth, and J. Bustillo. An integrated semiconductor device enabling non-optical genome sequencing. *Nature*, 475: 348–352, 2011.

[49] J. T. Davie, M. H. P. Kole, J. J. Letzkus, E. A. Rancz, N. Spruston, G. J. Stuart, and M. Hausser. Dendritic patch-clamp recording. *Nature Protocols*, 1:1235–1247, 2006.

[50] S. Ingebrandt, C. K. Yeung, M. Krause, and A. Offenhausser. Cardiomyocyte-transistor-hybrids for sensor application. *Biosensors and Bioelectronics*, 16:565–570, 2001.

[51] P. Fromherz. Electrical interfacing of nerve cells and semiconductor chips. *ChemPhysChem*, 3:276–284, 2002.

[52] R. H. Reuss, D. G. Hopper, and J. G. Park. Macroelectronics. *MRS Bulletin*, 31: 447–450, 2006.

[53] P. Benkart, A. Heittmann, H. Huebner, U. Ramacher, A. Kaiser, A. Munding, M. Bschorr, H. J. Pfleiderer, and E. Kohn. 3d chip stack technology using through-chip interconnects. *IEEE Design and Test of Computers*, 22:512–518, 2005.

[54] J. H. Ahn, H. S. Kim, K. J. Lee, S. Jeon, S. J. Kang, Y. G. Sun, R. G. Nuzzo, and J. A. Rogers. Heterogeneous three-dimensional electronics by use of printed semiconductor nanomaterials. *Science*, 314:1754–1757, 2006.

[55] B. Z. Tian, X. L. Zheng, T. J. Kempa, Y. Fang, N. F. Yu, G. H. Yu, J. L. Huang, and C. M. Lieber. Coaxial silicon nanowires as solar cells and nanoelectronic power sources. *Nature*, 449:885–888, 2007.

[56] X. J. Duan, R. X. Gao, P. Xie, T. Cohen-Karni, Q. Qing, H. S. Choe, B. Z. Tian, X. C. Jiang, and C. M. Lieber. Intracellular recordings of action potentials by an extracellular nanoscale field-effect transistor. *Nature Nanotechnology*, 7:174–179, 2012.

[57] H. Yan, H. S. Choe, S. W. Nam, Y. J. Hu, S. Das, J. F. Klemic, J. C. Ellenbogen, and C. M. Lieber. Programmable nanowire circuits for nanoprocessors. *Nature*, 470: 240–244, 2011.

[58] Y. Qin, X. D. Wang, and Z. L. Wang. Microfibre-nanowire hybrid structure for energy scavenging. *Nature*, 451:809–813, 2008.

[59] C. K. Chan, H. L. Peng, G. Liu, K. McIlwrath, X. F. Zhang, R. A. Huggins, and Y. Cui. High-performance lithium battery anodes using silicon nanowires. *Nature Nanotechnology*, 3:31–35, 2008.

[60] Z. Y. Fan, J. C. Ho, Z. A. Jacobson, H. Razavi, and A. Javey. Large-scale, heterogeneous integration of nanowire arrays for image sensor circuitry. *Proceedings of the National Academy of Sciences of the United States of America*, 105:11066–11070, 2008.

[61] R. R. He and P. D. Yang. Giant piezoresistance effect in silicon nanowires. *Nature Nanotechnology*, 1:42–46, 2006.

[62] L. G. Griffith and M. A. Swartz. Capturing complex 3d tissue physiology in vitro. *Nature Reviews Molecular Cell Biology*, 7:211–224, 2006.

[63] R. Glicklis, J. C. Merchuk, and S. Cohen. Modeling mass transfer in hepatocyte spheroids via cell viability, spheroid size, and hepatocellular functions. *Biotechnology and Bioengineering*, 86:672–680, 2004.

[64] F. Patolsky, G. F. Zheng, and C. M. Lieber. Nanowire-based biosensors. *Analytical Chemistry*, 78:4260–4269, 2006.

[65] F. Patolsky, B. P. Timko, G. F. Zheng, and C. M. Lieber. Nanowire-based nanoelectronic devices in the life sciences. *MRS Bulletin*, 32:142–149, 2007.

[66] N. A. Kotov, J. O. Winter, I. P. Clements, E. Jan, B. P. Timko, S. Campidelli, S. Pathak, A. Mazzatenta, C. M. Lieber, M. Prato, R. V. Bellamkonda, G. A. Silva, N. W. S. Kam, F. Patolsky, and L. Ballerini. Nanomaterials for neural interfaces. *Advanced Materials*, 21:3970–4004, 2009.

[67] K. I. Chen, B. R. Li, and Y. T. Chen. Silicon nanowire field-effect transistor-based biosensors for biomedical diagnosis and cellular recording investigation. *Nano Today*, 6:131–154, 2011.

[68] J. Hahm and C. M. Lieber. Direct ultrasensitive electrical detection of dna and dna sequence variations using nanowire nanosensors. *Nano Letters*, 4:51–54, 2004.

[69] F. Patolsky, G. F. Zheng, O. Hayden, M. Lakadamyali, X. W. Zhuang, and C. M. Lieber. Electrical detection of single viruses. *Proceedings of the National Academy of Sciences of the United States of America*, 101:14017–14022, 2004.

[70] W. U. Wang, C. Chen, K. H. Lin, Y. Fang, and C. M. Lieber. Label-free detection of small-molecule-protein interactions by using nanowire nanosensors. *Proceedings of the National Academy of Sciences of the United States of America*, 102:3208–3212, 2005.

[71] F. Patolsky, B. P. Timko, G. H. Yu, Y. Fang, A. B. Greytak, G. F. Zheng, and C. M. Lieber. Detection, stimulation, and inhibition of neuronal signals with high-density nanowire transistor arrays. *Science*, 313:1100–1104, 2006.

[72] T. Cohen-Karni, B. P. Timko, L. E. Weiss, and C. M. Lieber. Flexible electrical recording from cells using nanowire transistor arrays. *Proceedings of the National Academy of Sciences of the United States of America*, 106:7309–7313, 2009.

[73] Q. Qing, S. K. Pal, B. Z. Tian, X. J. Duan, B. P. Timko, T. Cohen-Karni, V. N. Murthy, and C. M. Lieber. Nanowire transistor arrays for mapping neural circuits

in acute brain slices. *Proceedings of the National Academy of Sciences of the United States of America*, 107:1882–1887, 2010.

[74] T. Cohen-Karni, D. Casanova, J. F. Cahoon, Q. Qing, D. C. Bell, and C. M. Lieber. Synthetically encoded ultrashort-channel nanowire transistors for fast, pointlike cellular signal detection. *Nano Letters*, 12:2639–2644, 2012.

[75] Q. Qing, Z. Jiang, L. Xu, R. Gao, L. Mai, and C. M. Lieber. Free-standing kinked nanowire transistor probes for targeted intracellular recording in three dimensions. *Nature Nanotechnology*, 9:142–147, 2014.

[76] S. W. Hwang, H. Tao, D. H. Kim, H. Y. Cheng, J. K. Song, E. Rill, M. A. Brenckle, B. Panilaitis, S. M. Won, Y. S. Kim, Y. M. Song, K. J. Yu, A. Ameen, R. Li, Y. W. Su, M. M. Yang, D. L. Kaplan, M. R. Zakin, M. J. Slepian, Y. G. Huang, F. G. Omenetto, and J. A. Rogers. A physically transient form of silicon electronics. *Science*, 337: 1640–1644, 2012.

[77] Y. Cui, L. J. Lauhon, M. S. Gudiksen, J. F. Wang, and C. M. Lieber. Diameter-controlled synthesis of single-crystal silicon nanowires. *Applied Physics Letters*, 78: 2214–2216, 2001.

[78] P. V. Brady and J. V. Walther. Kinetics of quartz dissolution at low-temperatures. *Chemical Geology*, 82:253–264, 1990.

[79] S. Ahn, P. S. Spuhler, M. Chiari, M. Cabodi, and M. S. Unlu. Quantification of surface etching by common buffers and implications on the accuracy of label-free biological assays. *Biosensors and Bioelectronics*, 36:222–229, 2012.

[80] M. S. Lord, M. Foss, and F. Besenbacher. Influence of nanoscale surface topography on protein adsorption and cellular response. *Nano Today*, 5:66–78, 2010.

[81] L. L. Hench. Bioceramics. *Journal of the American Ceramic Society*, 81:1705–1728, 1998.

[82] B. D. Ratner, A. S. Hoffman, F. J. Schoen, and J. E. Lemons. *Biomaterials Science - An Introduction to Materials in Medicine*. Academic Press, 2nd edition, 2004.

[83] J. Robertson. High dielectric constant oxides. *European Physical Journal-Applied Physics*, 28:265–291, 2004.

[84] A. C. Dillon, A. W. Ott, J. D. Way, and S. M. George. Surface-chemistry of al2o3 deposition using al(ch3)(3) and h2o in a binary reaction sequence. *Surface Science*, 322: 230–242, 1995.

[85] M. D. Groner, F. H. Fabreguette, J. W. Elam, and S. M. George. Low-temperature al_2o_3 atomic layer deposition. *Chemistry of Materials*, 16:639–645, 2004.

[86] F. Patolsky, G. Zheng, and C. M. Lieber. Fabrication of silicon nanowire devices for ultrasensitive, label-free, real-time detection of biological and chemical species. *Nature Protocols*, 1:1711–1724, 2006.

[87] E. Rosellini, C. Cristallini, N. Barbani, G. Vozzi, and P. Giusti. Alginate/gelatin blends for the preparation of biodegradable scaffolds for myocardial tissue engineering. *Journal Of Applied Biomaterials and Biomechanics*, 5:218–218, 2007.

[88] S. Guha, E. Cartier, N. A. Bojarczuk, J. Bruley, L. Gignac, and J. Karasinski. High-quality aluminum oxide gate dielectrics by ultra-high-vacuum reactive atomic-beam deposition. *Journal of Applied Physics*, 90:512–514, 2001.

[89] H. Jawad, N. N. Ali, A. R. Lyon, Q. Z. Chen, S. E. Harding, and A. R. Boccaccini. Myocardial tissue engineering: a review. *Journal Of Tissue Engineering And Regenerative Medicine*, 1:327–342, 2007.

[90] H. C. Hulst and H. C. van de Hulst. *Light Scattering by Small Particles*. Courier Dover Publications, 1957.

[91] M. N. Giraud, C. Armbruster, T. Carrel, and H. T. Tevaearai. Current state of the art in myocardial tissue engineering. *Tissue Engineering*, 13:1825–1836, 2007.

[92] A. N. Morritt, S. K. Bortolotto, R. J. Dilley, X. L. Han, A. R. Kompa, D. McCombe, C. E. Wright, S. Itescu, J. A. Angus, and W. A. Morrison. Tissue engineering of a vascularised myocardial patch. *Tissue Engineering*, 13:1769–1769, 2007.

[93] W. Lu, J. Xiang, B. P. Timko, Y. Wu, and C. M. Lieber. One-dimensional hole gas in germanium/silicon nanowire heterostructures. *Proceedings of the National Academy of Sciences of the United States of America*, 102:10046–10051, 2005.

[94] J. R. Fuchs, B. A. Nasseri, J. P. Vacanti, and D. O. Fauza. Postnatal myocardial augmentation with skeletal myoblast-based fetal tissue engineering. *Surgery*, 140: 100–107, 2006.

[95] C. Thelander, L. E. Froberg, C. Rehnstedt, L. Samuelson, and L. E. Wemersson. Vertical enhancement-mode inas nanowire field-effect transistor with 50-nm wrap gate. *IEEE Electron Device Letters*, 29:206–208, 2008.

[96] T. Eschenhagen and W. H. Zimmermann. Engineering myocardial tissue. *Circulation Research*, 97:1220–1231, 2005.

[97] R. Langer and J. P. Vacanti. Tissue engineering. *Science*, 260:920–926, 1993.

[98] P. A. Tresco. Tissue engineering strategies for nervous system repair. *Progress in Brain Research*, 128:349–363, 2000.

[99] C. E. Schmidt and J. B. Leach. Neural tissue engineering: strategies for repair and regeneration. *Annual Review of Biomedical Engineering*, 5:293–347, 2003.

[100] T. Eschenhagen, C. Fink, U. Remmers, H. Scholz, J. Wattchow, J. Weil, W. Zimmerman, H. H. Dohmen, H. Schafer, N. Bishopric, T. Wakatsuki, and E. L. Elson. Three-dimensional reconstitution of embryonic cardiomyocytes in a collagen matrix: a new heart muscle model system. *Faseb Journal*, 11:683–694, 1997.

[101] M. Radisic, H. Park, H. Shing, T. Consi, F. J. Schoen, R. Langer, L. E. Freed, and G. Vunjak-Novakovic. Functional assembly of engineered myocardium by electrical stimulation of cardiac myocytes cultured on scaffolds. *Proceedings Of the National Academy Of Sciences Of the United States Of America*, 101:18129–18134, 2004.

[102] T. Shimizu, M. Yamato, Y. Isoi, T. Akutsu, T. Setomaru, K. Abe, A. Kikuchi, M. Umezu, and T. Okano. Fabrication of pulsatile cardiac tissue grafts using a

novel 3-dimensional cell sheet manipulation technique and temperature-responsive cell culture surfaces. *Circulation Research*, 90:40–48, 2002.

[103] G. C. Engelmayr, M. Y. Cheng, C. J. Bettinger, J. T. Borenstein, R. Langer, and L. E. Freed. Accordion-like honeycombs for tissue engineering of cardiac anisotropy. *Nature Materials*, 7:1003–1010, 2008.

[104] D. Huh, B. D. Matthews, A. Mammoto, M. Montoya-Zavala, H. Y. Hsin, and D. E. Ingber. Reconstituting organ-level lung functions on a chip. *Science*, 328:1662–1668, 2010.

[105] L. G. Griffith and G. Naughton. Tissue engineering–current challenges and expanding opportunities. *Science*, 295:1009–1014, 2002.

[106] A. Hansen, A. Eder, M. Bonstrup, M. Flato, M. Mewe, S. Schaaf, B. Aksehirlioglu, A. Schworer, J. Uebeler, and T. Eschenhagen. Development of a drug screening platform based on engineered heart tissue. *Circulation Research*, 107:35–70, 2010.

[107] A. Grosberg, P. W. Alford, M. L. McCain, and K. K. Parker. Ensembles of engineered cardiac tissues for physiological and pharmacological study: Heart on a chip. *Lab on a Chip*, 11:4165–4173, 2011.

[108] M. Baker. A living system on a chip. *Nature*, 471:661–665, 2011.

[109] D. W. Hutmacher. Biomaterials offer cancer research the third dimension. *Nature Materials*, 9:90–93, 2010.

[110] A. Natarajan, M. Stancescu, V. Dhir, C. Armstrong, F. Sommerhage, J. J. Hickman, and P. Molnar. Patterned cardiomyocytes on microelectrode arrays as a functional, high information content drug screening platform. *Biomaterials*, 32:4267–4274, 2011.

[111] A. Furuta, S. Miyoshi, Y. Itabashi, T. Shimizu, S. Kira, K. Hayakawa, N. Nishiyama, K. Tanimoto, Y. Hagiwara, T. Satoh, K. Fukuda, T. Okano, and S. Ogawa. Pulsatile cardiac tissue grafts using a novel three-dimensional cell sheet manipulation technique functionally integrates with the host heart, in vivo. *Circulation Research*, 98: 705–712, 2006.

[112] W. H. Zimmermann, I. Melnychenko, G. Wasmeier, M. Didie, H. Naito, U. Nixdorff, A. Hess, L. Budinsky, K. Brune, B. Michaelis, S. Dhein, A. Schwoerer, H. Ehmke, and T. Eschenhagen. Engineered heart tissue grafts improve systolic and diastolic function in infarcted rat hearts. *Nature Medicine*, 12:452–458, 2006.

[113] T. Dvir, B. P. Timko, D. S. Kohane, and R. Langer. Nanotechnological strategies for engineering complex tissues. *Nature Nanotechnology*, 6:13–22, 2011.

[114] M. N. Hirt, A. Hansen, and T. Eschenhagen. Cardiac tissue engineering: state of the art. *Circulation Research*, 114:354–367, 2014.

[115] M. Papadaki, N. Bursac, R. Langer, J. Merok, G. Vunjak-Novakovic, and L. E. Freed. Tissue engineering of functional cardiac muscle: molecular, structural, and electrophysiological studies. *American Journal of Physiology-Heart and Circulatory Physiology*, 280: H168–H178, 2001.

[116] I. R. Efimov, V. P. Nikolski, and G. Salama. Optical imaging of the heart. *Circulation Research*, 95:21–33, 2004.

[117] I. R. Efimov, V. V. Fedorov, B. Y. Joung, and S. F. Lin. Mapping cardiac pacemaker circuits methodological puzzles of the sinoatrial node optical mapping. *Circulation Research*, 106:255–271, 2010.

[118] T. J. Herron, P. Lee, and J. Jalife. Optical imaging of voltage and calcium in cardiac cells and tissues. *Circulation Research*, 110:609–623, 2012.

[119] J. M. Kralj, A. D. Douglass, D. R. Hochbaum, D. Maclaurin, and A. E. Cohen. Optical recording of action potentials in mammalian neurons using a microbial rhodopsin. *Nature Methods*, 9:90–95, 2012.

[120] J. H. Hou, J. M. Kralj, A. D. Douglass, F. Engert, and A. E. Cohen. Simultaneous mapping of membrane voltage and calcium in zebrafish heart in vivo reveals chamber-specific developmental transitions in ionic currents. *Frontiers in Physiology*, 5:1–10, 2014.

[121] J. B. Pawley. *Handbook of Biological Confocal Microscopy*. Springer, 3rd edition, 2006.

[122] J. Huisken, J. Swoger, F. Del Bene, J. Wittbrodt, and E. H. K. Stelzer. Optical sectioning deep inside live embryos by selective plane illumination microscopy. *Science*, 305:1007–1009, 2004.

[123] J. Viventi, D. H. Kim, L. Vigeland, E. S. Frechette, J. A. Blanco, Y. S. Kim, A. E. Avrin, V. R. Tiruvadi, S. W. Hwang, A. C. Vanleer, D. F. Wulsin, K. Davis, C. E. Gelber, L. Palmer, J. Van der Spiegel, J. Wu, J. L. Xiao, Y. G. Huang, D. Contreras, J. A. Rogers, and B. Litt. Flexible, foldable, actively multiplexed, high-density electrode array for mapping brain activity in vivo. *Nature Neuroscience*, 14, 2011.

[124] I. L. Jones, P. Livi, M. K. Lewandowska, M. Fiscella, B. Roscic, and A. Hierlemann. The potential of microelectrode arrays and microelectronics for biomedical research and diagnostics. *Analytical and Bioanalytical Chemistry*, 399:2313–2329, 2011.

[125] M. Reppel, F. Pillekarnp, Z. J. Lu, M. Halbach, K. Brockmeier, B. K. Fleischmann, and J. Hescheler. Microelectrode arrays: A new tool to measure embryonic heart activity. *Journal Of Electrocardiology*, 37:104–109, 2004.

[126] J. Viventi, D. H. Kim, J. D. Moss, Y. S. Kim, J. A. Blanco, N. Annetta, A. Hicks, J. L. Xiao, Y. G. Huang, D. J. Callans, J. A. Rogers, and B. Litt. A conformal, bio-interfaced class of silicon electronics for mapping cardiac electrophysiology. *Science Translational Medicine*, 2:1–9, 2010.

[127] L. Z. Xu, S. R. Gutbrod, A. P. Bonifas, Y. W. Su, M. S. Sulkin, N. S. Lu, H. J. Chung, K. I. Jang, Z. J. Liu, M. Ying, C. Lu, R. C. Webb, J. S. Kim, J. I. Laughner, H. Y. Cheng, Y. H. Liu, A. Ameen, J. W. Jeong, G. T. Kim, Y. G. Huang, I. R. Efimov, and J. A. Rogers. 3d multifunctional integumentary membranes for spatiotemporal cardiac measurements and stimulation across the entire epicardium. *Nature Communications*, 5:1–10, 2014.

[128] J. Liu, C. Xie, X. C. Dai, L. H. Jin, W. Zhou, and C. M. Lieber. Multifunctional three-dimensional macroporous nanoelectronic networks for smart materials. *Proceedings of the National Academy of Sciences of the United States of America*, 110:6694–6699, 2013.

[129] F. Yang, R. Murugan, S. Wang, and S. Ramakrishna. Electrospinning of nano/micro scale poly(l-lactic acid) aligned fibers and their potential in neural tissue engineering. *Biomaterials*, 26:2603–2610, 2005.

[130] P. Gentile, V. Chiono, I. Carmagnola, and P. V. Hatton. An overview of poly(lactic-co-glycolic) acid (plga)-based biomaterials for bone tissue engineering. *International Journal of Molecular Sciences*, 15:3640–3659, 2014.

[131] E. S. Place, J. H. George, C. K. Williams, and M. M. Stevens. Synthetic polymer scaffolds for tissue engineering. *Chemical Society Reviews*, 38:1139–1151, 2009.

[132] D. Zhang, I. Y. Shadrin, J. Lam, H. Q. Xian, H. R. Snodgrass, and N. Bursac. Tissue-engineered cardiac patch for advanced functional maturation of human esc-derived cardiomyocytes. *Biomaterials*, 34:5813–5820, 2013.

[133] A. W. Feinberg, P. W. Alford, H. Jin, C. M. Ripplinger, A. A. Werdich, S. P. Sheehy, A. Grosberg, and K. K. Parker. Controlling the contractile strength of engineered cardiac muscle by hierarchal tissue architecture. *Biomaterials*, 33:5732–5741, 2012.

[134] M. Miragoli, G. Gaudesius, and S. Rohr. Electrotonic modulation of cardiac impulse conduction by myofibroblasts. *Circulation Research*, 98:801–810, 2006.

[135] M. Miragoli, N. Salvarani, and S. Rohr. Myofibroblasts induce ectopic activity in cardiac tissue. *Circulation Research*, 101:755–758, 2007.

[136] D. P. Zipes. Atrial fibrillation: From cell to bedside. *Journal of Cardiovascular Electrophysiology*, 8:927–938, 1997.

[137] G. Marton, I. Bakos, Z. Fekete, I. Ulbert, and A. Pongracz. Durability of high surface area platinum deposits on microelectrode arrays for acute neural recordings. *Journal of Materials Science-Materials in Medicine*, 25:931–940, 2014.

[138] S. J. Wilks, S. M. Richardson-Burns, J. L. Hendricks, D. C. Martin, and K. J. Otto. Poly(3,4-ethylenedioxythiophene) as a micro-neural interface material for electrostimulation. *Frontiers in Neuroengineering*, 2:1–8, 2009.

[139] W. Lu and C. M. Lieber. Nanoelectronics from the bottom up. *Nature Materials*, 6: 841–850, 2007.